PRACA DOKTORSKA

IChF
Institute of Physical Chemistry PAS

UNIVERSITÄT
LEIPZIG

Titania-based heterogeneous photocatalysis for the selective oxidation of biomass-derived platform chemicals

Thesis submitted for the degree

of

Doctor of Philosophy

in the field of

Chemical Sciences

prepared within the

International Ph.D. Studies

of the

Institute of Physical Chemistry (IPC), Polish Academy of Sciences (PAS),

Warsaw, Poland

by

Ayesha Khan

Supervised by

dr hab. inż. Juan Carlos Colmenares (Assoc. Prof. IPC, PAS)

and

Univ.-Prof. Dr. rer. nat. habil. Roger Gläser (Leipzig University)

Institute of Physical Chemistry, Polish Academy of Sciences

ul. Kasprzaka 44/52, 01-224

Warsaw, September 2021

Dedicated to

my Dearest Almighty Allah

and

my Dearest Prophet Muhammad (Peace be upon him)

Acknowledgments

If you feel like you have reached the end of the road and want to give up, think of the hundreds of time you have failed and yet Allah's mercy remains. First and foremost, I would like to pay my utmost gratitude to Almighty Allah for the countless blessings, mercy, help and guidance that has been a real source to accomplish this task.

I would like to thank Prof. Juan Carlos Colmenares for giving me an opportunity to conduct my Ph.D. studies in his research group and, for providing the freedom and infrastructure to explore many aspects of photocatalysis. Moreover, I am also grateful for his invaluable guidance, feedback and support during the course of my Ph.D. studies.

I would like to thank Prof. Roger Gläser for providing me a welcoming and motivating working environment during my secondment at the Institute of Chemical Technology, Leipzig University. Moreover, I am thankful to his invaluable in put, guidance and support all these years.

I would like to express my sincere gratitude to Dr. Michael Goepel for always being ready to help. It has been a great pleasure for me to work with him. The discussions we had about experiments and the comments and suggestions he gave me while writing the papers and thesis, helped enormously to finish this work as planned. Moreover, I appreciate the help he provided regarding the personal matters during my stay in Germany.

I would like to thank Dr. Dariusz Łomot for the assistance in characterization (N_2 sorption measurement and TPO-TPR measurements) and solving other technical problems in the Lab related to the instruments.

I would like to thank all the current and former members of "Catalysis for sustainable energy production and environmental protection group" (Tomasz Danko, Paweł Lisowski, Agnieszka Dżugan, Abdul Qayyum, Dr. Dimitrios Giannakoudakis, Karolina Kawka, Dr. Rafael L. Oliveira and Dr. Vaishakh Nair) for the help and support during my Ph.D. studies. Special thanks to my friends Swaraj Rashmi Pradhan and Jovana Prekodravac, their moral support means a lot to me.

I would also like to express my gratitude to the members of "Heterogeneous catalysis group" of the Institute of Chemical Technology, Leipzig University for their help and corporation during my stay there.

I would like to thank other colleagues of the Institute of Physical Chemistry, Dr. Wojciech Lisowski for XPS measurement, Dr. Dmytro Lisovytskiy for XRD and XRF measurements, Prof. Rafał Szmigielski for GC-MS analysis, Dr. Ariadna Nowicka for Raman spectroscopy analysis, Ms. Agnieszka Wiśniewska for TGA measurements and Dr. Magdalena Warczak for electrochemical measurements

I would like to extend my thanks to the administrative staff of the Institute of Physical Chemistry especially, Patrycja Niton, Monika Kuczynska and Joanna Wiszniowska for their help and cooperation.

I would like to thank all the NaMes fellows for their help and cooperation during the course of the Ph.D. studies

I also like to thank Dr. Marta Mazurkiewicz-Pawlicka from the Faculty of Chemical and Process Engineering, Warsaw University of Technology for her help in elemental analysis and TGA measurement.

I would like to thank Dr. Kamil Sobczak from the Faculty of Chemistry, Biological and Chemical Research Centre, University of Warsaw for TEM measurements.

I would also like to thank all my teachers who taught me at school, college and university, not only for educating me but also training me to face the challenges of life. I would like to thank Prof. Audil Rashid, for all the guidance and support during my scientific career. My sincere thanks to Prof. Ahmad Rafique Akhtar, his contribution in my life cannot be described in words. He changed my life, I cannot imagine how things would be if I have not known him. He taught me the life's most important lesson in the simplest way. I will never forget the support and courtesy he extended to me in the most difficult time of my life.

I always cherish the support and warm friendship of my friends (Rafia Younas, Shazia Anjum, Umsa Jameel, Misbah Khan, Ayesha Rubab, Shumail Ehsan, Salma Amir, Swaraj Rashmi Pradhan, Nabila Yasmeen, Jovana Prekodravac, Faria Khan, Rashmi Runjhun Alcina Johnson, Neha Rangam) here in Poland and back home in Pakistan. I am thankful for their help and support, and for all the fun we had together

I am extremely thankful to my parents for all the prayers, love, support and care. Without their support, I might not be the person I am today. I am sincerely thankful for everything they have done for me.

I am sincerely thankful to my dearest sisters (Mehwish Khan, Summaiya Khan and Ayiman Khan) for the prayers, care and unwavering support. Thank you for always being there for me to lift me up in hard times.

Last but not the least, I would like to thank my wonderful cousins (Kanza Khan, Usama Khan, Abdul Rahman Khan and Arsala Khan) for their encouragement and support, their presence means a lot in my life.

Gratitude to every single person who supported me, from the beginning of this journey up until this very moment in life.

Funding

- *This research is part of a project that has received funding from the European Union's Horizon 2020 research and innovation programme under the Marie Skłodowska-Curie grant agreement No. 711859.*
- *Scientific work funded from the financial resources for science in the years 2017-2022 awarded by the Polish Ministry of Science and Higher Education for the implementation of an international co-financed project.*
- *The National Science Centre, Poland, within OPUS-20 project No. 2020/39/B/ST5/00076*

NATIONAL SCIENCE CENTRE

Declaration of originality

I hereby declare that the research included within this thesis was carried out by myself or with support by others included in acknowledgments.

I state that I have exercised care to ensure that the work is original and contains no previously published material or written by another person, except where citations have been made in the text. To the best of my knowledge, the content provided here does not violate any copyrights.

I accept that the Polish Academy of Sciences has the right to use plagiarism detection software to ensure the thesis's legitimacy.

I certify that no part of my thesis has been or will be submitted for obtaining a degree or diploma by the Institute of Physical Chemistry, Polish Academy of Science, or any other educational institution.

This thesis's copyright rests with the author, and no information derived from it may be published without the author's consent.

Warsaw, September 2021

…….……
(signature)

List of publications

1. Ayesha Khan, Michael Goepel, Wojciech Lisowski, Dariusz Łomot, Dmytro Lisovytskiy, Marta Mazurkiewicz-Pawlicka, Roger Gläser, Juan Carlos Colmenares. 2021. Titania/Chitosan-Lignin nanocomposite as an efficient photocatalyst for the selective oxidation of benzyl alcohol under UV and visible light. Submitted to RSC Advances
2. Dimitrios A. Giannakoudakis, Abdul Qayyum, Vaishakh Nair, Ayesha Khan, Swaraj R. Pradhan, Jovana Prekodravac, Kyriazis Rekos, Alec P. LaGrow, Oleksandr Bondarchuk, Dariusz Łomot, Konstantinos S. Triantafyllidis, Juan Carlos Colmenares. 2021. Ultrasound-assisted decoration of CuO_x nanoclusters on TiO_2 nanoparticles for additives free photocatalytic hydrogen production and biomass valorization by selective oxidation. Mol. Catal. In Press
3. Ayesha Khan Michael Goepel, Adam Kubas, Dariusz Łomot, Wojciech Lisowski, Dmytro Lisovytskiy, Ariadna Nowicka, Juan Carlos Colmenares, Roger Gläser. 2021. Selective oxidation of 5-hydroxymethylfurfural to 2,5-diformylfuran by visible light-driven photocatalysis over in situ substrate-sensitized titania. ChemSusChem. 14, 1351-1362.
4. Ayesha Khan, Michael Goepel, Juan Carlos Colmenares, and Roger Gläser. 2020. Chitosan-based N-doped carbon materials for electrocatalytic and photocatalytic applications. *ACS Sustainable Chem. Eng.* 8, 4708-4727.
5. Dimitrios A. Giannakoudakis, Vaishakh Nair, Ayesha Khan, Eleni A. Deliyanni, Juan Carlos Colmenares, Konstantinos S. Triantafyllidis. 2019. Additive-free photo-assisted selective partial oxidation at ambient conditions of 5-hydroxymethylfurfural by manganese (IV) oxide nanorods. Appl. Catal. B: Environ. 256, 117803.
6. Ayesha Khan, Vaishakh Nair, Juan Carlos Colmenares and Roger Gläser. 2018. Lignin-Based Composite Materials for Photocatalysis and Photovoltaics. Top Curr Chem (Z) 376, 20.

List of Abbreviations

UV	Ultraviolet
LMCT	Ligand-to-metal charge transfer
HMF	5-hydroxymethylfurfural
DFF	2,5-diformylfuran
CL	Chitosan-lignin composite
T/CL	Titania/chitosan-lignin nanocomposite
BnOH	Benzyl alcohol
Bnald	Benzaldehyde
75T/CL	75wt%titania/chitosan-lignin nanocomposite
XPS	X-ray photoelectron spectroscopy
XRD	X-ray diffraction
FTIR	Fourier-transform infrared spectroscopy
CB	Conduction band
VB	Valence band
SHE	Standard hydrogen electrode
e^-	Electron
h^+	Hole
ROS	Reactive oxygen species
DSSCs	Dye-sensitized solar cells
PCE	Photoconversion efficiency
ESR	Electron spin resonance
AA	Ascorbic acid
EDTA	Ethylenediaminetetraacetic acid
AC	Activated carbon
MWNT	Multi-walled carbon nanotubes
SWP	Soft wood pellets
FDCA	2,5-furandicarboxylic acid
DMF	2,5-dimethyl furan
HMFCA	5-hydroxymethyl-2-furancarboxylic acid
FFCA	5-formyl-2-furancarboxylic acid
PBT	Polybutyleneterephthalate

PET	Polyethylene terephthalate
CoPz	Cobalt thioporphyrazine
MOFs	Metal-organic frameworks
DMF	N,N-dimethylformamide
SPD	Sonophotodeposition
WI	Wet impregnation
EPR	Electron paramagnetic resonance
SPR	Surface plasmon resonance
DRS	Diffuse reflectance spectroscopy
TTIP	Titanium(IV) isopropoxide
SGH-TiO_2	Sol-gel and hydrothermally prepared titania
HMF-Ads-SGH-TiO_2	5-hydroxymethylfurfural-adsorbed titania nanoparticles
HMF-Ads-P25	5-hydroxymethylfurfural-adsorbed commercial titania (P25)
BET	Brunauer-Emmet-Teller
BJH	Barrett, Joyner, Halenda
XRF	X-ray fluorescence
TEM	Transmission electron microscopy
TGA	Thermogravimetric analysis
SSA	Specific surface area
TPO	Temperature programmed oxidation
QMS	Quadrupole-mass-spectrometer
HPLC	High-performance liquid chromatography
AQY	Apparent quantum yield
LED	Light-emitting diode
ITO	Indium tin oxide
BQ	1,4-benzoquinone
SEM	Scanning electron microscopy
EIS	Electrochemical impedance spectroscopy
GC-MS	Gas chromatography-mass spectrometry
DMSO	Dimethylsulfoxide

Streszczenie

Dwutlenek tytanu , jako heterogeniczny fotokatalizator, ma wysoki potencjał w transformacji biomasy w produkty o dużej wartości dodanej, jednak często jest nieselektywny w reakcji utleniania związków organicznych ze względu na wytwarzanie wysoce aktywnych indywiduów utleniających, które nadmiernie utleniają substraty pod wpływem wysokoenergetycznego promieniowania UV. Wręcz przeciwnie, fotokataliza wykorzystująca światło widzialne oparta na dwutlenku tytanu do selektywnego utleniania związków modelowych składników biomasy jest uważana za podejście ekonomiczne i przyjazne dla środowiska. Teza ta skupia się przede wszystkim na aktywacji światłem widzialnym dwutlenku tytanu w celu jego zastosowania w fotokatalitycznym selektywnym utlenianiu tychże związków organicznych składników biomasy w produkty o dużej wartości dodanej. Zastosowano dwa podejścia do aktywacji światłem widzialnym dwutlenku tytanu zdolnego do selektywnego utleniania organicznych składników biomasy, tj. i) Uczulanie z przeniesieniem ładunku z liganda na metal (LMCT, skrót z ang. Ligand-to-Metal Charge Transfer), ii) Przygotowanie nanokompozytów z dwutlenku tytanu i materiałów węglowych. W celu uwrażliwienia LMCT, nanocząstki dwutlenku tytanu zsyntetyzowano metodą zol-żel połączoną z hydrotermalną, a następnie uczulenie dwutlenku tytanu osiągnięto poprzez utworzenie kompleksu LMCT (absorbującego światło widzialne) przez adsorpcję cząsteczki składnika biomasy (5-hydroksymetylofurfural, HMF) na powierzchni dwutlenku tytanu. Otrzymany kompleks LMCT umożliwił utlenianie HMF (59% konwersji) do przemysłowo ważnego związku 2,5- diformylofuranu (DFF) z wysoką selektywnością (87%) w świetle widzialnym (λ = 515 nm). Próbując poprawić aktywność dwutlenku tytanu w świetle widzialnym poprzez tworzenie nanokompozytów, najpierw zsyntetyzowano zestaw kompozytów chitozan-lignina (CL) metodą hydrotermalną, zmieniając

proporcje chitozanu i ligniny. Następnie, tak przygotowane kompozyty CL zintegrowano z dwutlenkiem tytanu (T) w celu przygotowania nanokompozytu (T/CL) metodą zol-żel połączoną z hydrotermalną. Jako reakcja testowa stosowana do oceny aktywności fotokatalitycznej nanokompozytu T/CL w świetle widzialnym ($\lambda = 515$ nm) wybrano selektywne utlenianie alkoholu benzylowego (BnOH) do benzaldehydu (Bnald). Reprezentatywny nanokompozyt 75T/CL(25:75) wykazywał doskonałą selektywność wobec Bnald (100%) przy umiarkowanej konwersji BnOH (19%) w świetle widzialnym. Na podstawie pomiarów XPS, sugeruje się, że aktywność nanokompozytów T/CL w świetle widzialnym można przypisać domieszkowaniu azotu (pochodzącego z chitozanu) do struktury dwutlenku tytanu. Przestawione wyniki sugerują zatem, że heterogeniczna fotokataliza sterowana światłem widzialnym, wykorzystująca powszechnie dostępny dwutlenek tytanu, ma wielki potencjał do waloryzacji organicznych składników pochodzących z biomasy poprzez selektywne utlenianie.

Abstract

Titania, as a heterogeneous photocatalyst has a significant potential for the conversion of biomass to value-added products. However, it is often unselective in organic oxidation reaction due to the generation of highly active oxidizing species, which over oxidizes the substrate under high energy UV radiation. On the contrary, titania-based visible light-driven photocatalysis for the selective oxidation of biomass-derived platform chemical is considered to be economical and environmentally benign approach. This thesis primarily focused on the visible light activation of titania for its application in the photocatalytic selective oxidation of biomass-derived platform chemicals into value-added products. Two approaches were employed for the visible light activation of titania for the selective oxidation of biomass-derived platform compounds i.e. i) Ligand-to-metal charge transfer (LMCT)-sensitization ii) Preparation of nanocomposites of titania and carbon materials. For LMCT-sensitization, titania nanoparticles were synthesized via sol-gel and hydrothermal method, subsequently sensitization of titania was achieved through the formation of visible light absorbing LMCT-complex on the titania surface by the adsorption of platform molecule, 5-hydroxymethylfurfural (HMF). The resulting LMCT-complex enabled the oxidation of HMF (59% conversion) to an industrially relevant compound 2,5- diformylfuran (DFF), with high selectivity (87%) under visible light (λ = 515 nm). In an attempt to improve the visible light activity of titania through nanocomposite formation, first, a set of chitosan-lignin (CL) composites have been synthesized via a hydrothermal method by varying the proportion of chitosan and lignin. Afterward, the as-prepared CL composites have been coupled with titania (T) to prepare a nanocomposite (T/CL) through sol-gel and hydrothermal approach. The test reaction used to assess the photocatalytic activity of T/CL nanocomposite under visible light (λ = 515 nm) is the

selective oxidation of benzyl alcohol (BnOH) to benzaldehyde (Bnald). A representative nanocomposite, 75T/CL(25:75) exhibited excellent selectivity for Bnald (100%) at moderate BnOH conversion (19%) under visible light. On the basis of XPS measurements, it is suggested that the T/CL nanocomposites activity under visible light may ascribed to the doping of nitrogen into titania framework from chitosan. The current findings, therefore suggest that visible-light driven heterogeneous photocatalysis employing abundantly available titania holds significant potential for the valorization of biomass-derived platform compounds via selective oxidation.

Contents

1. INTRODUCTION

1.1 Titania as photocatalyst

The photocatalytic activity of titania has inspired a wide range of research efforts since the discovery of photoelectrochemical water splitting on titania under ultraviolet light (UV) by Fujishima and Honda in 1972.[1] Few years later, the photocatalytic application of titania was extended to environmental frontiers. Frank and Bard[2] reported the photocatalytic oxidation of cyanide ion (an industrial pollutant) in aqueous solution using titania under solar irradiation.[2] Subsequent reports on titania catalyzed reduction of carbon dioxide to organic compounds (methanol, formaldehyde, formic acid and methane),[3] and photo-Kolbe decarboxylation for the production of butane[4] opened a new chapter of photocatalytic organic synthesis. Over the past few decades, titania has continued to be the most extensively studied photocatalyst for numerous applications such as, degradation of pollutants,[5,6] hydrogen generation via water splitting reaction,[1,7] dye-sensitized solar cells,[8] CO_2 reduction[9] and organic transformation reaction.[10,11,12,13] It has various advantages for its application in photocatalytic reactions for example, low cost, abundant availability, chemical and thermal stability, resistance to photocorrosion etc.[14,15] Titania generally exist in three different polymorphs including anatase (tetragonal), brookite (orthorhombic) and rutile (tetragonal). All the three crystalline phases of titania are made up of distorted TiO_6 octahedral unit (Figure 1), but connected in different ways.[16,17] Among the three crystalline phases, rutile is the most thermodynamically stable phase, whereas anatase and brookite are metastable phases that transform into rutile phase at elevated temperature (600 ^oC).[18] The photocatalytic activity of titania is influenced by its phase. Anatase is considered to be the most photocatalytically active polymorph of titania ascribed to its higher surface adsorption capacity to hydroxyl groups and a lower charge carrier recombination rate.[19]

Though, the band gap energy of rutile (~3.0 eV) is narrower than anatase (~3.2 eV), which broaden the light response range of rutile. However, the rutile phase tends to be stable at larger particle size (>35 nm), and exhibit lower specific surface area, which is not desirable from the photocatalytic point of view.[16] Whereas, the activity of the brookite phase has not been investigated systematically because of the difficulties in preparing its pure phase.[18,20] Possibly for these reasons, earliest studies on photocatalysis were carried out on anatase, and hence generally conclude that anatase phase of titania is the finest candidate in photocatalytic applications.[21,22]

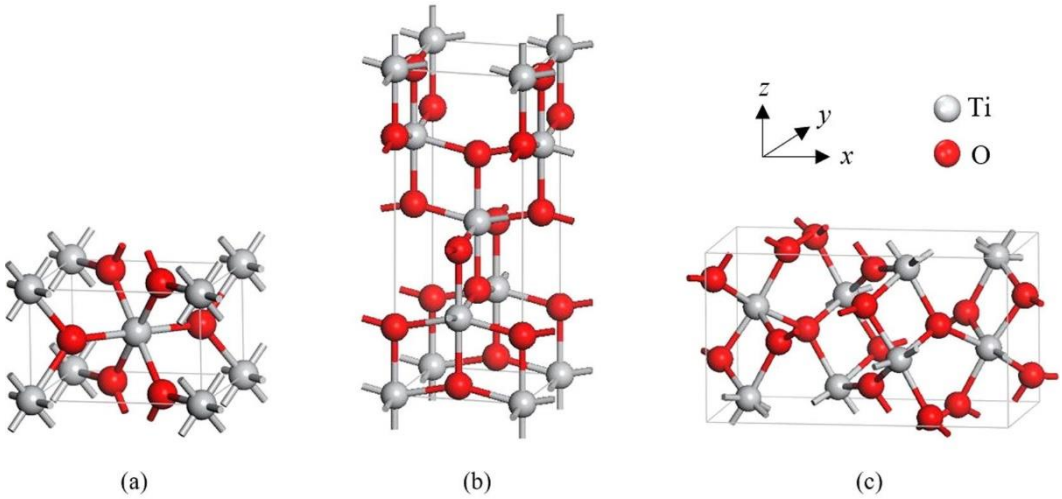

Figure 1. The primitive unit cell of (a) rutile, (b) anatase and (c) brookite phase of titania. (Reprinted an open-access article content [23])

However, several studies reported the excellent photocatalytic activity of brookite[9,24] and rutile[25] phases of titania. For example, Zhao et al.[26] reported that nanosheets of brookite efficiently catalyzed the oxidation of tetramethylbenzidine by H_2O_2 ascribed to its defects and flexible electronic states.[26] Besides that, single-crystalline brookite nanosheets showed enhanced activity toward the degradation of organic contaminants compared to commercial titania (P25), owing to the high-energy facets exposure and the efficient suppression of recombination rates of photogenerated charge carriers by these facets.[27] Similarly, rutile phase is also reported to have superior photocatalytic

activity than other phases of titania. For instance, the microspheres consist of rutile nanorods showed relatively higher photocatalytic activity than P25 for the degradation of papermaking wastewater due to specific crystal surface (001) exposure which may improve the separation of charge carriers, and enhanced the photocatalytic activity.[28] There are numerous factors such as, particle size, surface area, pore structure, ratio of polymorphs, density of defects, electronic structure, synthesis method, phase purity etc. that affect the photocatalytic activity of titania. [17,20,29,19,30] Therefore, the differences in photocatalytic activity among anatase, rutile and brookite phase is still under debate.

1.1.1 Mechanism and application of titania-based photocatalysis

Titania photocatalysis is a photon-driven process, initiated by the absorption of photon ($h\nu$) with an energy higher or equal to the bandgap of titania. The photon absorption in the bulk or at the surface of titania excites the electrons in the filled valence band (VB) to the vacant conduction band (CB), leaving behind the holes in the VB. During the transference process most (~90%)[31] of the electrons and holes undergo radiative or non-radiative recombination.[32] The electrons moved to the CB are good reducing agents, whereas the holes in the VB are strong oxidizing agents. As shown in Figure 2, the CB electrons can react with the O_2 in the surrounding medium and produce superoxide radical anions,[33] $O_2^{\bullet-}$ (redox potential +0.89 V vs standard hydrogen electrode, SHE).[20,34] Additionally, the $O_2^{\bullet-}$ generated may react with the VB holes and form singlet oxygen ($^1O_2$).[35] Nevertheless, the electrons may also reduce other ions or species in the surrounding medium if this is thermodynamically favored. While, the VB holes may react with the adsorbed water molecule (Figure 2) and form hydroxyl radicals, $^{\bullet}OH$ (redox potential +2.81 V vs SHE), hydrogen peroxide (H_2O_2), and hydroperoxyl radical ($HOO^{\bullet}$).[20,34] The $^{\bullet}OH$ can then participate in different oxidation reactions, on or near the surface of the titania (Figure 2). The H_2O_2 is further reported to be produced

by the hydroperoxyl radical coupling.[36] While, H_2O_2 may further react with $^{\bullet}OH$ and form $HOO^{\bullet}$.[20] During the photocatalytic process, free electrons, holes, and the reactive oxygen species (ROS) such as $^{\bullet}OH$, HOO• and $O_2^{\bullet-}$ react with the surface adsorbed species and inorganic and organic compounds in the surrounding medium.[20,37]

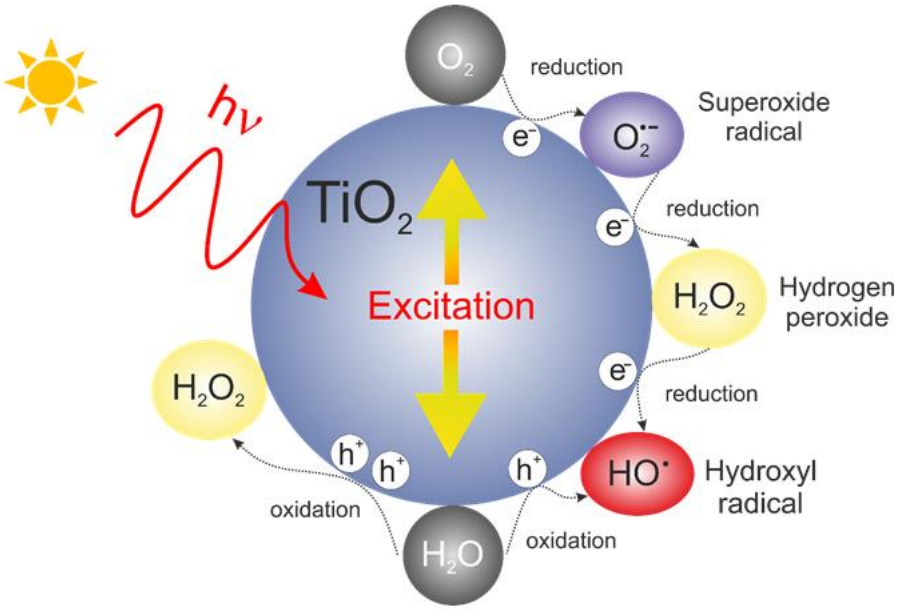

Figure 2. The generation of reactive oxygen species in titania-based photocatalysis. (Adapted with the permission of ref.[33])

The light absorption property and oxidation-reduction capability of titania depends on its band gap value and band edges position of the CB and VB, respectively. Moreover, charge (electrons and holes) separation also play an important role in determining the efficiency of a photocatalytic reaction.[31] Besides that, many elementary mechanistic processes have been involved in the photocatalytic redox processes over titania (Table 1). The efficient transformation of the absorbed photon to a chemically stored redox equivalent also depends on the rate of competing mechanistic processes (Table 1).

Table 1: Primary processes in heterogeneous titania photocatalysis and their characteristic times. >Ti^{IV}OH depicts the primary hydrated titania surface, e^-_{CB} is the conduction band electron, h^+_{VB} is the valence band hole, >$Ti^{IV}OH^{\bullet+}$is the surface bound hydroxyl radical or surface trapped hole, >$TiOH^{III}$ is the surface trapped conduction band electron (adapted with the permission of ref.[38])

Electronic step	Primary process	Time
Charge-carrier generation	$TiO_2 + hv \rightarrow e^-_{CB} + h^+_{VB}$	fs
Charge carrier trapping	$h^+ + >Ti^{IV}OH \rightarrow >Ti^{IV}OH^{\bullet+}$	10 ns
Shallow trap	$e^- + >Ti^{IV}OH \leftrightharpoons >TiOH^{III}$	100 ps
Deep trap	$e^- + >Ti^{IV} \rightarrow Ti^{III}$	10 ns
Charge carrier recombination	$e^- + >Ti^{IV}OH^{\bullet+} \rightarrow >Ti^{IV}OH$	100 ns
	$h^+ + >Ti^{III}OH \rightarrow Ti^{IV}OH$	10 ns
Interfacial charge transfer	$>Ti^{IV}OH^{\bullet+}$ + *organic molecule* → $>Ti^{IV}OH$ + *oxidized molecule*	100 ns
	$>Ti^{III}OH + O_2 \rightarrow >Ti^{IV}OH + O_2^{\bullet-}$	ms

The applications of titania as a photocatalyst can be broadly classified in to three categories, environmental applications (air and water purification), energy related application (hydrogen generation, photovoltaics), and organic synthesis (oxidation, reduction, and other transformations). Titania has been most widely used for the photocatalytic degradation of various organic pollutants such as polychrlorinatedbiphenyls,[39] methylene blue,[40] methyl orange,[40] Rhodamine B,[40] eriochrome black T,[40] and phenol.[41] Besides that, photodegradation of different pharmaceutical products such as tamoxifen,[42] gemfibrozil,[42] ibuprofen,[43] and carbamazepine[43] has also been successfully achieved using titania. The mechanism of photocatalytic degradation of organic compounds is similar to the titania-based photocatalysis described above. The photoinduced hydroxyl radicals $^{\bullet}$OH produced at the VB of titania acts as a strong oxidizing agents, and drive the oxidation of organic pollutant to purify the wastewater. Furthermore, the photoinduced electrons, HOO$^{\bullet}$ and

$O_2^{\bullet-}$ can reduce toxic metal ions, such as lead ions (Pb^{2+})[44], cadmium ions (Cd^{2+})[45] and chromium ions (Cr^{6+})[46] in wastewater. In addition, titania has also shown wide potential for the decontamination of various pollutants (alkenes,[47] alcohols,[48] nitrogen-containing compounds[49] etc.) in gas-phase.[50]

Titania also holds a significant potential to ease the energy crisis through effective exploitation of solar energy based on photovoltaic devices[51] and photocatalytic hydrogen production.[52] One of the key application of titania in photovoltaic is dye-sensitized solar cells (DSSCs).[53] Regan and Gratzel[51] provided a breakthrough in this field by developing a solar cell through titania thin films (nm) with monolayer coating of a charge-transfer dye to sensitize the film for harvesting light. The overall photoconversion efficiency (PCE) achieved under simulated solar light was 7.1-7.9%.[51] Though, for titania thin films, the overall PCE is limited due to charge carrier recombination and loss of electrons during percolation through the titania nanoparticle network within the film.[54] However, the PCE of titania-based DSSCs was improved up to 12.3% using a liquid cobalt(II/III)-based electrolyte and a zinc porphyrin sensitizer.[55] Photocatalytic hydrogen generation over titania is considered a key reaction towards the shift to a sustainable energy. However, pristine titania could not easily split water into H_2 and O_2 in the simple aqueous suspension, ascribed to the fast recombination of electron-hole pair.[32] Immobilizing highly dispersed metal (Au, Pd, Ag and Pt) nanoparticles, as cocatalyst on titania can help to improve the charge separation and photocatalytic efficiency for hydrogen production.[56,57] Moreover, the use of sacrificial donors (glycerol, methanol, ethanol)[58] can also enhance the photocatalytic hydrogen generation efficiency by scavenging the holes.[59] Chen et al.[60] reported that gold decorated P25 (Au/P25) showed much higher photocatalytic efficiency for H_2

generation (27.9 mmol g^{-1} h^{-1} in 10 vol.% glycerol) compared to bare P25 (1.9 mmol g^{-1} h^{-1} in 10 vol.% glycerol).[60]

The photocatalytic application of titania is extended to organic synthesis, providing an effective synthetic alternative for various industrially relevant chemicals. It offers the possibility of synthesizing high value-added chemicals through various processes, for example, oxidations, reductions,[61] isomerizations,[62] condensations[63,64] and polymerizations.[65] However, most of the titania-assisted photocatalytic organic transformation studies were focused on oxidation or reduction reactions, since the photoinduced active species produced intrinsically possess redox ability.

Titania has a significant potential to drive photocatalytic reductive chemical transformation of organic compounds[66,61] in the presence of suitable hole scavengers, and preferably in the absence of oxygen. The photocatalytic reduction of nitro compounds over titania produce corresponding amines through the formation of hydroxyl amine intermediates (Figure 3).[67] Imamura et al.[68] reported that, the highly selective reduction of m-nitrobenzenesulfonic acid to m-aminobenzenesulfonic acid (with >99% yield) could be achieved in an acidic aqueous suspensions utilizing formic acid as hole scavenger. The high yield of m-aminobenzenesulfonic acid was ascribed to the efficient hole scavenging ability of formic acid and probable repulsion of the reduced ammonium group from positively charged surface of titania in acidic medium, which prevents the re-oxidation of m-aminobenzenesulfonic acid.[68]

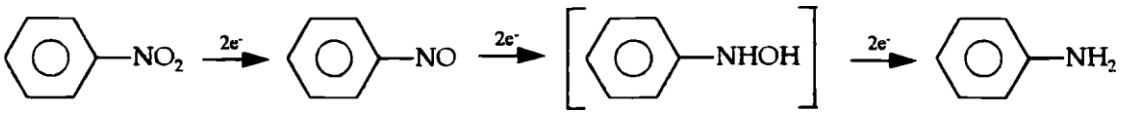

Figure 3. Photocatalytic reduction of nitrobenzene over titania. (Reprinted with the permission of ref.[67])

Furthermore, titania was successfully applied for the selective reduction of carbonyl compounds.[69] The efficient photocatalytic reduction of acetophenone derivatives and diaryl ketones to secondary alcohols (with ~100% yield) were achieved using ethanol as hole scavenger. [70]

Titania-assisted photocatalytic selective oxidation of alcohols, hydrocarbons, and amines is a major and well-studied category of organic transformation reactions. Photocatalytic selective oxidation of amines over titania produce corresponding imines, which are essential building blocks for the synthesis of pharmaceuticals, pesticides and fine chemicals.[71] It has been found that the crystalline phase of titania, electronic and surface structure characteristics play an important role in the adsorption and selective oxidation of amines.[71] Mixed-phase titania exhibited enhanced photocatalytic activity for the selective oxidation of benzylamine under visible light after 7 hours of illumination. The nanocomposite consists of 65% TiO_2(B) and 35% anatase showed 92% benzylamine conversion, whereas, single-phase TiO_2(B) and anatase showed much lower activity, with ~60% and ~50% benzylamine conversion, respectively. However, both mixed-phase and single-phase titania exhibited high (~93%) selectivity for imine. The enhanced photocatalytic performance of mixed-phase titania for the selective oxidation of benzylamine corresponds to the heterojunction between the two phases, which improved the charge separation efficiency.[72]

Selective activation of saturated C-H bonds in hydrocarbons (alkanes and aromatics) for the formation of value-added products (alcohols aldehyde and ketone) is of crucial importance for the chemical industry. However, the thermodynamically stable and inert nature of saturated C-H bonds make it significantly challenging.[73] It was observed that crystallinity of titania affect the photocatalytic selective oxidation of aromatic compounds to corresponding aldehyde. Cao et al.[74] reported that the anatase titania with

higher degree of crystallinity and exposed {001} facets exhibited enhanced photocatalytic performance for the selective oxidation of toluene (with 21% conversion) to benzaldehyde (with >90% selectivity) under UV light. Whereas, anatase with comparatively low crystallinity and commercial titania (P25) both showed ~9% toluene conversion with similar benzaldehyde selectivity. The improved performance of the anatase with comparatively higher degree of crystallinity ascribed to the improved charge separation efficiency.[74] Moreover, tuning of electronic structure of titania through ruthenium doping also reported to improve the selective oxidation of toluene to benzaldehyde under UV light.[75] It has been observed that introduction of $Ru^{3+/4+}$ states at 0.4 eV below the conduction band of titania improved the benzaldehyde selectivity by trapping electron, and suppressing the formation of excess $O_2^{-\bullet}$.[76]

Selective oxidation of alcohols to aldehydes and ketones gained burgeoning interest ascribed to their significance as raw materials for the production of vitamins, drugs, fragrances and flavors or food additives.[71] There are number of factors that influence the photocatalytic selective oxidation of alcohols over titania. In particular, crystallinity, polymorph type, surface acidity-basicity, crystal facet exposure, valence and conduction band edge position, charge recombination rate, hydroxyl group density, specific surface area, modification of titania (metal or non-metal doping / coupling with other semiconductors etc.),[18] which results in a different photocatalytic activity, and selectivity towards a target product. Yurdakal et al.[25] demonstrated that low-crystalline home-prepared rutile samples (HP333) showed improved photocatalytic performance for the selective oxidation of benzyl alcohol and 4-methoxybenzyl alcohol to the corresponding aldehydes compared to highly crystalline commercial rutile (SA). The poorly crystalline HP333 exhibited a selectivity of ca. 38% and 60% for benzaldehyde and 4-methoxybenzaldehyde, respectively at 50% conversion of the substrates.[25] The amorphous phase of titania improved the selectivity of the target product by offering

additional active sites for the partial oxidation and impeding the electron transfer between the particles due to the presence of the strongly basic terminal hydroxyl groups in amorphous phase.[77] Moreover, Wang et al.[78] reported that pretreating titania (P25) with Brønsted acids significantly enhanced the rate of oxidation of various aromatic alcohols under UV light. The photocatalytic conversion of benzyl alcohol on titania was increased from 46% to 66% after treating titania with hydrofluoric acid, retaining similar benzaldehyde selectivity (~99%). The improvement in the benzyl alcohol conversion in case of Brønsted acid-pretreated titania was ascribed to the decomposition of surface Ti-peroxide species by the Brønsted acids proton. This phenomenon results in the regeneration of active Ti-sites for the photocatalytic selective oxidation of alcohols.[78] Additionally, the effect of surface basic sites on the selective oxidation of alcohols has also been investigated. Leow et al.[79] found that, Al_2O_3 in the presence of dyes favored the partial oxidation of benzyl alcohol. This is attributed to the surface complexation of the alcohol on the Brønsted basic sites of the Al_2O_3, which decreases its oxidation potential and results in an upshift of its HOMO for the abstraction of electron by the dye.[79] In the last few years, an attention has been paid to study the influence of different facets of titania on the photocatalytic selective oxidation of alcohols. The anatase with predominant (001) facet (T001) exhibited enhanced photocatalytic performance for the selective oxidation of aromatic alcohols than the anatase with greater number of (101) facet (T101) under UV light in aqueous medium. The T001 sample showed much higher conversion for halogen substituted benzyl alcohols (49-53%) as compared to T101 (28-32%) keeping similar selectivity (97-100%) to corresponding aldehydes. The improved performance of the sample T001 was attributed to a higher surface energy value of the {001} facet which helps the activation of the substrates. Besides that, a higher number of oxygen vacancies and better adsorption of O_2 on (001) could trap photoelectron and prevent charge recombination.[80]

The effect of hydroxyl group density of titania on the photocatalytic selective oxidation of alcohols has been rarely studied. Di Paola et al.[81] investigated the role of hydroxyl group density of titania on the selective oxidation of 4-methoxybenzyl alcohol. It has been found that home-prepared titania sample with higher hydroxyl group density (10.76 w/w%) i.e. HPCl showed remarkably enhanced selectivity (92%) towards 4-methoxybenzaldehyde compared to poorly hydroxylated (0.76 w/w%) sample i.e. P25 (28%) at 20% substrate conversion under UV light.[81] The enhanced selectivity of aldehyde with higher degree of hydroxyl group density is probably related to the improved desorption of the aldehyde from the hydrophilic titania surface, which impedes its further oxidation.[82]

Moreover, a higher surface hydroxylation may hinder the oxidation of the reactant by limiting the surface coverage and the hole transfer to the substrate.[81] Besides the characteristic feature of titania, the nature of reaction medium also strongly influence the photocatalytic oxidation of alcohols over titania. Molinari et al.[83] demonstrated the positive influence of acetonitrile on the adsorption of aliphatic alcohols and subsequent photocatalytic oxidation on titania. According to ESR-spin trapping measurements, the minor water content (~2%) in acetonitrile strongly inhibit the adsorption and subsequent oxidation of alcohols on titania. For the photocatalytic oxidation of geraniol to corresponding aldehyde (citral), the selectivity of the citral was decreased from 73% to 50% after the addition of water (~4%) to acetonitrile. This is ascribed to the increase in the polarity of the dispersing medium by the addition of water, which facilitates the removal of the polar alcohols from the surface of titania. Besides that, water compete with the alcohol for the adsorption, which hampers the interaction of alcohol with the photocatalytic centres.[83]

Different mechanisms have been proposed for the photocatalytic oxidation of alcohols over titania, based on the selectivity and activity. Zhang et al.[84] performed oxygen isotope studies to provide fundamental insight to the oxidation of alcohols over the titania. ^{18}O-enriched benzyl alcohol and cyclohexanol have been used as representative alcohols to study the associated mechanism on titania. In oxygen deficient environment (under Ar flow), the alcohol is oxidized to corresponding aldehyde via two-electron transfer process, and the oxygen atom of the alcohol is retained in the product (Figure 4a). Whereas, in the presence of oxygen, alcohol underwent deprotonation and adsorb on the surface of titania (Structure I, Figure 4b). Upon UV light excitation, electron-hole pair were generated. The adsorbed alcohol reacts with the holes and subsequently underwent deprotonation to generate a carbon radical, while the Ti^{IV} trapped the photogenerated electrons and form Ti^{III} (Structure II, Figure 4b).

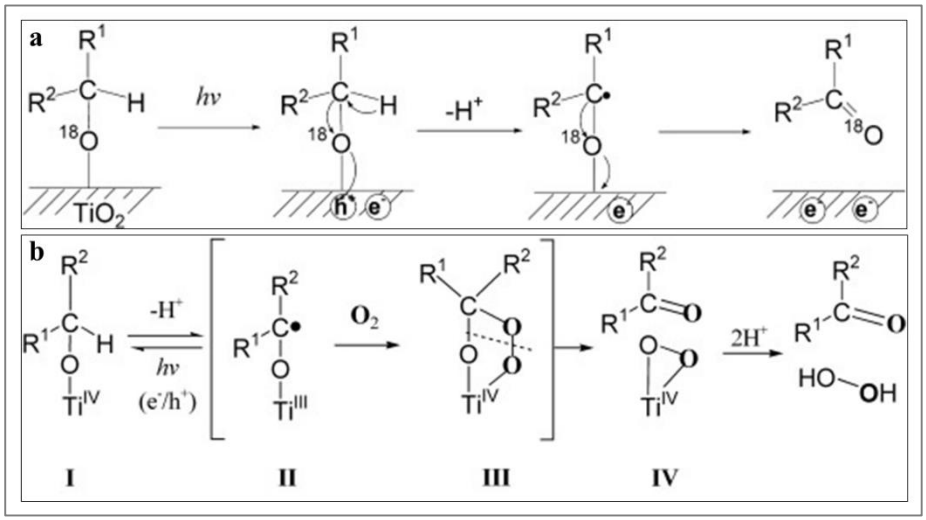

Figure 4. Proposed mechanism for alcohol oxidation on titania in benzotrifluoride solvent (a) in the absence of O_2 (b) in the presence of O_2. (Reprinted with the permission of ref.[84])

Both Ti^{III} and the carbon radical can easily combine with molecular oxygen to form a bridged oxygen structure (Structure III Figure 4b) via two possible ways. 1) Reduction

of oxygen by electron/Ti^{III} to form superoxide, which react with the carbon radical and form structure III (Figure 4b). 2) Reaction of carbon radical with molecular oxygen to form organic superoxyl radical, which then reacts with Ti^{III} and form structure III (Figure 4b). The breaking of C-O bond of alcohol and the O-O bond of molecular oxygen is possibly realized via such an oxygen bridged structure (Structure III, Figure 4b). The concerted bond cleavage of structure III produces aldehyde and titania-bound peroxide bridged structure (Structure IV, Figure 4b). The protons may react with the structure IV and form hydrogen peroxide, which is corroborated by iodometric titration studies.[84]

In this section an overview of titania catalyzed organic transformation reaction (especially for photooxidation of alcohols), has been provided. More details about the selective oxidation of biomass-derived platform chemicals (with special reference to 5-hydroxymethylfurfural and benzyl alcohol) is discussed in section 1.2.1 and 1.2.2.

1.1.2 Drawbacks of titania as photocatalyst

Despite several advantages of titania for photocatalytic application, it has some drawbacks too that limit its large-scale applications in photocatalysis. The main drawback of titania is the relatively wide band-gap (~3.2 eV for anatase and ~3.0 eV for rutile), which only permits the absorption of UV light (~5% of solar radiation).[85] This presents a crucial problem because UV light accounts for about <5% of the solar radiation,[85] which limit the possibility of using solar energy as a light source. Visible light absorption of titania is indispensable to harness sunlight due to high abundance of visible light (~45%) in the solar spectrum. The other major problem for titania material in the photocatalytic applications is its low quantum efficiency ascribed to the fast recombination of the electron-hole pairs.[15] Besides that, the separation or recovery of nanostructured titania from the liquid reaction medium is another issue related to its photocatalytic applications.[86]

1.1.3 Strategies to overcome the drawbacks of titania as photocatalyst

Various strategies have been adopted to overcome the narrow-light response range, low quantum efficiency and recovery issue of titania nanoparticles. Some of these approaches are discussed as follows.

1.1.3.1 Doping

Metal or non-metal doping of titania is a common strategy to modify the wide band-gap and improve the visible light absorption of titania. Non-metal doping is found to be more effective owing to the formation of fewer recombination centres in comparison with metal doping.[87] Nitrogen doping has been most extensively studied, among all non-metal doping in titania, and the possible means of visible-light absorption of N-doped titania has been elucidated. Dunnill et al.[88] showed that interstitial N-doping of titania results in visible light absorption of titania.[88] Whereas, Asahi et al.[89] proposed that substitutional N-doping of titania triggers the visible light absorption of titania. This is ascribed to the band-gap narrowing of titania due to mixing of O 2p states with the N 2p states of substituted N atoms in the newly formed VB.[89] Another proposition related to the origin of visible light absorption of N-doped titania is the formation of isolated N2p states above the VB of titania. These isolated energy levels facilitate the transfer of electron to the CB upon visible-light irradiation.[90] Besides that, Ihara et al[91] reported that the visible light absorption of N-doped titania is attributed to the creation of oxygen vacancies due to N-doping.[91] Although N-doping of titania is widely studied area, however, the underlying reason for N-doping-induced visible-light absorption, the exact nature of the chemical states formed via N-doping and the location of nitrogen in the titania lattice is still a matter of debate.

1.1.3.2 Coupling titania with other semiconductors

Fabrication of hetrostructure by combining titania with narrow band-gap semiconductor is another attractive approach to extend the photo-response of titania

into the visible light region and improve the separation of photogenerated electron-hole pairs via different carrier-transfer pathways.[92] Coupling titania with CdS (band-gap 2.4 eV) is most typical example of hetrostructured titania-based (TiO_2/CdS) photocatalyst. When TiO_2/CdS photocatalyst is irradiated under visible light, electrons are feasibly transferred from the CB of CdS to the CB of titania, whereas, the photogenerated hole remained in the VB of CdS.[93] The potential gradient built-in at the interface of titania and CdS assists in the better separation of electron-hole pairs and lessens the chance of recombination, which consequently improved the photocatalytic performance of the hetrostructured-titania.[94]

1.1.3.3 Sensitization by dyes and ligand to metal charge transfer (LMCT)-complex formation

Dye-sensitization: Dye-sensitization is one of the commonly used techniques for the visible light activation of titania. The organic dyes such as Erythrosin B, thionine, Eosin Y and Rhodamine B etc., adsorbed onto surface of titania are often used as sensitizers, ascribed to their visible light absorption ability.[95,96] The process of dye-sensitization is initiated by the photoexcitation of dye molecules, subsequently electrons are transferred from the excited dye molecules to the CB of titania (Figure 5). The oxidized dye molecules can be regenerated in the presence of suitable electron donors.[85] Dye sensitization also improve the photocatalytic performance of titania due to effective electro-hole pair separation,[97] as the transfer of electron from excited dye molecule to CB of titania occurred at a femtosecond scale in comparison to the electron-hole pair recombination, which occurred at nanoseconds to millisecond scale.[20,98] However, the low photostability of some organic dyes is a key concern associated with the dye-sensitization technique.[99,100]

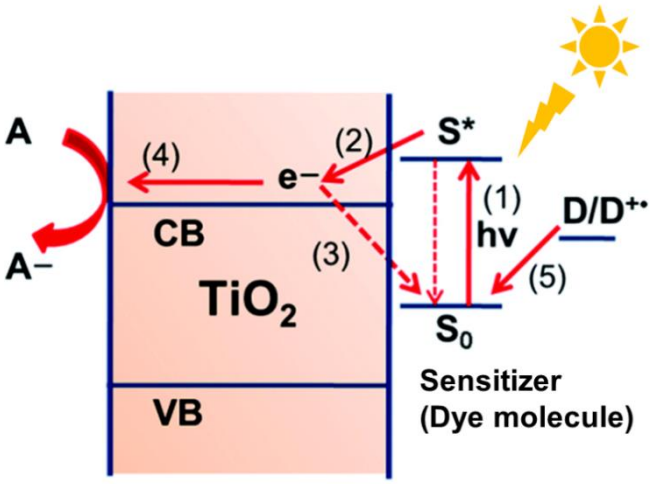

Figure 5. The schematic illustration of dye-sensitization of titania. 1) excitation of dye molecule by visible light absorption, (2) electron injection from the excited state of the dye to CB of titania, (3) recombination, (4) electron transfer to the acceptor, and (5) regeneration of the dye by an electron donor. S, D, and A represent the sensitizer (Dye molecule), electron donor, and electron acceptor, respectively. (S_0: ground state, S*: excited state of the sensitizer (Dye molecule). (Adapted with the permission of ref.[85])

Ligand to metal charge transfer (LMCT)-sensitization: Another approach employed for visible light activation of titania is the ligand to metal charge transfer (LMCT)-sensitization, which involves the sensitization of titania by surface adsorbates or substrates that do not absorb visible light by themselves.[85,101] During LMCT-sensitization electrons are transferred from the highest occupied molecular orbital (HOMO) of substrates/adsorbates to the CB of titania upon visible light irradiation (Figure 6).[85,102] In contrast to dye-sensitization, the electrons are directly excited from the ground state of adsorbate/substrate to the CB of titania, without involving the adsorbate/substrate excited state. The adsorbate/substrate could be regenerated by back electron transfer or by interacting with the electron donors in the reaction medium.[85]

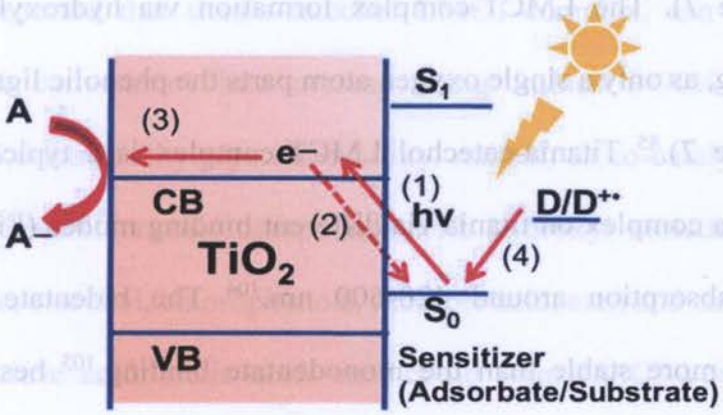

Figure 6. The schematic illustration of ligand to metal charge transfer (LMCT)-sensitization of titania. 1) visible light-induced LMCT transfer, (2) recombination, (3) electron transfer to the acceptor, and (4) regeneration of adsorbate/substrate by an electron donor. S, D, and A represent the sensitizer (adsorbate/substrate), electron donor, and electron acceptor, respectively. (S_0: ground state, S^1: excited state of the sensitizer (adsorbate/substrate). (Adapted with the permission of ref.[85])

The LMCT-complex formation on titania is generally accompanied by the visible light absorption, which is not observed with either the adsorbate or titania alone.[85] Generally, LMCT-surface-complexation induces visible light absorption extending up to far visible region (~650 nm). However, the intensity of visible light absorption of LMCT-complexed titania is influenced by the characteristic features of titania such as particle size, specific surface area, surface structure, hydroxyl groups etc.[85] Rajh et al.[103] reported that the overall optical absorption in dopamine-complexed titania was improved by reducing the particle size (from 15 nm to 4.5 nm). Moreover, the absorption was observed to be proportional to the fraction of Ti atoms at the surface.[103] Various studies have been performed on LMCT-complex formation on titania to elucidate the LMCT-induced visible light activation of titania. Phenolic compounds are potential candidates to form LMCT-complexes on titania through hydroxyl functional

groups (Figure 7). The LMCT-complex formation via hydroxyl groups facilitates strong coupling, as only a single oxygen atom parts the phenolic ligand from the titania surface (Figure 7).[85] Titania-catechol LMCT-complex is a typical example, where catechol form a complex on titania via different binding modes (Figure 7) and impart visible light absorption around 420-600 nm.[104] The bidentate binding mode is comparatively more stable than the monodentate binding,[105] besides that bidentate binding also enhanced the visible light absorption.[85] Moreover, presence of electron-donating group such as methyl or tert-butyl groups onto catechol further extend the visible light absorption of titania-catechol LMCT-complex towards longer wavelength.[103] The effect of substituent on visible light absorption is related to the dipole moment change in LMCT-complex formed between titania and substituted (electron-donating group) catechol, that may shift the electronic charge within the complex and extend the absorption to higher wavelength.[103]

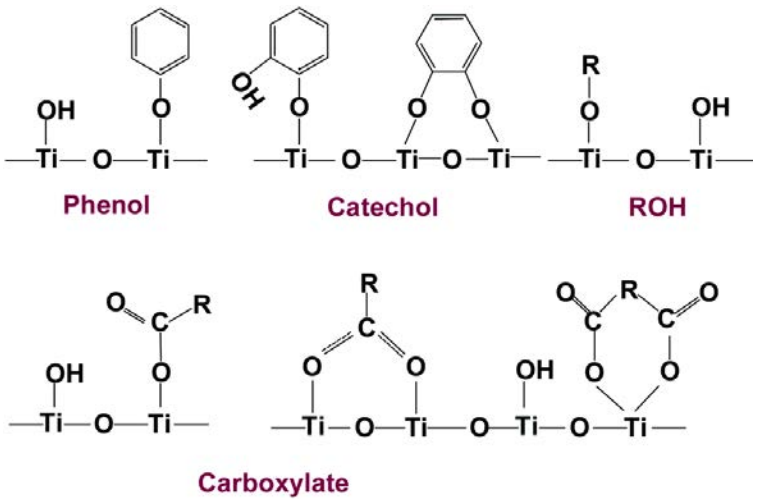

Figure 7. The possible binding modes of representative ligand to metal charge transfer (LMCT)-complexes on the titania surface. (Reprinted with the permission of ref.[85])

Shi et al.[106] reported that titania-catechol LMCT-complex, can efficiently oxidize amines (>90% conversion) into corresponding imines (>90% selectivity) using TEMPO (2,2,6,6-tetramethylpiperidine 1-oxyl radical) as co-catalyst under blue light irradiation.[106] Several organic compounds with hydroxyl moieties (benzyl alcohol, phenol, glucose, catechol, chlorophenols, ascorbic acid, etc.) and carboxylic acid group (formic acid, citric acid, lactic acid, etc.) could form LMCT-complexes on titania, accompanied by visible light absorption.[85] The LMCT-complex formed between ascorbic acid (AA) and titania can extend the visible light absorption of titania up to 800 nm, which is also accompanied by the change in color of titania from white to orange (Figure 8).[101] However, neither the ascorbic acid (AA) or titania showed absorption above 400 nm (Figure 8).[101] Surface-complexation of benzyl alcohols and its substituted derivatives (–OCH_3, –CH_3, –$C(CH_3)_3$, –Cl, –CF_3 and –NO_2) on titania selectively oxidize them into corresponding aldehydes (>99% selectivity) at high conversion of benzylic alcohols (>99%) upon blue light irradiation.[107]

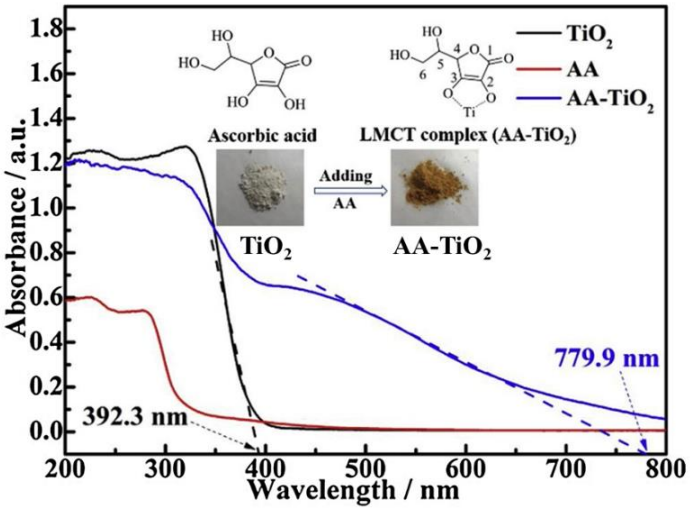

Figure 8. UV-Visible diffuse reflectance absorption spectra of ascorbic acid (AA), titania (TiO_2) and ascorbic acid-adsorbed titania-complex (AA-TiO_2). (Adapted with the permission of ref.[101])

Moreover, various organic compounds with carboxylic functional group are capable of forming LMCT-complex on titania. There are two possible binding configuration of titania-carboxylate complex i.e. monodentate binding and bidentate binding (Figure 7). Kim and Choi[102] demonstrated that ethylenediaminetetraacetic acid (EDTA) form a LMCT-complex on titania via carboxyl functional group, preferably through bidentate bridging coordination instead of monodentate binding. The surface-complexation of EDTA on titania induces absorption of visible light extending up to 550 nm, and exhibited significant photocatalytic activity for the reduction of Cr(VI) to Cr(III) and hydrogen generation in water.[102] Hydrogen peroxide (H_2O_2) also has a tendency to form a LMCT-complex on titania via condensation reaction.[85] The surface-complexation of H_2O_2 on titania changes its color from white to yellow and induce visible light absorption up to 550 nm. However, the titania-H_2O_2 complex is not stable and generate hydroxyl radicals ($^{\bullet}OH$) under visible light. This implies that titania-H_2O_2 complex can potentially be applied for the degradation of organic contaminants.[108]

Furfuryl alcohol, an important class of biomass-derived compounds with a variety of applications in chemical industry, can potentially form a LMCT-complex on titania, ascribed to the presence of hydroxyl group (OH). Wang et al.[109] reported that furfuryl alcohol can efficiently be chemosorbed over monolayer titanate nanosheet forming the surface coordination species via C-O groups. Upon visible light ($\lambda \geq 420$ nm) absorption the chemisorbed furfuryl alcohol over monolayer titanate nanosheets enables the oxidation of furfuryl alcohol (with 54% conversion) to furaldehyde, with high selectivity (99%).[109] This signifies that the derivatives of furfuryl alcohols, like 5-hydroxymethylfurfural (a platform compound) with hydroxyl moiety could potentially be employed for the visible light activation of titania and self-selective oxidation via LMCT-approach. This open-up a new avenue for the visible light active titania-based photocatalytic system for biomass valorization.

1.1.3.4 Titania/carbon composite

Recently, combining titania nanoparticles with carbon materials to form composites at nanoscale (nanocomposite) have attracted great deal of attention for the visible light activation of titania, to improve the photocatalytic performance of titania and, to overcome the problem of nanofiltration of titania nanoparticles. Carbon materials exhibit distinct features such as hydrophobic surfaces, multi-functionalities, high specific surface area, large pore volume, good chemical and thermal stability, that will enable their use in preparation of photocatalytic material. Comprehensive studies have been done on the advancement of titania/carbon composite formation and their application in heterogeneous photocatalysis.[110,111] In the context of green chemistry, renewable materials derived from biomass such as lignin, cellulose, chitosan, agriculture residues, activated carbon, fly ash and biochar are potential candidates for the preparation of composite.

Virkutyte et al.[112] reported that the nanocomposite prepared using titania and microcrystalline cellulose (TiO_2/MC) via sol-gel method under mild reaction conditions (atmospheric pressure and room temperature) exhibited efficient photocatalytic activity for the degradation (~90%) of methylene blue under visible light ($\lambda \geq 420$ nm). Whereas, commercial P25 showed negligible activity for the degradation of MB under visible light. The efficient photocatalytic activity of TiO_2/MC ascribed to the synergistic effect of the physical and/or chemical interactions between titania and MC.[112] It is suggested on the basis of XPS results that some of lattice titanium atoms may be substituted with carbon and form a Ti–O–C structure.[113] Moreover, combining microcrystalline cellulose with titania imparts the visible light absorption edge in TiO_2/MC up to 580 nm, and reduced the band gap of titania from 3.2 eV to 2.31 eV.[112] Activated carbon (AC), is a porous, amorphous solid carbon material derived mostly from carbonaceous or lignocellulosic materials.[114] It exhibits well-developed pore

structure, high specific surface area, and adsorption capacity, which are advantageous for its application in the preparation of photocatalytic materials.[86] Combining AC with titania could improve the photocatalytic efficiency of titania, as AC possess large number of adsorption sites which can assist in the adsorption of organic molecules before being transferred to the active center (titania).[115] Consequently, the ROS generated by the photocatalyst do not have to move very far from the active sites of the titania to catalyze a reaction. Moreover, AC can also act as a photosensitizer for titania by transferring electrons into the CB of titania upon light irradiation, and trigger the generation of ROS which can drive oxidation/reduction reaction.[116]

Titania-activated carbon composite (TiO_2(AC-700)) prepared via sol-gel method followed by calcination at 700 ^{O}C under air flow for 2 h, exhibited complete degradation of methylene blue (MB) in an aqueous solution after 2.5 hours of irradiation under visible light. Bare titania (prepared through sol-gel and calcination method) showed similar results for MB degradation at longer irradiation time (~3.5 hours). The apparent first-order rate constant of TiO_2(AC-700) for MB degradation (49.75×10^{-3} min^{-1}) under visible light irradiation showed that TiO_2(AC-700) catalyst was found to be approximately two times more active than bare titania (18.58×10^{-3} min^{-1}).[117] It has been proposed that degradation of MB over TiO_2(AC-700) and bare titania is driven by photosensitization, photolysis and photocatalysis. To further confirm the photocatalytic activity of TiO_2(AC-700), the degradation of photolysis resistant contaminant, 4-nitrophenol was carried out over TiO_2(AC-700) under visible light. Interestingly, TiO_2(AC-700) showed over 90% degradation of 4-nitrophenol after 6 hours of irradiation under visible light with an apparent first order rate constant of 2.03×10^{-3} min^{-1}.[117] The improved photocatalytic activity of TiO_2(AC-700) compared to bare titania for MB degradation is ascribed to number of factors. For example, bare titania predominantly consist of rutile phase, whereas, TiO_2(AC-700) consist of anatase phase,

which shows that addition of activated carbon to titania prevents the transformation of anatase to rutile phase. Moreover, the addition of activated carbon to titania, results in the blue shift of light absorption, prevents the agglomeration of titania particles and reduces the grain size of titania.[117,118] Besides that, TiO_2(AC-700) also showed higher specific surface area (51 m^2g^{-1}) compared to bare titania (5 m^2g^{-1}). All these factors contributed to the improved photocatalytic activity of TiO_2(AC-700).[117]

Multi-walled carbon nanotubes (MWNT) have attracted considerable attention to improve the photocatalytic performance of titania due to their unique electronic properties and excellent electrical conductivities.[119] Preparing a composite of titania and MWNT could suppress the charge recombination within the composite due to electron scavenging ability and conductive nature of MWNT.[120] MWNT and titania composite was prepared via acid-catalyzed sol-gel method followed by calcination (400 ^oC) for 2 hours under N_2 atmosphere with the aim to improve the visible light activity of titania for phenol degradation.[121] It was observed that the composite (20-MWNT-TiO_2) prepared using 20wt% MWNT and 80wt% titania showed high photocatalytic activity for the degradation (95%) of phenol. Whereas, pristine titania showed 40% phenol degradation under the same conditions. The activity of pristine titania for phenol degradation might be related to the traces of UV light from the illumination source and the oxidation effect ascribed to the presence of dissolved oxygen in the reaction medium.[121] Whereas, the high photocatalytic activity of 20-MWNT-TiO_2 is due to the synergy between titania and MWNTS. Where, MWNT acted as a photosensitizer and inject electrons into the conduction band of titania upon visible light absorption (Figure 9a).[121,122] Simultaneously, back electron transfer from valence band of titania to MWNT result in the formation of hole (Figure 9b). These events triggered the formation of reactive oxygen species (ROS) such as superoxide radical anion $O_2^{-\bullet}$ and hydroxyl radical ($^\bullet$OH), which accomplished the degradation of phenol.[121]

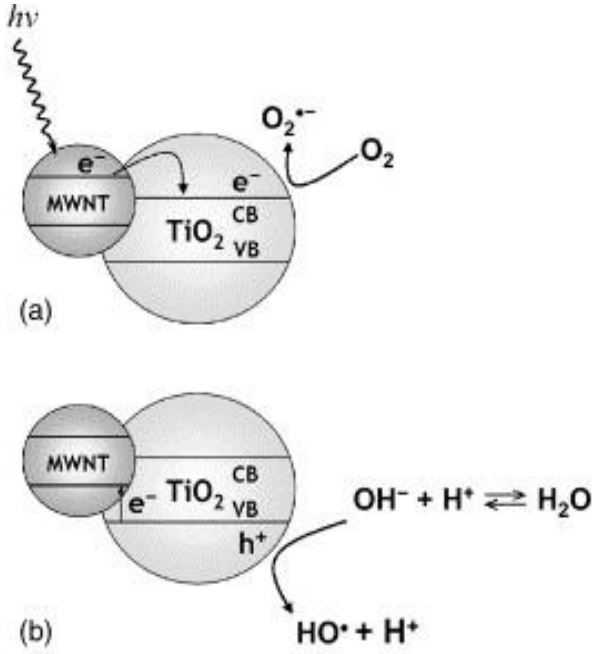

Figure 9. Multi-walled carbon nanotubes (MWNT) acting as photosensitizer in the composite catalyst: (a) electron injection into the conduction band of TiO_2 semiconductor; (b) electron back-transfer to MWNT with the formation of a hole in the valence band of TiO_2 semiconductor and reduction of the so formed hole by adsorbed OH^- oxidation. (Reprinted with the permission of ref.[121])

Biochar, a porous solid-rich byproduct of thermal decomposition of organic waste,[123] can possibly be used to improve the photocatalytic performance of titania. Biochar has number of advantages over conventional activated carbon such as the presence of surface functional groups (C–O, C=O, COOH, and OH). Besides that, the presence of sulphur and nitrogen containing functional group may also impart catalytic properties to biochar.[114] Lisowski et al.[5] prepared a composite from biochar (obtained from soft wood pellets (SWP) at 700 ^{O}C) and titania via sol-gel and ultrasound assisted method followed by calcination at 400 ^{O}C.[5] It was found that the composite (TiO_2/SWP700) prepared using ~20wt% of titania and ~80wt% of biochar (SWP700) exhibited high photocatalytic activity for the degradation (33%) of phenol under visible light (400-680

nm).[124] Whereas, the mechanical mixture of titania and biochar (SWP700) showed much lower activity (9%) for the degradation of phenol under visible light. The improved photocatalytic activity of TiO_2/SWP700 compared to physical mixture (titania + SWP700) ascribed to the narrower band gap (2.12 eV) of TiO_2/SWP700 composites, which enhanced the visible light harvesting. Besides that, the reduced recombination rate of photogenerated electron-hole pairs in TiO_2/SWP700 enhanced the photocatalytic efficiency.[5]

Chitosan (derived from the partial deacetylation of chitin) is a nitrogen-rich (~7 wt %) polymer, composed of repeating units of N-acetyl-D-glucosamine and D-glucosamine (Figure 10).[125,126] The presence of large number of amine and hydroxyl moieties in chitosan, may help to interact with titania for composite formation.[127] Besides that, chitosan may also act as nitrogen dopant for titania, which possibly improve the visible light harvesting of a chitosan-titania composite. Yan et al.[128] prepared visible light active chitosan-titania (CTS-TiO_2) nanocomposites via solvothermal method (180 °C for 12 hours) for the degradation of methylene blue (MB). The results showed that CTS-TiO_2 nanocomposite displayed a higher visible light photocatalytic activity for MB degradation compared to pure titania and commercial titania (P25). The apparent rate constant of the CTS-TiO_2 for MB degradation was 9.1×10^{-3} min^{-1}, which was greater than P25 (4.4×10^{-3} min^{-1}) and pure titania (4.3×10^{-3} min^{-1}). The enhanced photocatalytic activity of CTS-TiO_2 could be ascribed to the improved visible light harvesting of CTS-TiO_2 due to N-doping, and the efficient separation of the photo-generated electrons and holes pairs by carbon modification. Besides that, the carbon species in the CTS-TiO_2 may act as photosensitizers and the electron transport medium, and thereby improved the photocatalytic activity of CTS-TiO_2.[128,122]

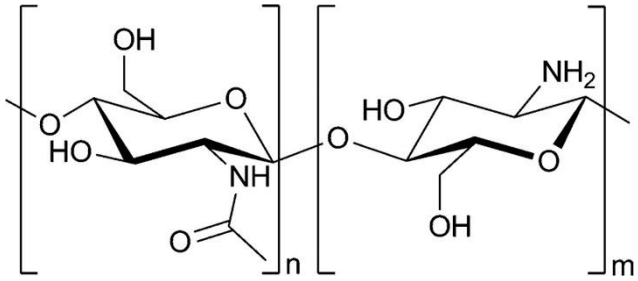

Figure 10. Chitosan, a linear polysaccharide composed of (1–4)-linked d-glucosamine and N-acetyl-d-glucosamine. (Reprinted with permission of ref.[125])

Lignin (derived from lignocellulosic waste) is a three-dimensional network macromolecular polymer composed of different polyphenolic units (Figure 11).[129,130] The presence of various functional groups (hydroxyl, methoxy, ether, and aldehyde groups) in lignin[129] offer great potential for the preparation of composite and photocatalytic materials.[123] The hydroxyl groups in lignin can involve in specific interactions with titania for the formation of composites.[131] Lignin has been used as a template to develop mesoporous titania nanoparticles via a hydrolysis precipitation method using $TiCl_4$ as precursor.[131] The highly electronegative hydroxyl groups in lignin display a strong affinity towards titanium atom, with comparatively low electronegativity (Figure 12).[131,114] During the partial hydrolysis of $TiCl_4$, the positively charged $Ti(OH)^{(4-n)+}_n$ were formed, which have tendency to react with nucleophilic ligand, resulting in adsorption on the surface of lignin through electrostatic forces of attraction. The adsorbed $Ti(OH)^{(4-n)+}_n$ subsequently hydrolyzed and converted to Ti–(O–lignin)$_4$ over the lignin surface. The well-dispersed titania nanoparticles were formed on the surface of the lignin after complete hydrolysis, (Figure 12).[131]

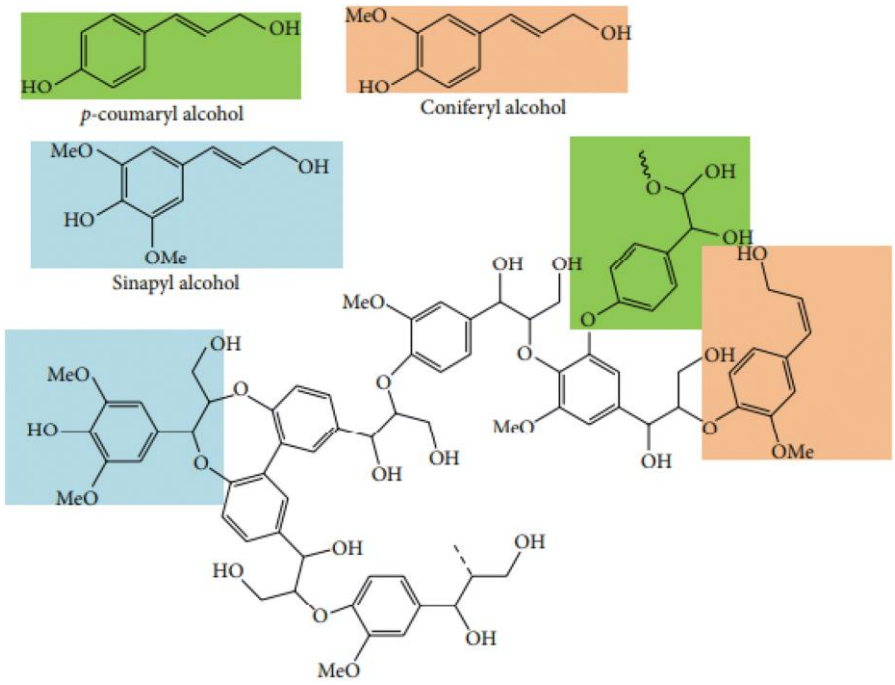

Figure 11. Cross-linked structures of lignin composed of phenolic monomers (p-coumaryl alcohol, coniferyl alcohol, and sinapyl alcohol). (Reprinted with the permission of ref.[130])

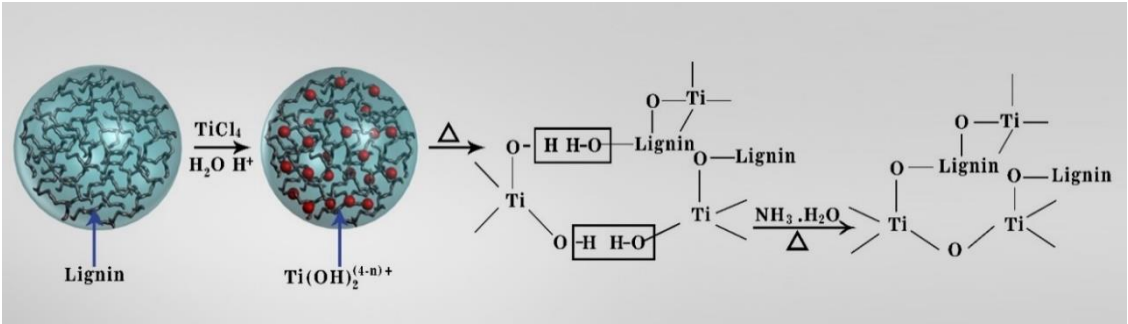

Figure 12. Formation mechanism of mesoporous titania with lignin as a template. (Adapted with the permission of ref.[131])

Moreover, the phenolic functional groups in lignin could improve the hole transport features of the composite materials.[132,133] Whereas, the aromatic rings in lignin may serve as chromophore site and assist in absorption.[134,135] specifically in the range of

295-400 nm.[136] Additionally, lignin may also act as a photosensitizer, and undergo a photoinduced electron transfer implying molecular oxygen and other substrate species, which result in the generation of reactive oxygen species (ROS) for example, superoxide radical anion ($O_2^{-\bullet}$) and hydroxyl radical ($^{\bullet}OH$).[137]

Chitosan and lignin exhibit number of beneficial properties, however, there are some limitations associated with the individual materials. For instance, chitosan, has low mechanical and thermal stability.[138] Furthermore, it is usually insoluble in neutral and basic pH range.[139] However, the lignin solubility in various solvents differs with the type of lignin. In the view of the fact, blending chitosan with lignin is a viable approach to obtain a biopolymer composite material with improved physicochemical properties. In an acidic medium, the amine groups of chitosan can easily be cationized,[140,114] which favors the interaction of chitosan with negatively charged materials. Adding, sulfonated lignin, as an anionic polymer into chitosan may help in the formation of ionic interaction between the two polymers,[141] which probably enhance the stability of the composite material.[142] Therefore, blending chitosan with lignin to prepare a composite for photocatalytic application is a captivating approach to benefit from the advantageous properties of both polymers and overcome the limitations of individual polymer.

Several methods have been reported to prepare chitosan-lignin (CL) composite, one of the most commonly used approach is the solvent cast method. In this technique, individual solutions of chitosan and lignin were prepared, subsequently mixed together and later by evaporating the solvents CL composite were formed.[143,144] Sonochemical technique has also been employed for the preparation of CL composites, in which chitosan suspension has been prepared and lignosulfonate particles were incorporated with the high intensity ultrasonic probe to obtain ionically cross-linked CL

composite.[142] Other approaches include reactive electrospinning process that involves the formation of polyelectrolyte solution of chitosan and lignin by controlling pH of the solution. Subsequently, the polyelectrolyte solution underwent electrospinning to acquire chitosan-lignin fibres.[141] Hydrothermal carbonization (a thermochemical process) is another potential method to prepare CL composite. The hydrothermal carbonization is carried out at relatively mild conditions at a temperature range of 180-280 °C under autogenous pressure in neutral/acidic/basic solutions,[145] which make it a sustainable process for preparation of CL composite. Moreover, the synthesis of CL composite through hydrothermal carbonization method, to the best of our knowledge has not yet documented.

Interestingly, the composite of chitosan and lignin (CL) is adaptable to couple with titania nanoparticles due to the presence of various functional groups.[146] In this context, preparing a nanocomposite by coupling CL composite with titania nanoparticles presents a possibility to improve the photocatalytic efficiency and the visible light activity of the titania. The varied functional groups of CL composite, especially aromatic groups of lignin, may enhance the substrate adsorption because of π-π stacking interaction with organic adsorbates, which is advantageous for enhancing the photocatalyst activity.[147] Whereas, nitrogen containing functional groups of chitosan may possibly improve the visible light harvesting of a titania via nitrogen doping.[126]

Numerous approaches have been used in the literature for the preparation of titania-based composites materials at nanoscale that include sol-gel method,[148,149,150] chemical vapor deposition,[151] hydrothermal method[152,153] and solvothermal method.[128] The sol-gel technique is the most widely used due to its simplicity and possible ability to control the surface properties of the composite. The sol-gel method involved the hydrolysis and polycondensation of a titanium alkoxide, which ultimately yields titanium dioxide (titania).[152] Titania obtained via sol-gel method is amorphous in nature, therefore titania

nanoparticles are subsequently calcined (400-700 ^{O}C) [5, 148,121] to acquire the crystalline phase of titania. However, calcination may lead to particle agglomeration, smaller specific surface area and rutile phase formation, which may result in lower photocatalytic activity of titania.[152] Moreover, the high temperature calcination (400-700 ^{O}C) is not an economical and sustainable approach. The hydrothermal treatment presents an alternative to the calcination for the crystallization of titania at mild temperatures (120-200 ^{O}C).[154, 155,156] Besides that, the characteristic features (grain size, particle morphology, crystalline phase, specific surface area and surface chemistry) of the titania nanoparticles can be adjusted by varying the experimental variables like pH, temperature, aging time, nature of solvent and additives.[155,157,158] Hydrothermal method provides a facile route for the synthesis of well-crystalline titania nanoparticles.[152] Moreover, to the best of our knowledge, the sol-gel-hydrothermal method has not been used for the preparation of titania/CL nanocomposite.

1.2 Valorization of biomass to value-added products

Biomass is considered as the most profusely available renewable resource. Globally, over 170 billion metric tons of biomass is produced every year.[159] Along with the increasing interest in exploring biomass for the preparation of photocatalytic material (as discussed in section 1.1.3.4), exploiting the biomass potential for the production of value-added chemicals and fuels is the key to a bio-based economy. Biomass mainly consist of cellulose (40–50%), hemicelluloses (16–33%), lignin (15–30%), and small fraction of other components.[160] Cellulose, a homopolymer of glucose (C-6 sugar) is recognized as the most economically beneficial, as it can be depolymerized into monosaccharide and glucose, which can subsequently be used as a precursor for other value-added chemicals by chemical or biochemical strategies. Unlike cellulose, hemicellulose is a hetropolymer consist of different monomers such as arabinose, mannose, galactose, glucose, and xylose.[161] Lignin is a complex polymer composed of

three-dimensional network of aromatic units connected through C−O−C ether bonds and C−C linkages.[162] It holds a significant potential for the production of aromatic compounds, however the recalcitrant nature of lignin structure makes its depolymerization quite challenging. The key problem associated with lignin valorization is the selective and effective cleavage of complex linkages which connect the aromatic units in the lignin structure.[162,163,164]

1.2.1 Conversion of 5-hydroxymethyl furfural (HMF) into value-added products

Biomass-derived sugars obtained from cellulose could be converted in to number of platform chemical such as furfural, 5-hydroxymethyl furfural (HMF), sorbitol, isorbide etc.[165] Among various building-block chemicals, 5-hydroxymethyl furfural (HMF) exhibit numerous application as intermediate compounds for the production of industrially relevant chemicals such as solvents, polymers, fuel additive lubricants, resins, decolorizing agents, drugs, fungicide etc.[166,167,168] The commercial production of HMF by acid-catalyzed hydrolysis-dehydration of C-5 sugars is well developed.[168,169,170] Interestingly, the versatile chemical reactivity of HMF ascribed to the presence of a hydroxyl group, an aldehyde group, and a furan ring offers great potential for the production of value-added products such as 2,5-diformylfuran (DFF), 2,5-furandicarboxylic acid (FDCA), 2,5-dimethyl furan (DMF), 5-hydroxymethyl-2-furancarboxylic acid (HMFCA), 5-formyl-2-furancarboxylic acid (FFCA), levullinic acid, maleic anhydride etc.[171,172,173,174] via hydrogenation, oxidation, polymerization, hydrogenolysis of C-O and dissociation.[175,176] However, partial oxidation of HMF is the most investigated process for the production of value-added derivatives of HMF.[177,178,179] As shown in Figure 13, the selective oxidation of hydroxyl functional group of HMF produces 2, 5-diformylfuran (DFF). Whereas, the selective oxidation of aldehyde functional group form 5-hydroxymethyl-2-furancarboxylic acid (HMFCA). Subsequent selective oxidation of DFF and HMFCA generate 5-formyl-2-

furancarboxylic acid (FFCA). With the further partial oxidation of the aldehyde group of FFCA, 2,5-furandicarboxylic acid (FDCA) is obtained.[176]

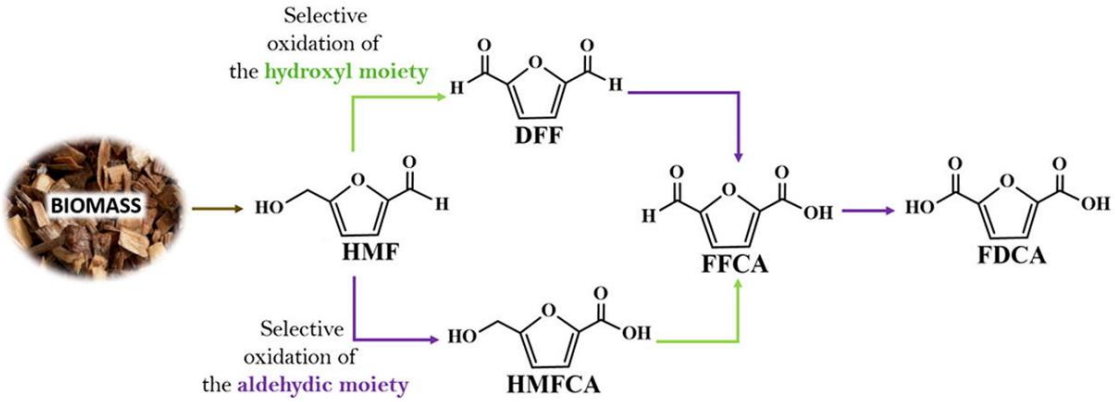

Figure 13. The pathways for the selective oxidation of 5-hydroxymethyl furfural (HMF) to 2, 5-diformylfuran (DFF), 5-hydroxymethyl-2-furancarboxylic acid (HMFCA), 5-formyl-2-furancarboxylic acid (FFCA) and 2,5-furandicarboxylic acid (FDCA). (Reprinted with the permission of ref.[176])

Among various value-added products derived from HMF, significant attention has been paid to the production of FDCA and DFF. FDCA has been identified among the top 12 building-block compounds derived from biomass by US Department of Energy. Interestingly, FDCA is a structural analogue of terephthalic acid, therefore considered as a viable substitute of terephthalic acid for the synthesis of different polymers like polybutyleneterephthalate (PBT) and polyethylene terephthalate (PET) plastics.[180,179] FDCA has enormous market potential, BASF and the Dutch technology firm Avantium is striving to develop a next generation bioplastics based on 2,5-furandicarboxylic acid (FDCA).[181,182]

In the recent years, the selective oxidation of HMF to FDCA is carried out over noble metal catalysts at high (80-150 ^{O}C) temperatures.[183,184] The major shortcoming of thermal catalytic oxidation methods include the high cost of expensive noble metal

catalysts, high energy consumption (due to high reaction temperatures) and high oxygen pressures (3-20 bar),[178,185] which hinders their large scale industrial applications. Hence, developing processes for the selective oxidation of HMF to FDCA under mild reaction conditions is a significant challenge. Heterogeneous photocatalysis is considered to be a relatively mild alternative approach for the selective oxidation of HMF to FDCA. Xu et al.,[185] reported that cobalt thioporphyrazine (CoPz) dispersed on graphitic carbon nitride (g-C_3N_4) showed exceptional photocatalytic activity for the selective oxidation of HMF to FDCA under simulated solar radiation (300-1000 nm) using molecular oxygen in air as an oxidizing agent, and alkaline reaction condition (pH = 9.18). High HMF conversion (99%) and FDCA selectivity (97%) was observed after 14 hours of illumination. [185]

DFF, another value-added product obtained from the selective oxidation of HMF has numerous applications for the preparation of drugs, pharmaceuticals, furan-urea resins, macrocyclic ligands, polymers, antifungal agents etc.[179,186] Numerous studies have been performed to selectively oxidize HMF to DFF using noble-metal catalyst, non-precious metal-containing catalyst, metal-organic frameworks (MOFs)-based catalyst. Baruah et al.[187] demonstrated that copper nanoparticles supported on cellulose, along with bismuth nitrate pentahydrate as a cocatalyst exhibit efficient catalytic activity for the selective oxidation of HMF to DFF in acetonitrile at 80 ^{O}C using air as an oxidant. High DFF yield (82%) with 85% HMF conversion was observed after 120 minutes.[187] Mesoporous manganese doped cobalt oxide catalyst (Meso 5%Mn/CoOx) showed the potential for the selective oxidation of HMF to DFF in different solvents such as toluene, acetonitrile, water, N,N-dimethylformamide (DMF) and 1,4-dioxane at 130 ^{O}C using air as an oxidizing agent after 4 hours. However, the Meso 5%Mn/CoOx catalyst showed best results in the presence of DMF, with 80% HMF conversion and 96% DFF

selectivity. Whereas, in aqueous medium moderate HMF conversion was achieved (70%) with high DFF selectivity (99%) at 100 ^{O}C after 4 hours.[188]

In the recent years, much emphasis has been given to heterogeneous photocatalytic approach for the selective partial oxidation of HMF to DFF, ascribed to its economical and environmentally-benign nature compared to thermocatalytic processes.[189,190,191] Melamine-derived graphitic carbon nitride (MCN) prepared via thermal (520 ^{O}C) condensation method demonstrated the reasonable potential for the photocatalytic selective oxidation of HMF to DFF in an aqueous medium. Moderate DFF selectivity (30%) was exhibited by MCN at 30% HMF conversion in an aqueous medium under UV-visible light (340-420 nm) irradiation. The thermal exfoliation of MCN at 540 ^{O}C further improved the DFF selectivity up to 45% at similar HMF conversion (30%). The improved photocatalytic performance of exfoliated MCN may ascribe to its relatively higher specific surface area (169 m^2g^{-1}) compared to non-exfoliated MCN (7 m^2g^{-1}). Moreover, thermal exfoliation of MCN may also improve the selectivity of DFF by eliminating the uncondensed NH_2 sites, which are considered detrimental for the partial oxidation of HMF to DFF.[192] Wu et al.[193] reported that graphitic carbon nitride (g-C_3N_4) obtained from the calcination (540 ^{O}C) of melamine showed better performance for the selective oxidation of HMF to DFF. The high DFF selectivity (~87%) was achieved by g-C_3N_4, with 31 % HMF conversion using molecular oxygen as oxidant in acetonitrile after 6 hours of illumination ($\lambda > 400$ nm). The photocatalytic selective oxidation of HMF over g-C_3N_4 in the presence of different radical scavengers revealed that the superoxide radical anion $O_2^{-\bullet}$ is the key active species involved in the oxidation of HMF (Figure 14). It was proposed that upon light irradiation, electrons are generated on the conduction edge, which reduced the oxygen to superoxide radical anion $O_2^{-\bullet}$. The $O_2^{-\bullet}$ preferably stays on the surface of g-C_3N_4, probably as an interface bound exciton pair to compensate for the positive charge within g-C_3N_4. The deprotonation of the hydroxyl

group of HMF (A) leads to the formation of alkoxide anion (B), which upon reaction with the hole by electron transfer form a radical (C). Further reaction of a radical (C) with hydroperoxyl radical (•OOH) forms the target product, DFF (D) and generate H_2O_2 as a side product (Figure 14).[193]

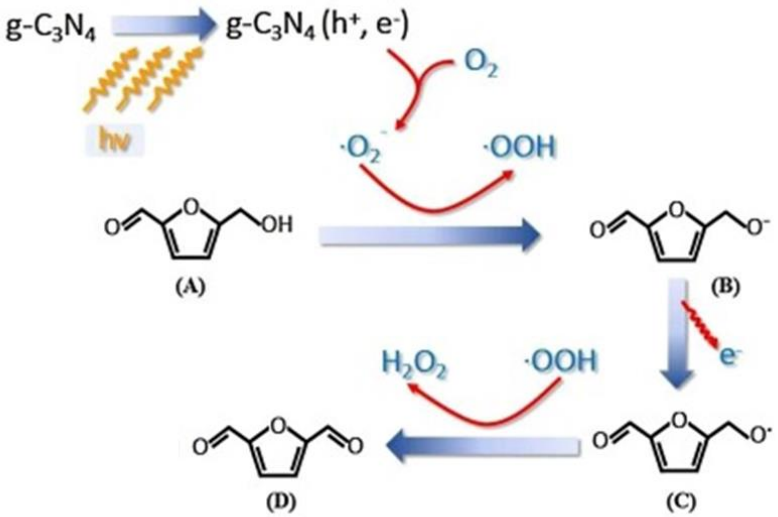

Figure 14. A possible reaction pathway for the photocatalytic selective oxidation of HMF to DFF over graphitic carbon nitride (g-C_3N_4). (Reprinted with the permission of ref.[193])

Zhang et al.[194] demonstrated the potential of niobium pentoxide (Nb_2O_5) obtained from the calcination (800 ^{O}C) of niobic acid for the selective oxidation of HMF to DFF under visible light ($\lambda > 400$ nm). A high DFF selectivity (~91%) was exhibited by Nb_2O_5 at low HMF conversion (~19%) in benzotrifluoride after 6 hours of illumination ($\lambda > 400$ nm). The mechanistic studies performed in the presence of radical scavenger showed that the holes (h^+) are the dominant active species involved in the oxidation of HMF to DFF. Based on radical scavenging experiments, a plausible mechanism has been proposed for the oxidation of HMF to DFF over Nb_2O_5 (Figure 15). The adsorption of HMF on Nb_2O_5 via hydroxyl group form alcoholate species, which is activated upon

visible light irradiation by injecting electrons in to the CB to reduce the Nb^{5+} to Nb^{4+}. Subsequently, alkenyl radical is formed, which is finally converted in to DFF, and water is formed as a side product. After the desorption of DFF the reduced Nb^{4+} is re-oxidized by the molecular oxygen.[194]

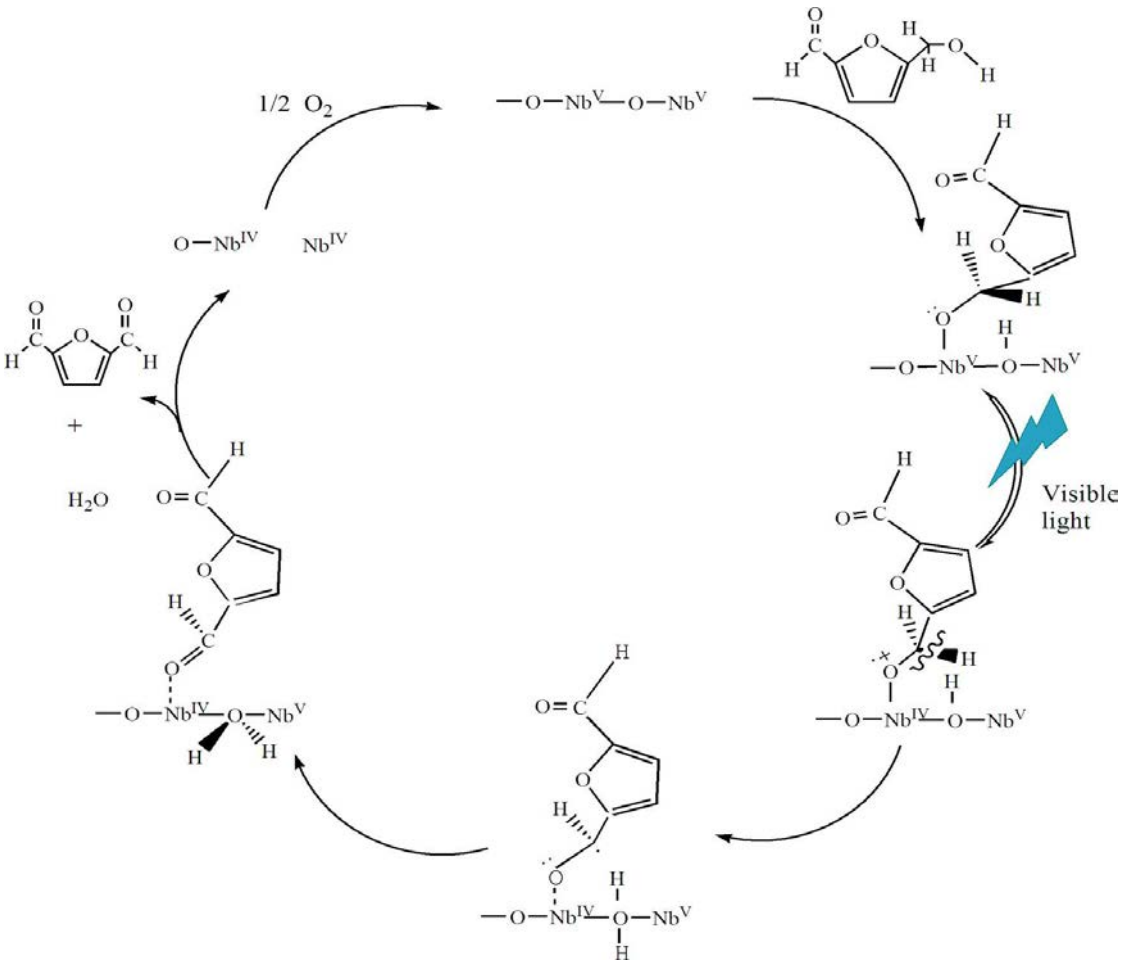

Figure 15. A possible reaction mechanism for the photocatalytic selective oxidation of HMF to DFF over Nb_2O_5. (Reprinted with the permission of ref.[194])

Though, these studies have demonstrated the practical applicability of visible light-driven photocatalytic selective oxidation of HMF to DFF. However, the synthesis of these photocatalysts (Nb_2O_5 and g-C_3N_4) is based on high-temperature calcination (800 ^{O}C and ~550 ^{O}C, respectively) method, which is not economical from sustainability point of view. Besides that, MnO_2 nanorods prepared through ultra-slow controlled

precipitation procedure using $KMnO_4$ as oxidant shown great potential for the selective oxidation of HMF under UV light (365 nm). The MnO_2 rods showed high HMF conversion (89%) and DFF selectivity (93%) in acetonitrile at 28 ^{O}C after 6 hours of illumination. A slight increase in temperature (from 28 to 39 ^{O}C) as a result of UV light irradiation (when experiment was performed without external cooling of reactor) acts synergistically with light irradiation and enhanced the photocatalytic activity of MnO_2, HMF conversion reaches up to 99% with ~100% DFF selectivity after 6 hours of illumination.[189] Although various studies carried out in the past showed that the photocatalytic approach has significant potential for the selective oxidation of HMF. However, the quest for a cost-effective, chemically stable and high performance visible light active photocatalyst is actively pursued to selectively oxidize HMF to DFF.

1.2.2 Conversion of benzyl alcohol (BnOH) into value-added products

Lignin, as one of the few renewable resources consisting of highly oxygenated polyphenolic units possess a significant potential for the production of value-added aromatic compound. Therefore, selective oxidation of lignin model compounds, which contains the functional groups found in native lignin has been the subject of intensive investigation.[195] The oxidation of benzyl alcohol (BnOH) has been used as a model reaction for the selective oxidation of lignin-derived aromatic alcohols. Besides that, the selective oxidation of BnOH to corresponding aldehyde or benzoic acid has immense application in pharmaceutical, cosmetics, perfumery, agrochemicals and flavor/fragrance industries.[196] Numerous photocatalytic systems have been developed for the selective oxidation of benzyl alcohol. Among various photocatalysts, titania and titania-based nanocomposite have been widely investigated for the selective oxidation of BnOH. [82,197,198] Magdziarz et al.[199] demonstrated that iron-containing TiO_2/Zeolite-Y photocatalyst synthesized through sonophotodeposition (SPD) method followed by calcination (300 ^{O}C) in air could be used for the selective oxidation of BnOH to

benzaldehyde (Bnald). High Bnald selectivity (>95%) was achieved with 48% BnOH conversion, by iron-containing TiO_2/Zeolite-Y photocatalyst in acetonitrile under solar simulated irradiation for 8 hours. Whereas, iron-containing TiO_2/Zeolite-Y photocatalyst obtained via ordinary wet impregnation (WI) method showed much lower activity for the selective oxidation of BnOH (10% conversion), with 90% Bnald selectivity. The enhanced photocatalytic performance of the nanocomposite obtained via SPD, ascribed to its improved visible light absorption (up to 700 nm) and reduced charge recombination due to the lower at.% of Fe (0.04) compared to the nanocomposite obtained from WI method (0.19 at.% of Fe).[199]

Band-gap alteration of titania via nitrogen doping is another approach used for the selective oxidation of BnOH under visible light. Zhang et al.[200] prepared a series of nanostructured N-doped titania by annealing the titania nanoparticles (synthesized via sol-gel and calcination method, 450 ^{O}C under O_2 flow) under pure NH_3 gas streams at various (400, 450, 500, 550 and 650 ^{O}C) temperatures for the selective oxidation of BnOH under visible light ($\lambda \geq 420$ nm). The optimal N-doped titania (containing 0.28 wt% N)[201] obtained at 500 ^{O}C showed ~20 % BnOH conversion and 100% Bnald selectivity in an aqueous medium after 2 hours of illumination. Whereas, the pristine titania showed negligible activity for the selective oxidation of BnOH (5% BnOH conversion, 100% Bnald selectivity) under visible light. The improved visible light activity of N-doped titania was attributed to the visible light absorption due to its reduced band-gap (2.28 eV) compared to pristine titania (~3.3 eV). Moreover, the electrochemical impedance spectroscopy (EIS) results showed that N-doping improved the charge separation efficiency, which also improved the visible light activity of N-doped titania for the selective oxidation of BnOH. Based on electron paramagnetic resonance (EPR) measurements the mechanism for the selective oxidation of BnOH over N-doped titania was proposed (Figure 16).[200] Upon visible light irradiation, the

photogenerated electrons (e^-) were scavenged by O_2 to form superoxide radical anion $O_2^{-\bullet}$, which subsequently form hydroperoxyl radical ($^\bullet$OOH). Whereas, the photogenerated holes (h^+) react with the deprotonated α-C-H group of BnOH and form a BnOH radical. Finally, the BnOH radical react with the hydroperoxyl radical ($^\bullet$OOH) radical and form Bnald.[200]

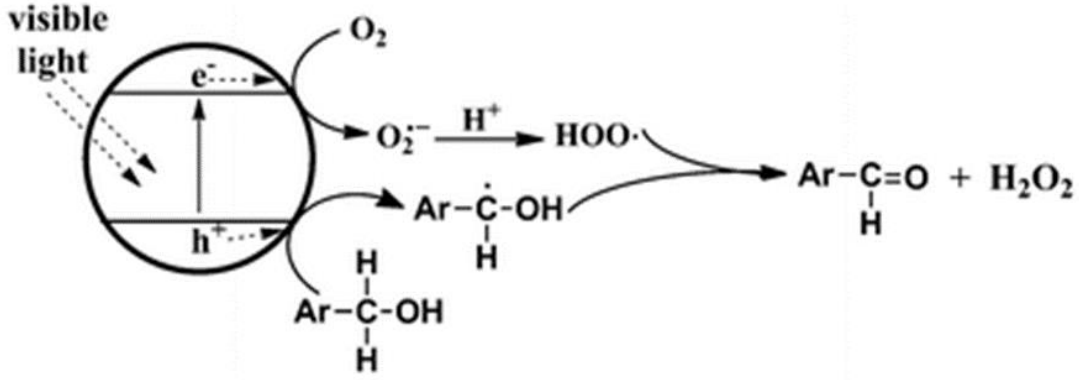

Figure 16. The proposed mechanism for the selective photocatalytic oxidation of benzyl alcohol (BnOH) to benzaldehyde (Bnald) under visible light irradiation. (Reprinted with the permission of ref.[200])

Tanaka et al.[202] prepared a visible light active Au/TiO_2 nanocomposite via colloid photodeposition (300 nm) with a hole scavenger (oxalic acid) method followed by calcination (973 K) for the selective oxidation of BnOH to Bnald. It was observed that Au/TiO_2 nanocomposite exhibit high Bnald selectivity (>99%) at >99% BnOH conversion in an aqueous medium using molecular oxygen as oxidant under red light ($\lambda > 600$ nm) after 12 hours of irradiation. Whereas, pristine titania showed negligible activity for the selective oxidation of BnOH under red light. The high photocatalytic performance of Au/TiO_2 nanocomposite compared to pristine titania ascribed to the surface plasmon resonance (SPR) of gold nanoparticles, which improved the photoabsorption of Au/TiO_2 nanocomposite.[202]

Though, the possibility of selective oxidation of BnOH under visible light especially under far visible region (red light) seems to be an attractive approach for the exploitation of renewable solar energy. On the contrary, high temperature calcination methods and use of expensive noble metal (gold) to achieve visible light activity limits their large-scale implementation for practical applications. Hence, there is a need for the sustainable processes for the valorization of biomass under visible light.

1.3 Prospects and challenges in titania-based photocatalysis for the selective oxidation of biomass-derived platform chemicals

There are several bottlenecks for the application of titania in organic oxidation reactions. However, the nonselective oxidation under UV light, which leads to poor product selectivity, is the biggest challenge associated with titania-based photocatalysis for the selective oxidation reactions. There are number of factors involved in the nonselective photocatalytic oxidation of organic substrates over titania. For instance, the formation of highly active oxidizing species especially in aqueous medium, which over oxidizes the substrate and often leads to mineralization and results in poor selectivity of the target product. Yurdakal et al.[203] reported that the photocatalytic selective oxidation of HMF over titania in an aqueous medium under UV light (365 nm) suffers from low DFF selectivity (22%) with 50% HMF conversion. The low selectivity of DFF by titania is ascribed to the generation of highly active oxidative species in aqueous medium such as hydroxyl radicals, which may destroy the furan ring and results in complete oxidation of HMF to CO_2 and H_2O (Figure 17).[203] Moreover, the reaction medium (solvent) can affect the conversion efficiency of the substrate and product selectivity either by competing with reactants and products for the catalytic centres or by solvating adsorbed species.[204]

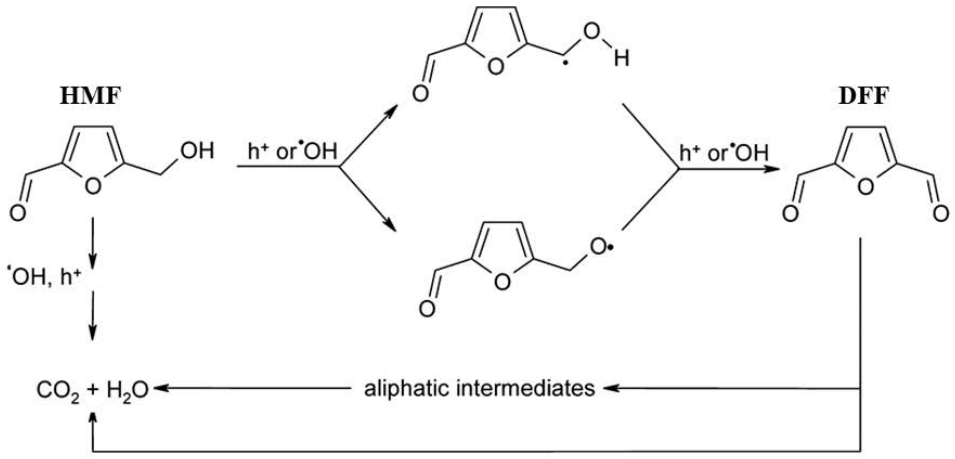

Figure 17. Mechanism for HMF oxidation to DFF over titania under UV light. (Reprinted with the permission of ref.[203])

Molinari et al.[83] demonstrated that the adsorption of geraniol and its subsequent photocatalytic oxidation to citral over titania (P25) is limited by the presence of water in the dispersing medium (acetonitrile). Interestingly, in anhydrous acetonitrile 3% adsorption of geraniol on titania (P25) was observed, which was slightly decreased (less than 1%) by adding small amount of water in the dispersing medium (ACN/H_2O 96/4). However substantial difference in the photocatalytic activity of titania (P25) for the oxidation of geraniol was observed in different reaction medium. In anhydrous acetonitrile, 73% selectivity of citral (at ~18% geraniol conversion) was observed after 35 minutes of illumination ($\lambda > 320$ nm). However, adding small amount of water in to acetonitrile (ACN/H_2O 96/4) reduced the selectivity of citral up to 50% (at ~11% geraniol conversion). It was proposed that the water as highly polar solvent increased the polarity of the dispersing medium (ACN/H_2O 96/4), which favours the interaction of geraniol with ACN/H_2O mixture. Moreover, ESR (electron spin resonance)-spin trapping investigation revealed that the competitive adsorption of water with geraniol inhibit the adsorption of geraniol on titania and subsequent oxidation.[83]

The characteristic feature of titania such as surface hydroxyl groups, specific surface area, crystallinity etc. also play a crucial role in determining the activity for the selective oxidation reaction. Higashimoto et al.[11,205] demonstrated the critical role of surface hydroxyl group of titania for the selective oxidation of BnOH to Bnald under blue light (λ >420 nm). It was found that the adsorption of BnOH on the surface of titania, involving surface OH groups result in the formation of LMCT-complex, which upon blue light absorption catalyzes the oxidation of BnOH to Bnald. A high BnOH conversion (>99%) with high Bnald selectivity (>99%) was achieved in acetonitrile using molecular oxygen as an oxidant after 4 hours of illumination. To corroborate the role of surface hydroxyl group of titania in the visible light active LMCT-complex formation, titania was treated at high temperature (~973 K) with the aim to remove the hydroxyl groups. The heat treatment drastically decreased the activity of titania for BnOH conversion (20%) with slight decrease in Bnald selectivity (~90%). The decrease in the activity of titania with heat treatment is ascribed to the removal of OH groups responsible for the adsorption of BnOH, and ultimately reduced the activity of titania. This was also evidenced by the surface fluorination of titania, that OH groups are critical for the adsorption of BnOH and visible light activity of titania. Moreover, the specific surface area of the titania (320 $m^2 g^{-1}$) was substantially reduced (up to 91 $m^2 g^{-1}$) after the heat treatment, which shows that the reduced number of active sites may also decrease the activity of titania.[11]

Crystallinity of titania is a crucial factor affecting the activity and selectivity of titania. It has been commonly observed that the higher degree of crystallization provides better separation of charge carriers. However, Augugliaro et al.[206] reported that less-crystalline rutile (HP333) phase of titania displayed better results for the selective oxidation of BnOH compared to more-crystalline rutile (HP973) and commercial P25 under UV light (λ = 360 nm). The HP333 sample showed 38% Bnald selectivity with

50% BnOH conversion, Whereas, HP973 exhibited ~10% Bnald selectivity at similar BnOH conversion (50%). Moreover, commercial P25 showed the four to five times lower Bnald selectivity (~8%) than HP333 at 50% BnOH conversion.[206] The enhanced selectivity of HP333 was ascribed to the facilitated charge recombination, and consequently hindered the generation of strong oxidizing •OH radicals. Besides that, OH groups formed from deactivated •OH radicals were preferred to adsorb on the less-crystalline rutile (HP333), creating a more hydrophilic surface. Desorption of Bnald was consequently improved, so was its selectivity.[206, 207]

In a nutshell, there are number of factors that influence the selectivity of desired product in titania-based photocatalysis, for example the intrinsic features of titania (crystallinity, specific surface area, number of surface OH groups, crystalline phase etc.) reaction medium, adsorption-desorption behavior of substrate and products. The literature review showed that different ways such as the use of relatively less polar solvent (compared to water) like acetonitrile may help improve the selectivity of the desired product, specifically in selective oxidation of alcohols over titania. This might be related to the reduced competition of solvent with the substrate for the adsorption site, which may improve the activity and selectivity of the titania. Moreover, acetonitrile would also minimize the formation of highly oxidizing •OH radicals, which often leads to the over-oxidation and poor selectivity of desired product. Additionally, the higher number of surface OH groups and greater specific surface area observed to improve the activity and selectivity of titania in selective oxidation reaction, which may have ascribed to the availability of increased number of adsorption sites/active sites for the substrate. Another challenge of titania-based photocatalysis in the selective oxidation reaction is the utilization of visible light. Titania is in principle active under UV light, but often poorly selective for the oxidation reaction under UV light. The literature review showed that different approaches such as doping (with metals or non-

metals), dye-sensitization, LMCT-sensitization, formation of composite (discussed in detail in section 1.1.3) etc. could be helpful in improving the visible light activity of titania. However, there is still a need for the improvement of visible light activity of titania to utilize solar energy efficiently, which allows the absorbance of a broader range of wavelengths (green and red light), using mild conditions (without the use of noble metal and high temperature (400-700 ^{O}C) calcination method).

2. RESEARCH HYPOTHESIS AND OBJECTIVES

From the current state of knowledge, it was inferred that the pristine titania has some limitations for its application in selective oxidation reaction. The foremost limitation is the requirement of UV light irradiation for its activity, which often lead to the low selectivity of partial oxidation products. This implies that more strategic approaches should be developed to extend the response of titania to the visible light region for the selective oxidation of organic substrates to high value-added products. On the basis of literature survey, two approaches have been used in this thesis for the visible light activation of titania for the selective oxidation of biomass-derived platform compounds i.e. i) Ligand-to-metal charge transfer (LMCT)-complex formation ii) Preparation of nanocomposites of titania and carbon materials.

2.1 Research hypothesis I

Ligand-to-metal charge transfer (LMCT)-complex formation: It is known from the literature that the furfuryl alcohol can be chemosorbed over titania and form a visible light-active surface-complex involving hydroxyl group. The surface-complex enables the oxidation of furfuryl alcohol to furaldehyde upon visible light ($\lambda \geq 420$ nm) irradiation.[109] This implies that the 5-hydroxymethylfurfural (a derivative of furfuryl alcohol), a platform compound with hydroxyl functional group could potentially be employed for the visible light ($\lambda = 515$ nm) activation of titania and self-selective oxidation via LMCT approach.

Following are the sub-hypotheses for the research hypothesis I.

i. It is hypothesized that 5-hydroxymethyl furfural (HMF) could adsorb on the titania surface and form a LMCT-complex, which can act as an in situ sensitizer and enable the selective oxidation of HMF to diformylfuran (DFF) under visible light ($\lambda = 515$ nm).

ii. It is hypothesized that the dissociative interaction of hydroxyl groups of HMF and the titania surface leads to the formation of LMCT-complex

iii. It is known from the literature that the higher specific surface area of titania may likely enhance the LMCT-mediated visible light photocatalytic activity of titania, ascribed to increased number of adsorption sites (hydroxyl groups).[11] It is therefore conjectured that the LMCT-mediated visible light photocatalytic activity of titania is correlated with its specific surface area.

iv. Referring to the current state of knowledge, it is presumed that the LMCT-complex formation between titania and HMF can extend the absorption of titania into the visible light region, which may facilitate the selective oxidation of HMF to DFF under visible light.

Following objectives were established to verify the research hypothesis I.

i. Understand the in situ sensitization of titania via LMCT-complex formation between HMF and titania, through various characterization techniques (Raman Spectroscopy, FTIR spectroscopy, DRS UV-Visible spectroscopy, XPS).

ii. Evaluate the role of surface hydroxyl group (OH) groups of titania in LMCT-mediated visible light activation of titania for the selective oxidation of HMF through heat treatment (to remove the surface hydroxyl groups) and surface fluorination (to replace the surface hydroxyl groups with F^- ions) of titania.

iii. Develop a mechanistic insight into the photocatalytic selective oxidation of HMF via LMCT-mediated activation of titania through radical scavenging experiments and by carrying out photocatalytic experiments in the presence of different additives.

iv. Investigate the effect of specific surface area on the activity of LMCT-activated titania for the selective oxidation of HMF to DFF.

2.1 Research hypothesis II

Preparation of nanocomposites of titania and carbon materials: The literature study showed that combining titania with carbon materials to form a composite at nanoscale could improve the visible light activity of titania.[121,124,128] In respect of selection of carbon material, the literature review revealed that chitosan and lignin exhibit number of advantageous properties,[127,129,131] and combining chitosan with lignin is a viable approach to obtain a biopolymer composite material with improved physicochemical properties. Subsequently, coupling titania with chitosan-lignin (CL) composite to prepare a nanocomposite (T/CL) can possibly improve the visible light (λ = 515 nm) activity of titania for the selective oxidation of benzyl alcohol (BnOH) to benzaldehyde (Bnald).

Following are the sub-hypotheses for the research hypothesis II.

i. According to literature survey, chitosan and lignin have some inherent flaws, it is hypothesized that combining chitosan with lignin may form a composite with improved physicochemical properties.

ii. It is presumed that CL composite bearing multiple functional groups may potentially interact with titania nanoparticles and form a nanocomposite.

iii. It is known from the literature that lignin may act as a photosensitizer,[137] therefore it is hypothesized that CL as part of nanocomposite (T/CL) may act as a photosensitizers and electron transport medium, and thereby improved the visible light activity of titania for the selective oxidation of BnOH.

iv. Referring to the literature survey, chitosan may act as a nitrogen dopant.[128] It is therefore conjectured that CL composite may incorporate nitrogen in to the titania lattice and form a new-mid-gap energy state, which may decrease the

band-gap of titania and improve the visible light activity of titania for the selective oxidation of BnOH.

Following objectives were established to verify the research hypothesis II

i. Design a low temperature (hydrothermal) synthesis route for the preparation of chitosan-lignin (CL) composite.

ii. Develop a low temperature (150 °C) synthesis method utilizing sol-gel and hydrothermal techniques for the preparation of titania/chitosan-lignin (T/CL) nanocomposite.

iii. Understand the synergy of titania and chitosan-lignin composite by characterizing them through wide range of techniques, e.g. X-ray diffraction (XRD), N_2 physisorption, FTIR spectroscopy, DRS UV-Visible spectroscopy, and X-ray photoelectron spectroscopy (XPS) for the visible light activation of T/CL nanocomposite for the selective oxidation of benzyl alcohol (BnOH) to benzaldehyde (Bnald).

3. EXPERIMENTAL

This chapter includes the work published in ChemSusChem and the work submitted for publication in RSC Advances.

Chemicals: Titanium(IV) isopropoxide (97+%, Sigma Aldrich), nitric acid (65%, Alfa aesar), 2-propanol (99.7%, Alfa aesar), commercial titanium(IV) oxide, P25 (99.5%, Evonik), brookite (99.9%, Sigma Aldrich), 5-hydroxymethylfurfural (98%, Acros Organics), acetonitrile (99.9%, POCH), anatase (98%, Acros Organics), 2,5-diformylfuran (98%, abcr), methanol (99.9%, POCH), sodium acetate (99.0% Chempur), sodium fluoride (99%, Chempur), 1,4-benzoquinone (98%, Sigma Aldrich), silver nitrate (99.8%, STANLAB), potassium trioxalatoferrate (III) trihydrate (98%, abcr), 1,10–phenanthroline (99.5%, Chempur), citric acid monohydrate (≥99.0 %, STANLAB), alkali lignin, low sulfonate content (average Mw ~10,000, 4% sulfur, Sigma Aldrich), medium molecular weight chitosan (75-85% deacetylated, Sigma Aldrich), orthophosphoric acid (85%, POCH), sodium sulfate (>99%, ROTH), benzyl alcohol (99.8%, Sigma Aldrich), benzaldehyde (99.0%, Chempur), dimethylsulfoxide (>99.5%, ROTH), Nafion (~5% in a mixture of lower aliphatic alcohols and water, Sigma Aldrich), and active carbon Norit® SX 2 (POCH) were used without further purification. Water used was purified up to 18 MΩ cm resistivity via Milli-Q water purification system.

3.1 In situ LMCT-sensitization of titania and its photocatalytic activity

3.1.1 Synthesis of titania nanoparticles

Titania nanoparticles were prepared via sol-gel and hydrothermal method adapted from the literature.[49,208] A titania sol was prepared by acid-catalyzed hydrolysis of titanium(IV) isopropoxide (TTIP). In a typical procedure, a specified volume of TTIP (30.5 mL) was dissolved in 25 mL of 2-propanol and stirred (400 rpm) at room

temperature for 2 hours. Subsequently, 1M nitric acid (1 mL) was added to the prepared solution under continuous stirring (for 5 minutes) till gelation takes place. Then, water (25 mL) was slowly added to the gel and stirred (400 rpm) for additional 3 hours. Afterwards, the synthesized titania nanoparticles were filtered, washed three times with water, and subsequently dried at 80 ^{o}C in hot air oven for 12 hours. The dried titania nanoparticles were ground to powder and shifted to a Teflon lined autoclave filled with water (~80%) for hydrothermal (150 ^{o}C) treatment for 8 hours. Finally, the obtained titania nanoparticles named as SGH-TiO_2, were dried in hot air oven at 110 ^{o}C for 12 hours.

Preparation of sensitized titania nanoparticles: For the preparation of sensitized titania nanoparticles (HMF-adsorbed titania nanoparticles, HMF-Ads-SGH-TiO_2), a specified amount (20 mg) of SGH-TiO_2 is suspended in 20 mL of 1 mM HMF solution in acetonitrile in the glass photoreactor. The resulting suspension was stirred (400 rpm) in dark for 1 hour. Afterwards, the HMF-Ads-SGH-TiO_2 was collected, dried in hot air oven at 80 ^{o}C for 3 hours and characterized further. HMF-adsorbed P25 (HMF-Ads-P25) was prepared following the same procedure. However, for the photocatalytic experiments the catalyst was not removed and the light experiment was started after 1 hour of stirring in dark.

Chemical and thermal modification of titania nanoparticles (SGH-TiO_2): The synthesized SGH-TiO_2 nanoparticles were further modified through chemical (surface-fluorination) and thermal treatment to exchange or remove the surface hydroxyl (OH) groups, respectively. Thermal modification involves high temperature calcination (600 ^{o}C) of SGH-TiO_2 for 3 hours under static air at a heating ramp of 5 ^{o}C /min.[11] Thermally modified SGH-TiO_2 nanoparticles were named as SGH-TiO_2-cal-600. Whereas, surface-fluorinated titania (F-SGH-TiO_2) nanoparticles were prepared according to the

method reported by Park and Choi [209] with some modifications. An aqueous solution of sodium fluoride (0.05 M) was prepared and the pH of the sodium fluoride solution was maintained to ~3.5 using HCl. Afterwards, 0.06 g of SGH-TiO_2 were suspended in sodium fluoride solution (6 mL) and stirred at room temperature for 5 hours to exchange the surface OH groups of SGH-TiO_2 with fluoride ions. Afterwards, the fluorinated SGH-TiO_2 (F-SGH-TiO_2) were collected and dried in hot air oven at 110 °C for 12 hours.

3.1.2 Characterization of titania nanoparticles

Powder XRD measurements for the titania samples were carried out by applying Bragg-Brentano configuration. This type of configuration has been provided by means of Empyrean diffraction platform, Malvern PANalytical Co., powered at 40 kV × 40 mA and furnished with a vertical goniometer, using theta-theta geometry applying nickel filtered Cu Kα radiation. Data were collected in range of 2θ = 9°-100°, with 0.008° step size, and counting time 60 second per step. The percentage phase composition of titania samples were estimated through the Rietveld refinements of the XRD patterns. Whereas, the average crystallite size of titania samples was calculated using Scherrer equation (Equation 1), where D is the average size of the crystallite (nm), λ is the Cu kα X-ray radiation wavelength (λ = 0.154056 nm), k is a coefficient taken as 0.94, β is the full width at half maximum intensity (FWHM) of the peak observed at 2θ (radian), and θ is the diffraction angle.

$$D = \mathrm{k}\,\lambda\,/\beta\mathrm{Cos}\theta \quad \text{(Equation 1)}$$

The textural features such as specific surface area and pore width distribution of the titania samples were studied via N_2 physisorption isotherms by employing Brunauer-Emmet-Teller (BET) and Barrett, Joyner, Halenda (BJH) method, respectively. The N_2 physisorption measurements were performed at Micrometrics ASAP 2000 automated

system. The FTIR spectrum of titania samples was measured on Bruker ATR spectrometer in the transmittance mode, within the range of 4000-400 cm^{-1}, with 16 scans and a resolution of 4 cm^{-1}. DRS-UV-Visible absorption spectrum were recorded by means of Jasco V-570 UV/VIS/NIR spectrophotometer equipped with an integrating sphere. The baseline has been recorded using a reference material, Spectralon™ (poly(tetrafluoroethylene)). Band-gaps values of titania samples were estimated using Tauc plot by applying Kubelka-Munk function. The non-polarised Raman spectra were recorded using Renishaw micro-Raman system equipped with an integrated Leica microscope, in the back scattering geometry. The infrared solid state laser (785 nm), powered at 20 mW was used as a source of excitation light. Laser beam was focused on the titania sample through the objective of 20x/0.4NA, the spatial resolution was about 2 μm. The titania samples were scanned in 3 spectral range: i. 100 -1000 cm^{-1} (I), 1000-2000 cm^{-1} (II) and from 2750 -3450 cm^{-1} (III) with 1 cm^{-1} spectral resolution. The Rayleigh radiation was blocked by a holographic notch filter. The backscattered Raman-light has been dispersed by 1800 mm^{-1} (785 nm) holographic grating on the Peltier cooled CCD. All the measurements were recorded at ambient temperature. Artefacts from cosmic ray have been eliminated and spectra analyses was performed on Bruker OPUS software. The leaching of titanium ion after the photocatalytic reaction was determined using the energy dispersive X-ray fluorescence analysis (EDXRF), carried out using MiniPal 4 equipment from PANalytical Co, with a Rh-tube and silicon drift detector (resolution 145 eV) to assess the elemental composition of liquid samples. The spectrum was recorded in atmosphere without using any filters, at a 30 kV tube voltage in order to detect the presence of Ti. The acquisition time was set to 600 seconds and the tube current ~50 μA. X-ray photoelectron spectroscopy (XPS) measurements were carried out in a PHl 5000 VersaProbe™ – spectrometer (ULVAC-PHI, Chigasaki Japan). The XPS spectra were recorded using monochromatic Al-Kα

radiation (hν = 1486.6 eV) from an X-ray source operating at 15 kV, 25 W and 100 µm spot size. Both high resolution (HR) and survey XPS spectra were recorded with the analyser pass energy of 117.4 eV and 23.5 eV with the energy step size of 0.4 and 0.1 eV, respectively. The Casa XPS software (v.2.3.19, Casa Software Ltd.) was applied to analyse the XPS data. The Shirley background subtraction and fitting of peak with Gaussian-Lorentzian shaped profiles has been applied on XPS data. The binding energy (BE) scale has been referenced to the C 1s peak with binding energy = 284.8 eV. The PHI Multipak sensitivity factors and estimated transmission function of the spectrometer were applied for quantification. The fluorine content in fluorinated SGH-TiO_2 (F-SGH-TiO_2) was estimated using elemental analyzer (UNICUBE). The high resolution TEM (HR-TEM) measurements were performed on FEI Talos F200X transmission microscope at 200 kV. In order to estimate the particle size more than 200 particles were counted.

Hydroxyl (OH) group density measurement: The hydroxyl (OH) group density of titania samples were estimated through thermogravimetric analysis (TGA) weight loss, using a thermobalance (Mettler Toledo TGA/DSC 3+). The method applied for TGA analysis[210,211] involved two steps. In the 1st step, the samples were heated under air flow (40 mL/min) from 25 to 120 °C at a ramp of 5 °C/min and held at this temperature for 3 hours to remove the physically bound water from the titania surface. In the 2nd step, the temperature was increased up to 750 °C at a heating rate of 10 °C/min and held for 1 hour. The mass loss occurred during the 2nd step was used to estimate the number of OH groups per surface area using the following formula (Equation 2)[212]:

$$OH/_{nm^2} = \alpha \frac{2(m_T - m_c)\frac{N_A}{MH_2O}}{10^{18} \times SSA} \qquad (Equation\ 2)$$

The m_T is the mass loss per mg of the catalyst between the temperature range of 120-750 ºC, m_C is the mass loss per mg of the sample due to carbon content (based on the evolved CO_2), SSA is specific surface area (m^2g^{-1}), MH_2O is the molar mass of H_2O in $gmol^{-1}$, α is the calibration constant (0.625)[211,212] and N_A is Avogadro's constant (mol^{-1}).

The carbon content in titania samples were determined via temperature programmed oxidation (TPO) experiments. The samples were heated from 25 ºC to 120 ºC at a heating ramp of 5 ºC/min under air flow (25 mL/min), with the 3 hours of holdup time. Then, samples were cooled down to room temperature and then heated from 25 ºC to 750 ºC, with the heating ramp of 10 ºC/min under air flow (25 mL/min). The oxidation of titania samples was analyzed by quadrupole-mass-spectrometer (QMS) Dycor Ametek. The carbon content was estimated from the CO_2 signals of the QMS, calibrated using CO_2 (with the pulse of 1.01×10^{-5} mol).

3.1.3 Evaluation of the photocatalytic activity of LMCT-sensitized titania for the selective oxidation of 5-hydroxymethylfurfural (HMF)

Photocatalytic selective oxidation of 5 Hydroxymethylfurfural (HMF): The photocatalytic selective oxidation of HMF was performed in a glass photoreactor (20 mL). In a typical experiment, 1mM (0.02 mmoles) HMF solution in acetonitrile (20 mL) and 20 mg of SGH-TiO_2 photocatalyst (1g/L) was added into a glass photoreactor. Afterward, the suspension was stirred at 400 rpm in the dark for 1 hour to attain the equilibrium in dark. The photocatalytic reaction began with the irradiation of green LED lamp (λ= 515 nm). The intensity of the LEDs was measured to be 6 x ~9 W/m^2, determined via light meter (Delta OHM HD 2302.0) with LP 471 RAD probe having 400-1050 nm spectral range. In addition, the selective oxidation of HMF was also carried out under UV light using UV LED lamp (λ= 375 nm) having similar intensity (6 x ~9 W/m^2) as green LED lamps, measured by a Delta OHM HD 2302.0 light meter

with a LP 471 UVA probe having a spectral range of 315-400 nm. The distance between the photoreactor wall and the irradiation source is ~2 mm. At given illumination time intervals, 0.15 mL aliquots were collected, and subsequently filtered via nylon filter (0.2 μm pore size) to remove the photocatalyst. The same experiments were performed with commercial titania (P25 and P90) photocatalyst. The experimental set-up used for the photocatalytic experiment is shown in Figure 18a

Recycling of the SGH-TiO_2: After each run the *SGH-TiO_2* was recovered by decanting the solvent washed three times with water, dried in hot air oven for 48 hours at 110 ^{o}C and used again in the next run with fresh HMF solution. This procedure was repeated up to five times of application.

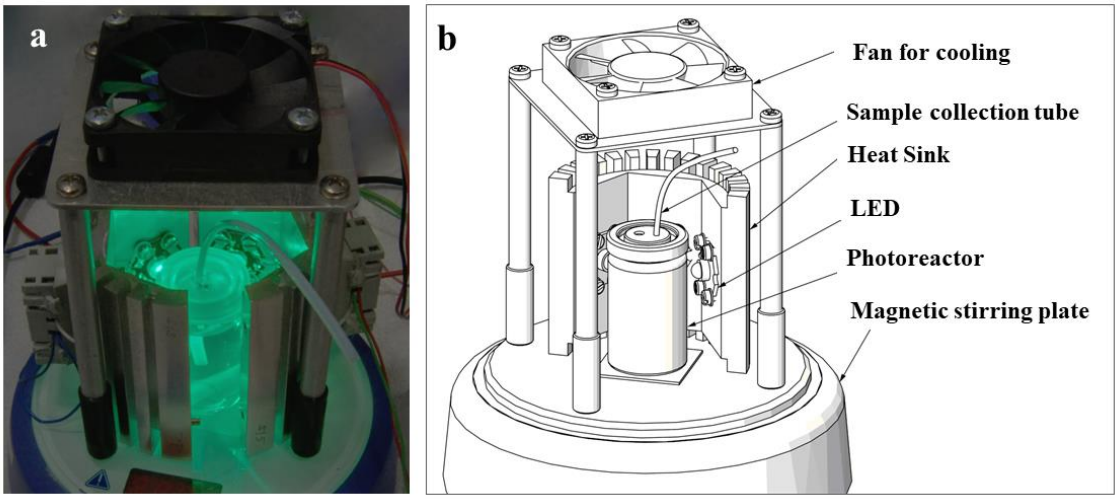

Figure 18. a) Experimental setup used for the photocatalytic experiments under visible light. b) Vertical cross-section view of photocatalytic set-up

Analysis of HMF oxidation reaction: The quantitative analysis of products and reactants was performed on Waters 2487 high-performance liquid chromatography (HPLC) instrument equipped with C18 Thermo scientific column (250 x 4.6 mm), using an eluent consist of acetonitrile (55%) and Milli-Q water (45%) at a 1 mL/min flow rate. The column oven temperature was set at 25 ^{o}C. The HMF conversion (Equation 3) and DFF selectivity (Equation 4) were determined as follows:

$$\%HMF\ Conversion\ = \frac{M^{o}_{HMF} - M_{HMF}}{M^{o}_{HMF}} \times 100 \qquad Equation\ 3$$

$$\%DFF\ Selectivity = \frac{M_{DFF}}{M^{o}_{HMF} - M_{HMF}} \times 100 \qquad Equation\ 4$$

Where M^{o}_{HMF} refers to the initial amount of HMF in mmoles, whereas M_{HMF} *and* M_{DFF} corresponds to the amount of HMF (mmoles) and DFF (mmoles) after the photocatalytic reaction.

For the detection of side products, the liquid samples were analyzed on Agilent 7890A & 5975C GC/MS system, equipped with HP-5MS column (30 m x 250 µm x 0.25 µm). The temperature of the inlet was set at 250 °C, and the column temperature was increased from 40 to 320 °C with 10 °C/min ramp rate. The injection volume used was 1 µL in a split less mode.

Adsorption sites and HMF conversion per surface OH group: The number of OH groups and conversion (conv.) of HMF with reference to area and adsorption sites of titania samples were calculated as follows.

$$Area\ normalized\ conv. = \frac{number\ of\ molecules\ of\ HMF_{conv.}}{SSA\ \times\ m_{cat}} \qquad (Equation\ 5)$$

$$Area\ normalized\ rate = \frac{number\ of\ molecules\ of\ HMF_{conv.}}{SSA\ \times\ m_{cat}\ \times \text{time}} \qquad (Equation\ 6)$$

$$number\ of\ OH\ groups = D_{OH} \times SSA\ \times\ m_{cat} \qquad (Equation\ 7)$$

$$Conv.\ per\ surface\ OH\ groups\ = \frac{number\ of\ molecules\ of\ HMF_{conv.}}{number\ of\ OH\ groups} \ (Equation\ 8)$$

$$Conv.\ per\ surface\ OH\ groups\ per\ unit\ time\ = \frac{number\ of\ molecules\ of\ HMF_{conv.}}{number\ of\ OH\ groups\ \times time} \ (Equation\ 9)$$

Where, area normalized conv. is the conversion of HMF per m^2 of the catalyst (m^{-2}), while area normalized rate is the conversion of HMF per m^2 per unit time ($m^{-2}s^{-1}$), SSA

is the specific surface area (m^2g^{-1}) of photocatalyst, m_{cat} is the mass of the photocatalyst (g) and D_{OH} is the density of OH groups per m^2 of the photocatalyst.

Apparent quantum yield (AQY) measurement: The apparent quantum yield (Φ) for the DFF production is defined as the ratio of the amount of DFF formed per unit time to the number of photon absorbed by the system per unit time (Equation 10).

$$\Phi = \frac{Number\ of\ moles\ of\ DFF\ produced\ per\ unit\ time}{Number\ of\ photons\ (Einstein)\ absorbed\ per\ unit\ time} \times 100 \quad (Equation\ 10)$$

To determine the apparent quantum yield (Φ), the photon flux to the photoreactor was calculated by potassium ferrioxalate actinometry.[213,214,215,216] The Actinometry experiments were carried out in a dark room under green LED lamp (515 nm) with an intensity of 6 × ~9 W/m^2. In a typical procedure, 0.15 M potassium ferrioxalate solution (20 mL) was charged into a glass photoreactor used for the photocatalytic experiments. Then the actinometer solution was illuminated for 30 s while stirring (400 rpm). At the same time, another sample prepared following the same procedure was left in the dark as a control. Upon completion of illumination an aliquot (3 mL) of 0.15 M potassium ferrioxalate was taken in glass vials and then 0.1% buffered 1,10-phenanthroline solution (500 μL) was added to irradiated and non-irradiated samples. The samples were then allowed to develop for half an hour in the dark. After that, the absorption of each of the sample was recorded on Thermoscientific Evolution 220 UV Vis Spectrophotometer at 510 nm. The amount of Fe^{2+} produced during the illumination is measured using the optical difference (ΔA_{510nm}) between the illuminated and control sample (prepared in dark) and the extinction coefficient at 510 nm (ε = 11,100 M^{-1} cm^{-1}).

The quantum yield for Fe^{2+} production is 1.0, the photon flux absorbed by the sample per unit time is estimated using the following formula (Equation11).[216] Where t is the irradiation time in seconds and F is the fraction of light absorbed.

$$\frac{Nhv}{t} = \frac{moles\ of\ Fe^{2+}}{\Phi\ \ t\ F} \quad (Equation\ 11)$$

3.2 Titania/chitosan-lignin nanocomposite and its photocatalytic activity

3.2.1 Synthesis of chitosan-lignin (CL) composite

CL composites were synthesized in different weight ratios (10:90, 25:75, 50:50, 75:25 and 90:10) through the following method. At first, 0.5 wt% chitosan solution was prepared in aqueous citric acid (0.2 M) solution (100 mL) and stirred (800 rpm) well for 2 hours to get a homogeneous solution. A known mass of lignin was introduced in to as prepared chitosan citric acid solution and stirred (800 rpm) for 2 hours. Subsequently, the brown suspension formed was transferred to a Teflon equipped stainless steel autoclave, which was then placed in an oven followed by hydrothermal treatment (200 ℃) for 12 hours. Afterwards, the autoclave was cooled down naturally at room temperature. The blackish brown suspension obtained was filtered, and the precipitates were washed with water and 2-propanol twice and then dried in an oven (80 °C) for 12 hours. The obtained CL composites were named as CL(10:90), CL(25:75), CL(50:50), CL(75:25) and CL(90:10).

3.2.2 Synthesis of titania sol

A titania sol was prepared by acid-catalyzed hydrolysis of titanium(IV) isopropoxide (TTIP).[49] In a typical procedure, a specified volume (9.077 mL) of TTIP was dissolved in in 25 mL of 2-propanol and stirred (400 rpm) at room temperature for 2 hours.

Subsequently, 1M nitric acid (1 mL) was added to the prepared solution under continuous stirring (400 rpm for 5 minutes) till gelation takes place. Then, water (25 mL) was slowly added to the gel and stirred (400 rpm) for additional 3 hours.

3.2.3 Synthesis of titania/chitosan-lignin (T/CL) nanocomposites

To prepare the T/CL nanocomposites with the weight fraction of 75/25 (75wt% titania/ 25wt% CL composite), the prepared titania sol was introduced into a suspension of CL composite (0.8 g) in 160 mL of water, while stirring (600 rpm) at room temperature. The resulting suspension was stirred for 5 hours, then filtered, washed with water and dried in oven (80 ^{O}C) for 12 hours. Afterwards, the obtained solid sample was ground to powder and then shifted to Teflon lined autoclave filled (~80%) with water for hydrothermal treatment (150 °C) for 8 hours. Finally, the nanocomposite obtained named 75T/CL was dried in hot air oven (110 ^{O}C) for 12 hours. Following the same procedure, a series of nanocomposites were prepared using CL composites synthesized in various weight ratios (10:90, 25:75, 50:50, 75:25 and 90:10). The optimization of titania content in the nanocomposite is given in Appendix (Section A4). For the purpose of comparison, an activated carbon (Norit)-based nanocomposite (75T/Norit), lignin-based nanocomposite (75T/L) and chitosan-based nanocomposite (75T/C) were also synthesized using the same sol-gel and hydrothermal route. Furthermore, to elucidate the effect of titania content higher than 75wt%, a series of nanocomposites was also synthesized by increasing the titania content (85wt%, 95wt% and 99wt%) for the selected CL composite (CL(25:75)). A specified volume of TTIP, equivalent to the definite wt% of titania (85wt%, 95wt% and 99wt%) was used to synthesize the titania sol, and the synthesized nanocomposites were named as, 85T/CL(25:75), 95T/CL(25:75) and 99T/CL(25:75), respectively.

3.2.4 Characterization of CL composites and titania/chitosan-lignin (T/CL) nanocomposite

The CL composites morphology was evaluated by FEI Nova Nanolab 200 scanning electron microscopy (SEM) at 15 kV accelerating voltage. The X-ray diffraction (XRD) measurements for CL composite and T/CL nanocomposite were performed following the same procedure used for the XRD analysis of SGH-TiO_2 (see section 3.1.2 for details). The textural properties of CL composites and T/CL nanocomposites were measured through N_2 physisorption isotherms by applying Brunauer-Emmet-Teller (BET) and Barrett, Joyner, Halenda (BJH) method. The measurements for CL composites and T/CL nanocomposite were carried out at Micrometrics ASAP 2000 automated system and Micrometrics ASAP 2020 automated system, respectively. The FTIR measurements and Diffuse reflectance UV-Visible spectroscopy measurements for CL composite and T/CL nanocomposite were performed following the same procedure applied for the analysis of SGH-TiO_2 (see section 3.1.2 for details). Elemental analysis of the samples has been carried out on Thermo Scientific Flash 2000 Organic Elemental Analyzer. X-ray photoelectron spectroscopy (XPS) experiments were performed in a PHl 5000 VersaProbe^{TM} – spectrometer (ULVAC-PHI, Chigasaki Japan). The XPS spectra were recorded using monochromatic Al-Kα radiation (hν = 1486.6 eV) from an X-ray source operating at 100 μm spot size, 25 W and 15 kV. Both survey and high-resolution (HR) XPS spectra were collected with the analyser pass energy of 117.4 eV and 23.5 eV with the energy step size of 0.4 and 0.1 eV, respectively. The Casa XPS software (v.2.3.19, Casa Software Ltd,) was used to analyse the XPS data. The Shirley background subtraction and fitting of peak with Gaussian-Lorentzian shaped profiles has been performed. The binding energy (BE) scale was referenced to the C 1s peak with binding energy = 284.8 ± 0.2 eV and Ti $2p_{3/2}$ peak with binding energy = 458.6 ± 0.2 eV. For quantification the

PHI Multipak sensitivity factors and determined transmission function of the spectrometer were used. Thermal stability of CL composites was examined using thermogravimetric analysis (TGA) carried out on Netzsch STA 409 TG/DTA device. The samples were analyzed under N_2 flow (75mL/min) with the heating ramp of 10 ^oC/min. Whereas, TGA measurements for nanocomposites were performed under air flow (30 ml/min) with the heating rate of 20 ^oC/min using Mettler Toledo TGA/DSC 3+ system, to estimate the titania content. The TEM measurements for nanocomposites was performed following the same procedure used for the TEM measurement of SGH-TiO_2 (see section 3.1.2 for details).

Photoelectrochemical characterization: The photoelectrochemical characterization was performed on Ivium Bipotentiostat electrochemical workstation in a three-electrode system, applying Pt wire as a counter electrode and Ag/AgCl electrode as a reference electrode. Sodium sulphate (0.2 M) was used as an electrolyte solution. The ITO electrode covered with the photocatalyst used as a working electrode. The working electrode was prepared by the following method:[217] The photocatalyst (10 mg) was mixed with 300 µL of 2-propanol, 100 µL of Milli-Q water and 20 µL of Nafion solution then ultrasonically treated for 30 minutes to obtain a suspension. Afterwards, 20 µL of the suspension was drop-cast onto the ITO glass surface (0.77 cm^2) and then dried in air at room temperature to form the working electrode. The electrochemical impedance spectra (EIS) were measured over the frequency range of 0.01 to 1000 Hz with a 10 mV amplitude of the AC signal at 0 V vs. OCP (open circuit potential). The transient photocurrent responses were measured using chronoamperometry method at 0 V vs. OCP using green (515 nm) LED lamp as a light source.

3.2.5 Evaluation of the photocatalytic activity of titania/chitosan-lignin (T/CL) nanocomposite for the selective oxidation of benzyl alcohol (BnOH)

Photocatalytic selective oxidation of benzyl alcohol (BnOH): The photocatalytic selective oxidation of benzyl alcohol (BnOH) was performed in a glass photoreactor (20 mL). 20 mL of 0.5 mM (0.01 mmoles) BnOH solution in acetonitrile and 20 mg of photocatalyst (1g/L) were charged into the photoreactor. Then, the suspension was magnetically stirred at 400 rpm at room temperature for 1 hour in the dark to achieve the equilibrium. The photocatalytic reactions were performed under the irradiation of UV LED lamps (λ= 375 nm) and green LED lamps (λ= 515 nm). Each light source equipped with six LEDs and the intensity of the green and UV LEDs was measured to be 6 x ~9 W/m^2, recorded by a light meter (Delta OHM HD 2302.0) with a LP 471 RAD probe having a spectral range of 400-1050 nm and LP 471 UVA probe having a spectral range of 315-400 nm, respectively. The distance between the photoreactor wall and the light source was ~2 mm. At given illumination time intervals, aliquots (0.15 mL) were collected, and then filtered via nylon filter (0.2 μm pore size) to remove the photocatalyst. The set-up used for the photocatalytic oxidation of BnOH is shown in Figure 18.

After each catalytic run the photocatalyst was collected by decanting the solvent, washed multiple times with water, dried in hot air oven (110 ^{o}C) for 48 hours and reused for the next run with a fresh BnOH solution. Multiple photocatalytic runs were carried out following the same procedure.

Analysis of BnOH oxidation reaction: The quantitative analysis of substrate and reaction products was carried out on Waters 2487 high-performance liquid chromatography (HPLC) instrument equipped with Sunfire C18 (4.6 x 150 mm) column using an eluent consisting of Milli-Q (77.4%), acetonitrile (20%), methanol

(2.5%) and 0.05 M orthophosphoric acid (0.1%) at 1 mL/min flow rate. The temperature of the column oven was kept at 28 ºC. The BnOH conversion (Equation 12), and Bnald selectivity (Equation 13) were calculated as follows:

$$\%\ BnOH\ Conversion\ = \frac{M^{o}_{BnOH} - M_{BnOH}}{M^{o}_{BnOH}} \times 100 \qquad Equation\ 12$$

$$\%\ Bnald\ Selectivity\ = \frac{M_{Bnald}}{M^{o}_{BnOH} - M_{BnOH}} \times 100 \qquad Equation\ 13$$

Where M^{o}_{BnOH} corresponds to the initial amount of BnOH (mmoles), whereas M_{BnOH} and M_{Bnald} refers to the mmoles of BnOH and mmoles of Bnald after the photocatalytic reaction.

Apparent quantum yield (AQY) measurement: The apparent quantum yield (Φ) for the Bnald formation is the ratio of the amount of Bnald formed per unit time to the number of photons absorbed by the system per unit time (Equation 14)

$$\Phi = \frac{Number\ of\ moles\ of\ Bnald\ produced\ per\ unit\ time}{Number\ of\ photons\ (\text{or}\ Einstein)\ absorbed\ per\ unit\ time} \times 100 \quad (Equation\ 14)$$

To measure the apparent quantum yield (Φ), the photon flux to the photoreactor was determined by potassium ferrioxalate actinometry (see section 3.1.3, Apparent quantum yield (AQY) measurement). The experiment was performed using 0.006 and 0.15 M potassium ferrioxalate solution under UV and visible light, respectively.

3.2.6 Stability of titania/chitosan-lignin (T/CL) nanocomposite

The leaching of titanium from 75T/CL(25:75) nanocomposite (a representative photocatalyst) into BnOH solution after photocatalytic reaction (after 4 hours of irradiation) was determined via energy dispersive X-ray fluorescence analysis

(EDXRF). The EDXRF analysis was carried out using a MiniPal 4 equipment from PANalytical Co, with a Rh-tube and silicon drift detector (resolution 145 eV) to measure the elemental composition. The spectrum was collected in atmosphere, without using any filter, at a tube voltage of 30 kV in order to evaluate the presence of Ti dissolved in the solution. The time of acquisition was set to 600 seconds and the tube current up to 50 μA.

Moreover, the stability of 75T/CL(25:75) nanocomposite (a representative photocatalyst) in terms of the degradation of lignin and chitosan was assessed under dark conditions and light irradiation (UV and visible). For this purpose, 20 mg of the photocatalyst and 20 mL of acetonitrile were loaded in to a photoreactor and the suspension formed was stirred at 400 rpm in dark for 4 hours. Same experiments were carried out under UV and visible light to test the photostability of the 75T/CL(25:75) nanocomposite. After the experiments, 2 mL of the sample was collected, and then filtered via a nylon filter (pore size 0.2 μm) to remove the photocatalyst. Finally, UV-Visible absorption spectra were recorded (Thermo Scientific Evolution 220, UV-Vis Spectrophotometer) in the range of 200-800 nm, for the filtrate obtained.

4. RESULTS AND DISCUSSION

This chapter includes the work published in ChemSusChem and the work submitted for publication in RSC Advances.

4.1 In situ LMCT-sensitization of titania and its photocatalytic activity

4.1.1 Characterization of titania nanoparticles

The characteristic features of as-synthesized titania (SGH-TiO_2) were compared with commercial titania (P25) which is considered as a benchmark material in photocatalysis. The XRD reflexes (Figure 19) found in both P25 and SGH-TiO_2 at 25.4° {101}, 37.9° {004}, 48.0° {200}, 54.4° {105}, 63.2° {204}, 69.3° {116} and 75.7° {215} indexed to the anatase phase (JCPDS Card No. 21-1272) [218] of titania. However, the XRD reflex observed in SGH-TiO_2 at 30.8° {121} corresponds to the brookite phase (JCPDS no. 29-1360) [219] of titania.

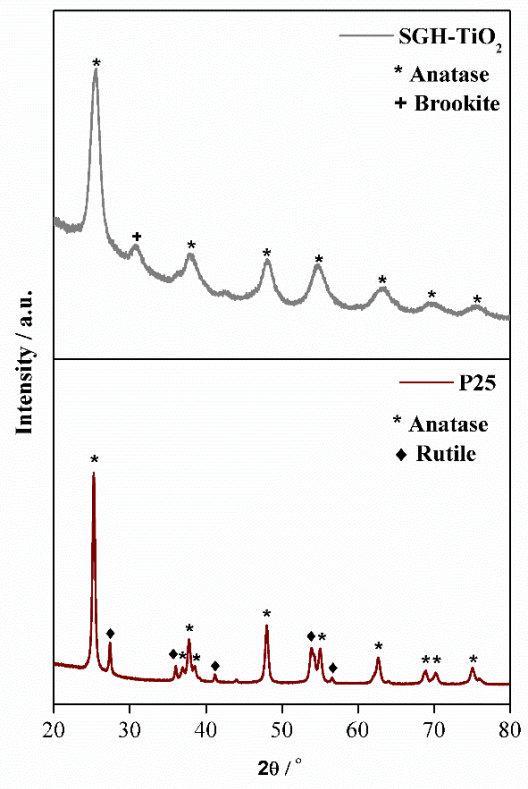

Figure 19. X-ray diffraction (XRD) pattern of P25 and SGH-TiO_2. (Reprinted an open-access article content[12])

Whereas, P25 exhibited (Figure 19) characteristic reflexes at 27.3° {110}, 36.1° {101}, 41.2° {111}, 53.9° {211} and 56.6° {220}, which are assigned to the rutile phase (JCPDS card no. 21-1276) [218] of titania. The phase composition and crystallite size of P25 and SGH-TiO_2 is summarized in Table 2.

Table 2. Textural (BET-specific surface area (SSA) BJH-pore volume (BJH Vp) and BJH-pore width (BJH wp)) and crystallographic features (phase composition and crystal size) of P25 and SGH-TiO_2 (Reprinted an open-access article content.[12])

Entries	Sample	Ratio of crystalline phases	Crystal size			SSA / [m^2g^{-1}]	BJH Vp / [cm^3g^{-1}]	BJH wp / nm
		Anatase:Brookite:Rutile / %	Anatase / nm	Brookite / nm	Rutile / nm			
1	SGH-TiO_2	74:26:0	5	6		177	0.20	3
2	P25	87:0:13	17		24	53	0.22	16

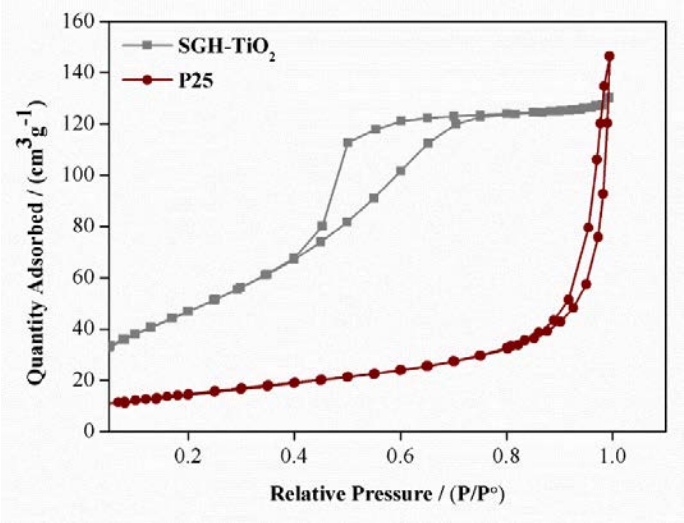

Figure 20. Nitrogen adsorption-desorption isotherms of P25 and SGH-TiO_2 (Adapted from an open-access article[12])

The textural properties of P25 and SGH-TiO_2 were examined by N_2 adsorption-desorption isotherms. As shown in Figure 20, that SGH-TiO_2 displayed type IV

isotherm and H2 hysteresis that is indicative of mesoporous materials. However, P25 revealed type II isotherm and H3 hysteresis that is typical of plate-like particles or slit-shaped pores.[220] It was found that SGH-TiO_2 exhibited higher specific surface area (177 m^2g^{-1}) compared to P25 (53 m^2g^{-1}), which could be beneficial from photocatalytic point of view. The detailed microstructure properties of P25 and SGH-TiO_2, such as pore volume, pore width etc. are summarized in Table 2. According to TGA weight loss, the hydroxyl group density (OH/nm^2) of P25 and SGH-TiO_2 is estimated to be 7 OH/nm^2 and 9 OH/nm^2, respectively. The results attained are comparable with the reported OH group density of P25 in literature (8 OH/nm^2 [221], 5.3 OH/nm^2 [222]), and sol-gel synthesized titania (11.9 OH/nm^2 [223] 8.7 OH/nm^2 [212] and 10.2 OH/nm^2 [224]).

4.1.2 Photocatalytic activity of in situ LMCT-sensitized titania for the selective oxidation of HMF

It was hypothesized that the adsorption of HMF on SGH-TiO_2 results in the formation of LMCT-complex which impart the visible light activity to titania for the selective oxidation of HMF. To investigate the formation and reactivity of LMCT-complex of HMF on titania, the photocatalytic experiment for the selective oxidation of HMF was carried out under visible light (λ = 515 nm). Interestingly, in situ LMCT-sensitization of SGH-TiO_2 by HMF displayed a high activity for the oxidation of HMF (Figure 21a). After 4 hours (240 minutes) of illumination under visible light (λ = 515 nm), 59% HMF conversion was achieved with high (87%) DFF selectivity. The DFF selectivity increases steadily (Figure 21a) in the beginning, which may attribute to the slow desorption of DFF from the surface of SGH-TiO_2. Additionally, the selectivity of DFF remains stable over the course of reaction under visible light (Figure 21a), which indicates that relatively low energy visible light radiation prevents the over-oxidation of DFF. However, commercial titania (P25) exhibited very low activity (Figure 21b)

with 18% HMF conversion and moderate DFF selectivity (69%) after 4 hours (240 minutes) of irradiation. The low activity of P25 compared to SGH-TiO_2 under visible light might be related to the low specific surface area of P25 (53 m^2g^{-1}) than SGH-TiO_2 (177 m^2g^{-1}). Furthermore, SGH-TiO_2 and P25 exhibited high activity for the oxidation of HMF (Figure 22a and 22b) under UV light (λ = 375 nm). However, the DFF selectivity exhibited by SGH-TiO_2 (36%) and P25 (44%) was very low (Figure 22a and 22b) at 52% and 54% HMF conversion, respectively.

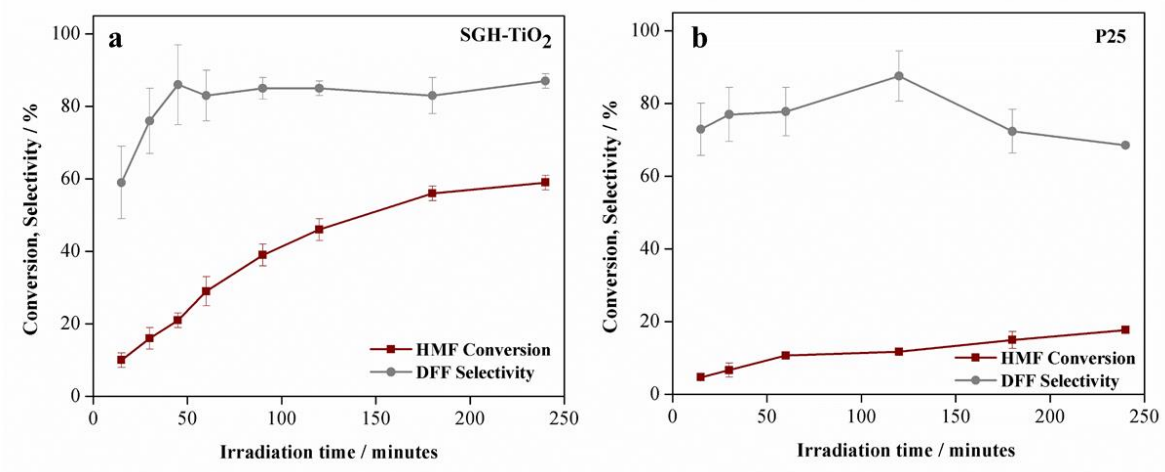

Figure 21. HMF conversion and DFF selectivity profile in the photocatalytic oxidation of HMF to DFF under visible light (λ = 515 nm) over a) SGH-TiO_2 b) P25 (Adapted from an open-access article[12])

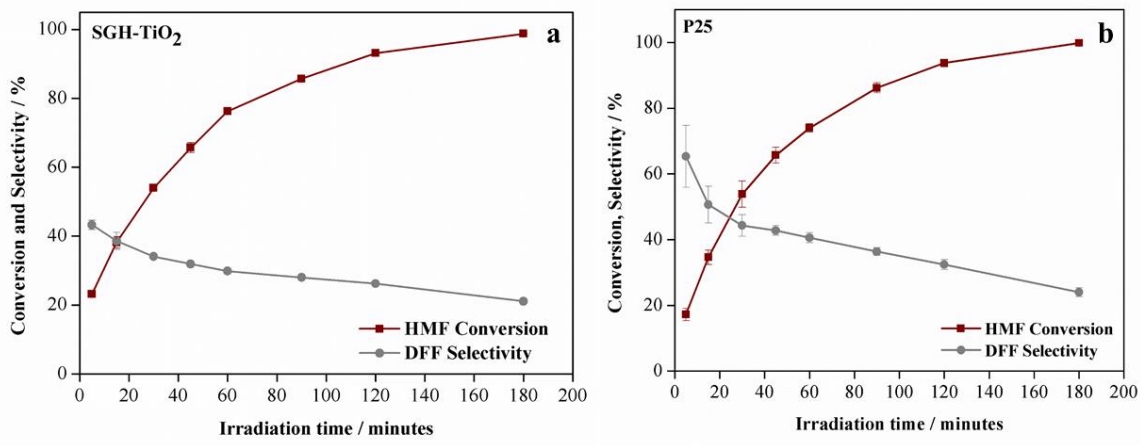

Figure 22. HMF conversion and DFF selectivity profile in the photocatalytic oxidation of HMF to DFF under UV light (λ = 375 nm) over a) SGH-TiO_2 b) P25 (Adapted from an open-access article[12])

The low selectivity of DFF, under UV light suggests that the DFF produced may compete with HMF and underwent further oxidation until complete mineralization. Besides that, HMF may undergo complete oxidation to CO_2 and H_2O via different intermediates, which may not desorb from the surface of the photocatalyst to liquid medium.[203] This is in consistent with the study performed by Yurdakal et al.[203] who evaluated various crystalline phases of titania to selectively oxidize HMF to DFF in aqueous medium under UV light.

4.1.3 Recyclability and stability of SGH-TiO_2

The recyclability and stability of the catalyst has crucial importance for the industrial application view point. To evaluate the recyclability of the photocatalyst, the reusability experiment was performed for the selective oxidation of HMF using SGH-TiO_2. As presented in Figure 23, SGH-TiO_2 could be employed in multiple cycle without significant drop in the DFF selectivity and HMF conversion.

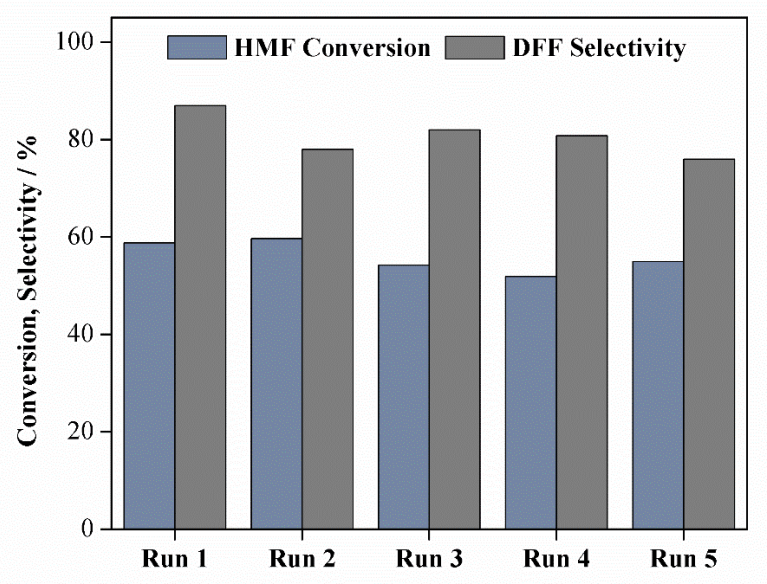

Figure 23. Recycling runs for the selective oxidation of HMF over SGH-TiO_2 under visible light irradiation. (Adapted from an open-access article[12])

Moreover, the XRF analysis (Figure 24) of HMF solution after photocatalytic reaction under visible light (after 4 hours of irradiation), did not show the titanium leaching from SGH-TiO_2, which indicates the stability of SGH-TiO_2. The peaks appeared in XRF spectrum refers to Rh from Rh lamp and, Cu signals that are finger print of the spectrometer.

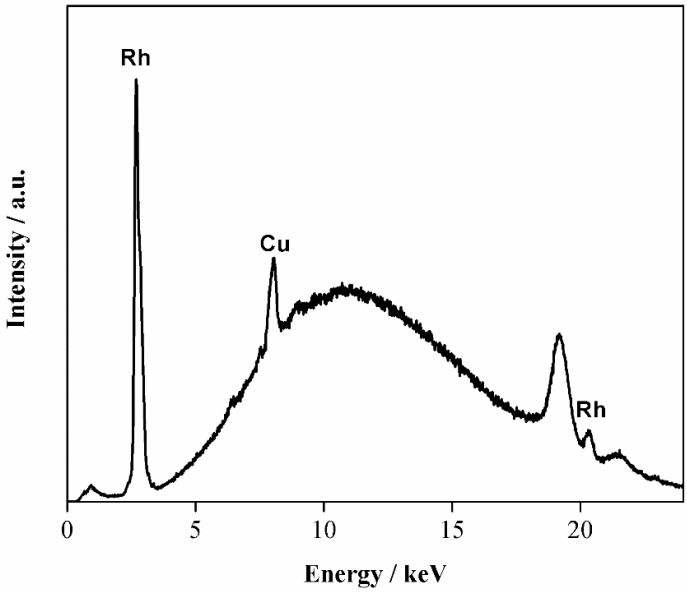

Figure 24. XRF analysis of HMF solution catalyzed over SGH-TiO_2 under visible light.

4.1.4 Apparent quantum yield (AQY)

The photon flux absorbed under visible light by the photocatalytic system was estimated to be 11.63×10^{-9} Es^{-1}. Whereas, the AQY demonstrated by P25 and SGH-TiO_2 for the production of DFF after 4 hours of irradiation were estimted to be 2.2% and 6.3% at a wavelength of 515 nm, respectively.

4.1.5 Formation of ligand-to-metal charge transfer (LMCT)-complex on SGH-TiO_2

In order to verify that the activity of SGH-TiO_2 under visible light is ascribed to in situ LMCT-sensitization, a series of characterization was performed for pristine titania and

in situ sensitized titania (HMF-adsorbed titania). To evaluate the effect of adsorption of HMF on the optical absorption behavior of SGH-TiO_2 and P25, DRS-UV-Visible absorption spectra (Figure 25) was recorded for P25, SGH-TiO_2, HMF-adsorbed P25 (HMF-Ads-P25) and HMF-adsorbed SGH-TiO_2 (HMF-Ads-SGH-TiO_2). As shown in Figure 25, the adsorption of HMF on P25 expanded the absorption in the visible light region, which is also accompanied by the slight change in color of P25. However, the adsorption of HMF on SGH-TiO_2 results in a pronounced increase in the absorption of visible light (up to 650 nm), which is also complemented by a noteworthy change in color (from white to yellow) of SGH-TiO_2 (Figure 25). Nevertheless, HMF does not show absorption in the visible light region like titania. It is therefore suggested that the absorption of visible light is related to the LMCT-complex formation between HMF and titania. In order to confirm that the selective oxidation of HMF under visible light was not a result of direct photosensitization of the HMF, a control experiment was carried out in the absence of SGH-TiO_2, no activity in terms of HMF conversion was observed (Entry 16, Table 3).

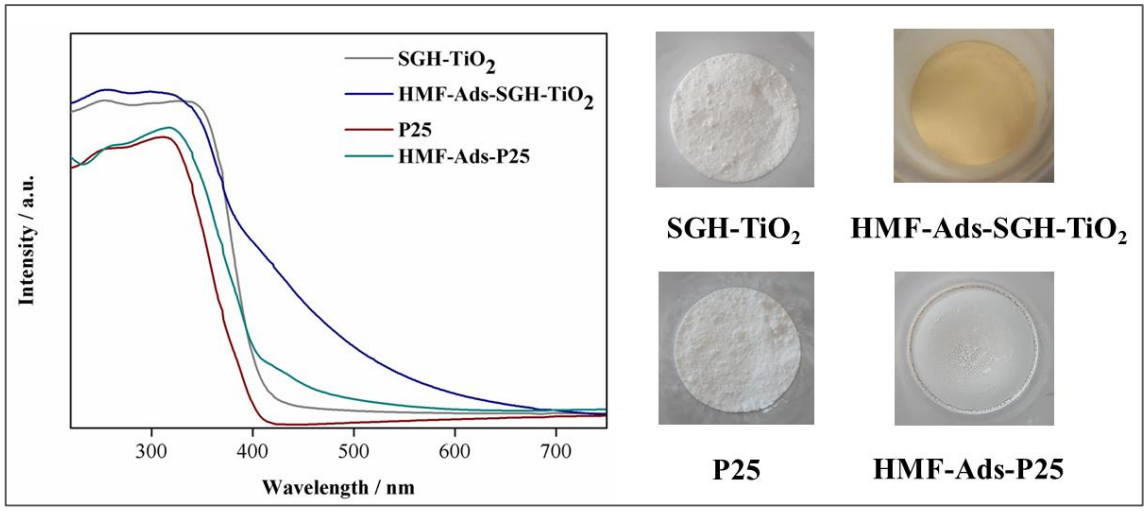

Figure 25. DRS-UV-visible absorption spectra of P25, SGH-TiO_2, HMF-Ads-P25 and HMF-Ads-SGH-TiO_2. (Reprinted an open-access article content[12])

To further evaluate the phenomenon of LMCT-complex formation between titania and HMF, FTIR analysis was carried out for SGH-TiO_2, HMF and HMF-Ads-SGH-TiO_2 samples. The characteristic bands observed in FTIR spectrum of HMF-Ads-SGH-TiO_2 in comparison with individual components can be observed in Figure 26. The band observed at 1662 cm^{-1}, 1537 cm^{-1} and 1420 cm^{-1} in HMF-Ads-SGH-TiO_2 are typical IR bands for HMF, which refers to C=O stretching vibration, C=C symmetric stretching and asymmetric stretching, respectively.[225] These bands indicate the adsorption of HMF on SGH-TiO_2 surface. However, a weak band appeared at 1198 cm^{-1} in the HMF-Ads-SGH-TiO_2 assigned to the multiple rocking vibrations of C-C-C bond.[194] Interestingly, the band corresponding to the O-H stretching vibrations in SGH-TiO_2 (hydroxyl groups present in the form of hydrogen bonded water or free or metal (Ti) hydroxyl moiety) and HMF at 3200-3400 cm^{-1} was found to be absent in the HMF-Ads-SGH-TiO_2. The absence of an obvious O-H stretching band in the HMF-Ads-SGH-TiO_2 suggested that, the adsorption of HMF over SGH-TiO_2 may have occurred via OH group on the metal surface and result in the formation of a metal alkoxide complex.

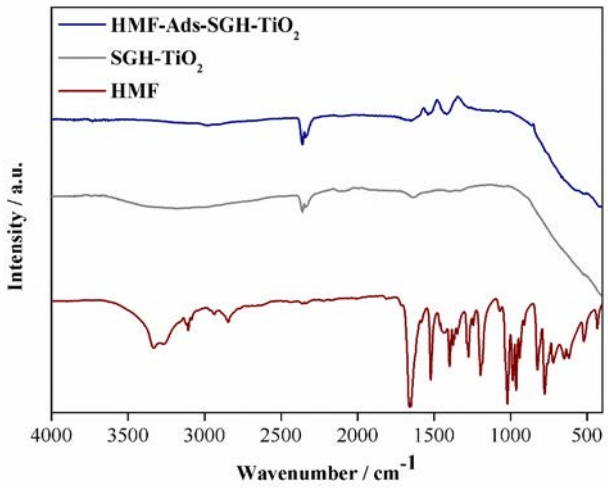

Figure 26. FTIR spectra of HMF, SGH-TiO_2 and HMF-Ads-SGH-TiO_2 (Reprinted an open-access article content[12])

Furthermore, the distinctive band of titania due to the Ti-O-C and Ti-O-Ti stretching vibration in the range of 800-400 cm^{-1} was also found in HMF-Ads-SGH-TiO_2. However, the bands observed in SGH-TiO_2 and HMF-Ads-SGH-TiO_2 at 2357 cm^{-1}, 2115 cm^{-1}, may have attributed to physically adsorbed CO, CO_2, respectively.

To further corroborate the LMCT-complex formation via interaction of HMF and SGH-TiO_2, Raman spectra for SGH-TiO_2, HMF and HMF-Ads-SGH-TiO_2 has also been recorded (Figure 27). It can be seen (Figure 27b), that HMF-Ads-SGH-TiO_2 exhibited distinctive furan ring C=C symmetric vibrations at 1521 cm^{-1} [226], which suggests the HMF adsorption on the surface of SGH-TiO_2. In addition, the broad band observed at 3200-3400 cm^{-1} (Figure 27c) for O-H stretching vibrations in HMF and SGH-TiO_2 totally disappeared in HMF-Ads-SGH-TiO_2, suggesting the formation of LMCT complex possibly through a dissociative adsorption of CH_2OH moiety of HMF and hydroxyl group of SGH-TiO_2. Besides that, a weak band observed at 2941 cm^{-1} in HMF-Ads-SGH-TiO_2 corresponds to C-H stretching vibrations.[227]

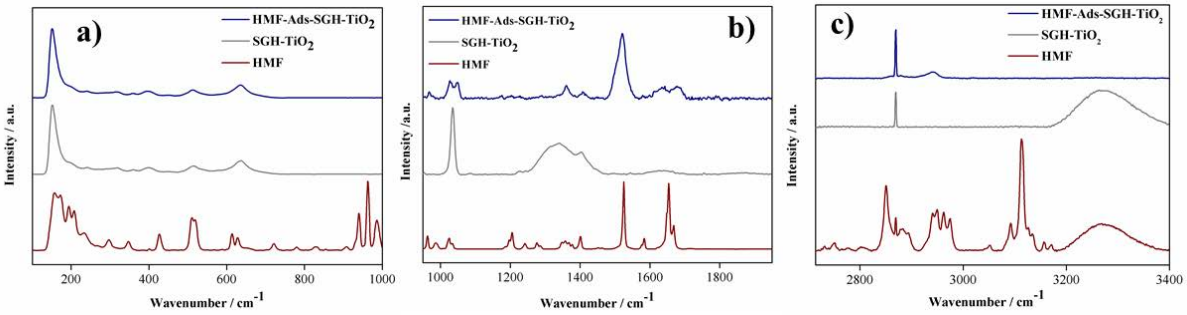

Figure 27. Raman spectra of HMF, SGH-TiO_2 and HMF-Ads-SGH-TiO_2 (Reprinted an open-access article content[12])

On the other hand, a broad doublet observed at 1637 cm^{-1} and 1680 cm^{-1} may refers to the stretching vibrations of C=O due to HMF adsorption. Additionally, HMF-Ads-SGH-TiO_2 exhibited a new weak band at 1048 cm^{-1} that may ascribe to the stretching

vibrations of C-O group of the alcoholate species formed between HMF and SGH-TiO_2. These results suggested that the adsorption of HMF on SGH-TiO_2 may form a LMCT-complex, which impart visible light activity to HMF-Ads-SGH-TiO_2. Furthermore, Raman spectra of HMF-Ads-SGH-TiO_2 also corroborated the existence of three distinctive Raman active modes of anatase phase (Figure 27a) of titania at 399 cm^{-1}, 513 cm^{-1} and 635 cm^{-1}, which are indexed to unresolved doublet (B_{1g}, A_{1g}/B_{1g}) and E_g symmetries, respectively.[228] While, the strong band appeared at 152 cm^{-1} refers to A_{1g} mode of brookite.[229]

XPS measurements were performed to evaluate the changes in the surface chemical environment of SGH-TiO_2 due to interaction with HMF. As shown in Figure 28a, the Ti 2p peaks of SGH-TiO_2 deconvoluted into four peaks, the peak observed at 458.5 eV (Ti $2p_{3/2}$) and 464.3 eV (Ti $2p_{1/2}$) corresponds for Ti^{4+} in TiO_2 lattice.[194] While, the peak found at 457.0 eV (Ti $2p_{3/2}$) and 462.8 eV (Ti $2p_{1/2}$) assigned to Ti^{3+} in Ti_2O_3.[230] Whereas, the HMF-Ads-SGH-TiO_2 XPS spectrum of Ti 2p has not shown a pronounced shift in the binding energies and substantial differences in the peak area (Figure 28b). This indicates that HMF adsorption did not greatly influenced the electronic state of Ti element. Furthermore, negligible changes (~1%) in the peak area contribution of Ti^{4+} and Ti^{3+} was observed after the adsorption of HMF, which is an indication of stable titania lattice. This suggests that interaction of HMF with titania may possibly occur via a terminal OH groups instead of Ti substitution. The O1s spectrum of SGH-TiO_2 split into four peaks (Figure 28c), the peak observed at 529.7 eV may ascribe to lattice oxygen. While, the peaks appeared at 530.5 eV and 531.3 eV refers to oxygen in Ti_2O_3 and oxygen linked with carbon (C=O), respectively. Whereas the peak observed at 532.8 eV assigned to hydroxyl groups attached to carbon or titanium (C-OH or Ti-OH). Whereas, the O1s spectrum of HMF-Ads-SGH-TiO_2 corresponding to the surface

bound oxygen in the form hydroxyl group, showed a slight shift (Figure 28d) in the binding energy (532.5 eV). This may have attributed to slightly higher electron density[194] around hydroxyl group associated oxygen, after HMF adsorption. Though, a negligible change in the peak area contribution of O 1s associated to surface bound and lattice oxygen was observed after the adsorption of HMF (Figure 28d).

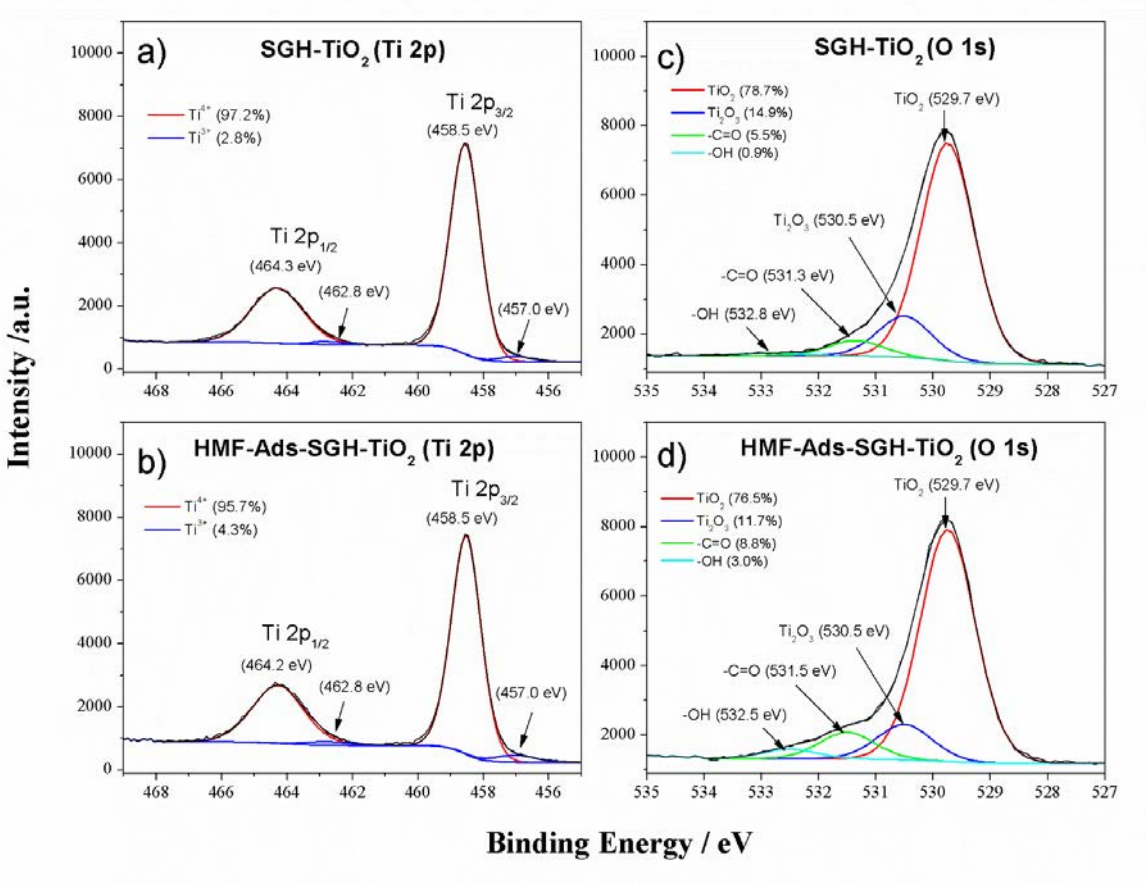

Figure 28. XPS spectra of a) Ti 2p SGH-TiO_2 b) Ti 2p HMF-Ads-SGH-TiO_2 c) O1s SGH-TiO_2 d) Ti 2p HMF-Ads-SGH-TiO_2. (Reprinted an open-access article content[12])

4.1.5.1 Role of surface OH groups for LMCT-sensitization of SGH-TiO_2

To further evaluate the role of surface OH groups in LMCT-complex formation, SGH-TiO_2 was calcined at high temperature (600 °C) with the goal to eliminate surface OH

groups through condensation. FTIR (Figure 29) and Raman (Figure 30) spectra of calcined SGH-TiO_2 (SGH-TiO_2-cal-600) exhibited that the band for O-H stretching vibration at 3200-3400 cm^{-1}, and bending vibrations at 1333 cm^{-1} vanished upon calcination. Interestingly, the SGH-TiO_2-cal-600 was found to be inactive as a photocatalyst for HMF oxidation under visible light (Entry 5, Table 3), suggesting that the OH groups are crucial for the visible light photocatalytic activity. They are possibly involved in the LMCT-complex formation and visible light activity.

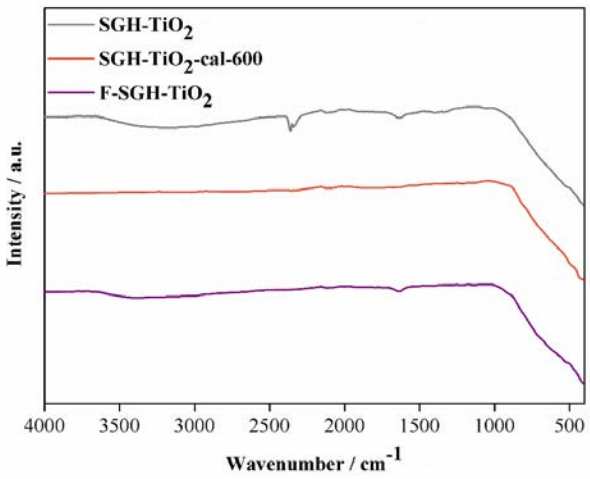

Figure 29. FTIR spectra of SGH-TiO_2, SGH-TiO_2-cal-600 and F-SGH-TiO_2. (Reprinted an open-access article content[12])

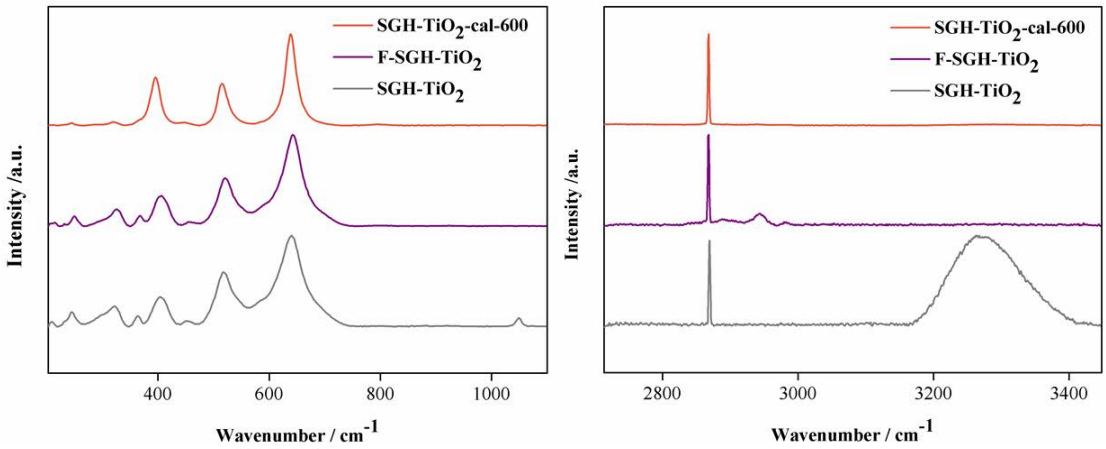

Figure 30. Raman spectra of SGH-TiO_2, F-SGH-TiO_2 and SGH-TiO_2-cal-600. (Reprinted an open-access article content[12])

In a further approach to corroborate the contribution of surface OH groups for LMCT-sensitization, SGH-TiO_2 has been modified chemically through surface-fluorination to exchange the surface OH groups with fluoride (F^-) ions.[209] The F^- ion surface coverage is estimated to be 7 OH/nm^2, which accord for ~80 % of surface exchange of F^- ion with the OH groups. The XPS measurement (Figure 31) for surface-fluorinated SGH-TiO_2 (F-SGH-TiO_2) also evidenced the presence of F^- ions on the titania surface, and the surface hydroxyl groups of titania were modified to Ti-F (Figure 31). Besides that, the absence of an evident O-H stretching band 3200-3400 cm^{-1} in the FTIR (Figure 29) and Raman (Figure 30) spectra of F-SGH-TiO_2 further confirm the replacement of terminal hydroxyl group with F^- ion. Expectedly, the surface-fluorination totally hindered the photocatalytic activity of SGH-TiO_2 under visible light (Entry 6, Table 3). This is again accordant with inhibiting the HMF adsorption on the titania surface and, therefore, the LMCT-complex formation via OH group interaction.

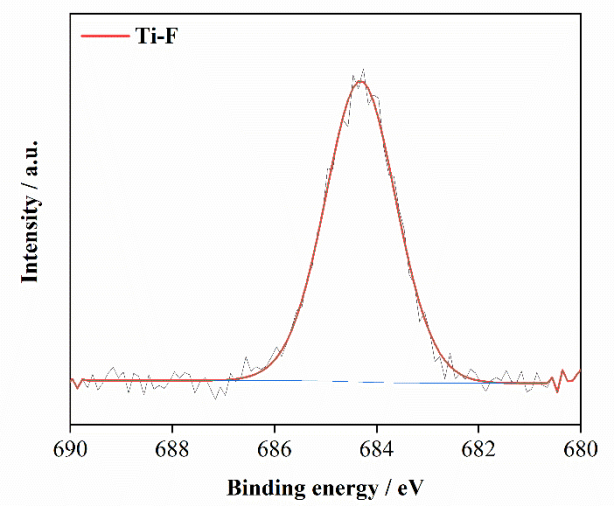

Figure 31. XPS spectra of F 1s of surface-fluorinated SGH-TiO_2 (F-SGH-TiO_2).

4.1.6 Plausible mechanism of oxidation of HMF via LMCT-sensitized SGH-TiO_2

To elucidate the dominant active species involved in the selective oxidation of HMF under visible light, various additives/radical scavengers such as 1,4-benzoquinone

(BQ), methanol, and silver cations were separately introduced in to the reaction medium. The methanol was added as hole (h^+) scavenger, did not affect the conversion of HMF (56%) and selectivity for DFF (88%) greatly, suggesting that h^+ may not be the main active species involved in the oxidation of HMF (Entry 8, Table 3). However, the addition of BQ in the reaction medium as a superoxide radical anion ($O_2^{-\bullet}$) scavenger completely inhibited the HMF conversion and DFF production (Entry 9, Table 3). This indicates that the $O_2^{-\bullet}$ is the dominant active species involved in the selective oxidation of HMF to DFF. Whereas, introducing silver cations as electron acceptors completely hindered the photocatalytic activity of SGH-TiO_2 (Entry 10, Table 3). This represents the potential involvement of electrons in the active intermediates formation for the oxidation of HMF. It is proposed that silver cations as electron acceptor may hamper the generation of $O_2^{-\bullet}$, potentially responsible for HMF oxidation. Additionally, to examine the effect of oxygen on the activity of SGH-TiO_2, the oxidation of HMF was performed under anoxic (degassed acetonitrile and under Ar flow, 25 mL/min) conditions as well as by bubbling air into the reaction medium. The anoxic environment significantly affects the photocatalytic activity and inhibit the HMF conversion (Entry 11, Table 3). However, bubbling air (25 mL/min) into the reaction medium enhanced the selectivity of DFF up to 96% (Entry 12, Table 3), nonetheless the conversion of HMF was slightly decreased (52%), which suggests that increased oxygen content inhibit the side reactions probably through neutralizing the reactive oxidizing species possibly formed by the potential side product (H_2O_2). Furthermore, bubbling air in to the reaction medium may also facilitate the desorption of DFF from the surface of catalyst, which further enhanced the selectivity for DFF.

Table 3. The results of the photocatalytic selective oxidation of HMF under variable conditions. (Adapted from an open-access article[12])

Entries	photocatalyst	Light	Additive	HMF Conv. / %	DFF Sel. / %	Carbon Balance /%
1	SGH-TiO_2	Visible	None	59	87	92
2	SGH-TiO_2	[a]UV	None	52	36	66
3	P25	Visible	None	18	69	94
4	P25	[a]UV	None	54	44	70
5	SGH-TiO_2-cal-600	Visible	None	0.0	0.0	100
6	F-SGH-TiO_2	Visible	None	0.0	0.0	100
7	P90	Visible	None	35	75	91
8	SGH-TiO_2	Visible	Methanol	56	88	93
9	SGH-TiO_2	Visible	1,4-benzoquinone	0.0	0.0	100
10	SGH-TiO_2	Visible	Ag^+	0.0	0.0	100
11	SGH-TiO_2	Visible	[b]Ar	0.0	0.0	100
12	SGH-TiO_2	Visible	Air	52	96	98
13	SGH-TiO_2	Visible	Ar:Air	38	87	97
14	SGH-TiO_2	Dark	None	0.0	0.0	100
15	[c]SGH-TiO_2	Visible	None	0.0	0.0	100
16	None	Visible	None	0.0	0.0	100
17	Anatase	Visible	None	0.0	0.0	100
18	Brookite	Visible	None	0.0	0.0	100
19	Ana:Brook (74:26)	Visible	None	0.0	0.0	100

(**Reaction conditions:** HMF (0.02 mmol, 1 mM), photocatalyst, (20 mg, 1g/l), scavenger (1:1 molar ratio of substrate, 0.02 mmol), reaction time (240 minutes), [a]reaction time (30 minutes), solvent (acetonitrile), [b]solvent (degassed acetonitrile), [c]solvent (water), HMF solution volume (20 mL), air flow rate (25 mL/min, 21 % O_2), Ar flow rate (25 mL/min, 99.9 % Ar), Ar:Air flow rate (15 mL/min:10 mL/min, 60% Ar and 8.4% O_2), LED wavelength (UV = 375 nm, Visible = 515 nm), light intensity was 6 x ~9 W/m^2, Ana:Brook (Physical mixture of anatase and brookite))

To get further insight on the selective oxidation of HMF, some additional experiments were performed and results are summarized in Table 3. Commercial titania (P90) exhibited higher activity (Entry 7, Table 3) for the selective oxidation of HMF under visible light compared to P25 (Entry 3, Table 3). This might be related to higher specific surface area of P90 (100 m^2g^{-1}) than P25 (53 m^2g^{-1}). Similarly, SGH-TiO_2 displayed superior photocatalytic activity for the selective oxidation of HMF as compared to P25 under visible light (Entry 1 and 3, Table 3). There are couple of advantageous features exhibited by SGH-TiO_2, that may enhance its photocatalytic activity. For instance, HMF-ads-SGH-TiO_2 displayed marked shift in the light absorption from 400 to 650 nm in comparison with HMF-ads-P25 (Figure 25). This may attribute to higher (177 m^2g^{-1}) specific surface area of SGH-TiO_2 than P25 (53 m^2g^{-1}). The higher specific surface area of SGH-TiO_2 contribute 4 times higher number of potential adsorption sites (OH groups) for HMF than P25, which in turn improved the activity of SGH-TiO_2 for the selective HMF oxidation under visible light. On the basis of characterization results and the photocatalytic experiments performed in the presence of various additives and scavengers, a possible reaction mechanism is proposed for the selective oxidation of HMF over SGH-TiO_2 under visible light (Figure 32). The HMF adsorption on SGH-TiO_2 initiate all the oxidation steps. LMCT-complex formed by the HMF adsorption is activated upon visible light irradiation, that transfer electrons into the CB of SGH-TiO_2, and HMF is converted to the corresponding radical cation (Step 2, Figure 32). While, the oxygen dissolved in the reaction medium accepts electron from the CB of SGH-TiO_2 and transformed to superoxide radical anion ($O_2^{-\bullet}$). Subsequently, the radical cation reacts with $O_2^{-\bullet}$ and produces an intermediate radical and hydroperoxyl ($^{\bullet}OOH$) radical (Step 3, Figure 32). In the last step, the $^{\bullet}OOH$ abstract hydrogen atom from the intermediate radical to furnish the desired (DFF) product and side (H_2O_2) product (Step 4, Figure 32).

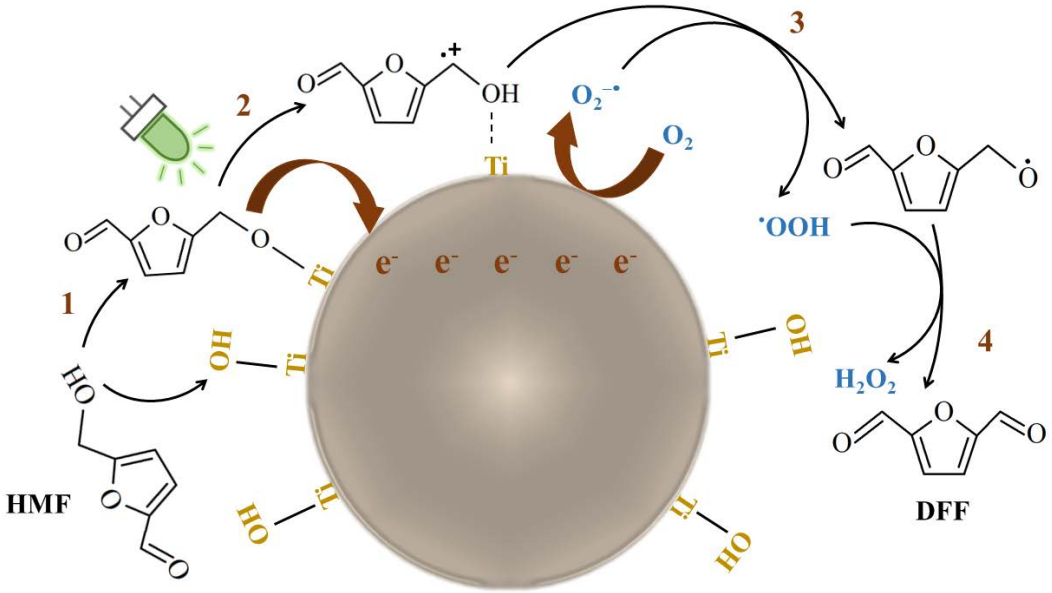

Figure 32. Plausible mechanism for the oxidation of HMF over SGH-TiO_2 under visible light (λ = 515 nm). (Adapted from an open-access article[12])

The H_2O_2 formed may have adsorbed on the SGH-TiO_2 and probably react with the electrons to form $^{\bullet}OH$, that could affect the reaction mechanism and DFF selectivity. The radical cation produced in the step 2, may or may not move into the liquid reaction medium. However, our experiments could not explain whether the radical cation stays on the surface or released. If the radical cation stays over the surface of SGH-TiO_2, it could react with another HMF molecule and generate an intermediate radical by deprotonation. Successively, the $O_2^{-\bullet}$ may react with the intermediate radical and generate DFF and hydroperoxide ($^{-}$OOH) anion. While, the $^{-}$OOH could react with the proton and produce H_2O_2. Though, the probability of free radical cation attacked by the $O_2^{-\bullet}$ in the beginning is greater in comparison with the intermediate radical attacked at later stages.

4.1.7 Active sites and HMF conversion per surface OH group

In catalysis, the expression active site is commonly used for the adsorption site operative for catalytic reactions. In photocatalysis, the active site is generally employed for the dispersed chemical entities for example metal complexes/adsorbed chemical species, on the support.[231] Nevertheless, the photocatalytic reaction can only occur upon light absorption by these species, and the species that are not irradiated cannot act as an active site.[231–233] Thus, the expression active site is often ambiguous in photocatalysis, and its relationship with photocatalytic activity is difficult to assess.[231] However, the estimation of photocatalytic activity based on the active sites number cannot be entirely ruled out. Here, the surface OH groups of titania are considered as potential active sites. Accordingly, the photocatalytic activity has also been investigated based on the number of HMF molecules converted after 1 hour of irradiation and the number of OH groups originally present. The HMF conversion with regard to surface hydroxyl groups and area related parameters are presented in Table 4. The number of surface hydroxyl groups exhibited by SGH-TiO_2 was four times higher as compared to P25 (Table 4), which might be related to higher specific surface area (177 m^2 g^{-1}) and slightly higher OH group density (9 OH/nm^2) of SGH-TiO_2. Though, the HMF conversion per surface hydroxyl groups per unit time (area- normalized rate) exhibited by P25 was 1.5 times higher as compared to SGH-TiO_2 (Table 4). Moreover, P25 displayed two times higher HMF conversion per surface hydroxyl groups as compared to SGH TiO_2 (Table 4). Nonetheless, various factors may affect the HMF conversion per surface hydroxyl groups. The comparatively lower HMF conversion per surface hydroxyl groups by SGH TiO_2 suggest that all the hydroxyl groups may not necessarily be accessible for HMF adsorption to initiate the catalytic cycle. Furthermore, the entire surface area is not accessed by light, specifically the aggregated particles and inside the pores.[234]

Table 4. Area-normalized conversion (conv.), area-normalized rate, conv. per surface hydroxyl groups and conv. per surface hydroxyl groups per unit time accomplished by P25 and SGH-TiO_2. (Reprinted an open-access article content[12])

Entries	Catalyst	Area-normalized Conv. / m^{-2}	Area-normalized rate / m^{-2} s^{-1}	D_{OH} / OH nm^{-2}	Number of OH groups	Conv. per OH	Conv. per OH per unit time/ s^{-1}
1	SGH-TiO_2	8.1×10^{17}	22.7×10^{13}	9	32.5×10^{18}	0.08	24.7×10^{-6}
2	P25	12.5×10^{17}	34.9×10^{13}	7	7.8×10^{18}	0.17	47.2×10^{-6}

(**Reaction conditions:** HMF (0.02 mmol, 1 mM), photocatalyst (20 mg, 1g/l), solvent (acetonitrile), volume of HMF solution (20 mL), irradiation time (1 hour), incident light wavelength (515 nm) and the light intensity (6 x ~9 W/m^2))

4.1.8 Conclusions

In conclusion, the adsorption of biomass-derived platform chemical (HMF) on the titania surface form a LMCT-complex, which played a role of in situ sensitizer and enabled the selective oxidation of HMF to the industrially important chemical diformylfuran (DFF) under visible light (λ = 515 nm). Based on the FTIR and Raman characterization, it is concluded that the dissociative interaction of OH groups of HMF and the titania surface is crucial for the visible light active LMCT-complex formation. Moreover, the modification (surface-fluorination) and removal (calcination) of hydroxyl groups of titania also inhibited the HMF oxidation, demonstrating that hydroxyl groups are crucial for LMCT-complex formation and visible light activity. DRS-UV Visible results showed that the LMCT-complex formation with HMF extended the visible light absorption of titania up to 650 nm. Upon visible light irradiation, the LMCT-complex transport electrons in to the CB of titania. The electrons subsequently interact with the oxygen dissolved in the reaction medium and form superoxide radical anion, dominantly involved in the oxidation of HMF. The visible

light activity of LMCT-complex influenced by the available surface area, SGH-TiO_2 showed higher activity for HMF conversion (59%) compared to P25 (18%) and P90 (35%). This might be related to the higher specific surface area of SGH-TiO_2 (177 m^2g^{-1}) than P25 (53 m^2g^{-1}) and P90 (100 m^2g^{-1}), which provide higher overall number of potential adsorption sites (OH groups) for HMF and ultimately improved the activity of SGH-TiO_2.

4.2 Titania/chitosan-lignin (T/CL) nanocomposite and its photocatalytic activity for the selective oxidation of benzyl alcohol (BnOH)

4.2.1 Characterization of chitosan-lignin (CL) composite

The as-synthesized chitosan-lignin (CL) composite were characterized through various analytical techniques and the distinguishing features of the CL composites were compared with Norit (commercial activated carbon). The surface morphology of chitosan, lignin, CL composites and Norit was investigated by means of the scanning electron microscopy (SEM) technique. SEM images of the chitosan exhibited rough and flaky surface (Figure 33a). Whereas, lignin showed rounded or semispherical shape particles with voids on flat the surface (Figure 33b).

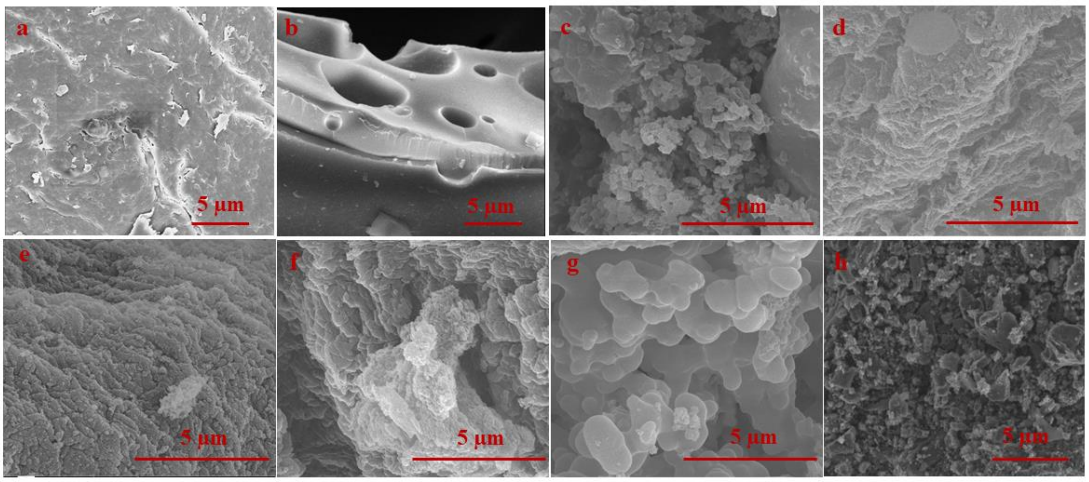

Figure 33. Scanning electron microscope (SEM) images of a) Chitosan, b) Lignin, c) CL(10:90), d) CL(25:75), e) CL(50:50), f) CL(75:25), g) CL (90:10), h) Norit

However, CL composite showed different morphology compared to parent materials. The CL composites lack ordered structure and displayed coarse and non-uniform surface. Moreover, the relative proportion of chitosan and lignin did not significantly change the composite morphology. Whereas, Norit showed porous irregular surface structure (Figure 33h).

The chemical composition of chitosan, lignin, CL composites and Norit was evaluated via elemental analysis (Table 5). Chitosan (Entry 1, Table 5) exhibited high nitrogen content (6.2 wt%) attributed to the presence of nitrogen-containing functional moieties (acetamide and amine). However, nitrogen has not been detected in Norit and lignin. As expected, the increase in chitosan proportion in the CL composite increased the nitrogen content in the CL composites (Entry 3-7, Table 5).

Table 5. Elemental composition (CHNS wt%) of chitosan, lignin, Norit and CL composites.

Entries	Samples	C / %	H / %	S / %	N / %
1	Chitosan	40.71	6.64	ND	6.26
2	Lignin	48.26	4.73	4.16	ND
3	CL(10:90)	62.47	4.98	2.06	0.06
4	CL(25:75)	60.59	4.83	1.62	0.29
5	CL(50:50)	62.84	4.75	1.25	0.55
6	CL(75:25)	64.77	4.7	0.89	0.76
7	CL(90:10)	64.93	4.65	0.44	1.28
8	Norit	84.41	0.43	0.03	ND
9	75T/CL(10:90)	15.45	1.67	0.52	ND
10	75T/CL(25:75)	15.00	1.59	0.35	ND
11	75T/CL(50:50)	13.79	1.44	0.25	ND
12	75T/CL(75:25)	15.82	1.52	0.24	ND
13	75T/CL(90:10)	15.87	1.44	0.07	ND
14	75T/Norit	20.18	0.56	ND	ND

ND: Not detected

Furthermore, ~4 wt% sulphur was found in lignin owing to the presence of sulfonate group. The decrease in lignin proportion in the CL composites decreased the sulphur content in the CL composites (Entry 3-7, Table 5). Additionally, traces of sulphur were also detected in Norit (Entry 8, Table 5).

In order to evaluate the textural properties of CL composites and Norit the N_2 adsorption-desorption isotherms were recorded. All the CL composites exhibited Type II isotherms (Figure 34), which is a characteristic of non-porous materials. The specific surface area of CL composites according to Brunauer-Emmett-Teller (BET) analyses were calculated to be in the range of 10-16 m^2g^{-1} (Entries 1-5, Table 6). Whereas, Norit exhibited different textural properties compared to CL composites. The shape of N_2 adsorption-desorption isotherms observed for Norit corresponds for Type IV isotherm with H3 hysteresis (Figure 34), which is indicative of mesoporous material with slit-shaped pores. Moreover, Norit showed much higher specific surface area (558 m^2g^{-1}) compared to CL composites.

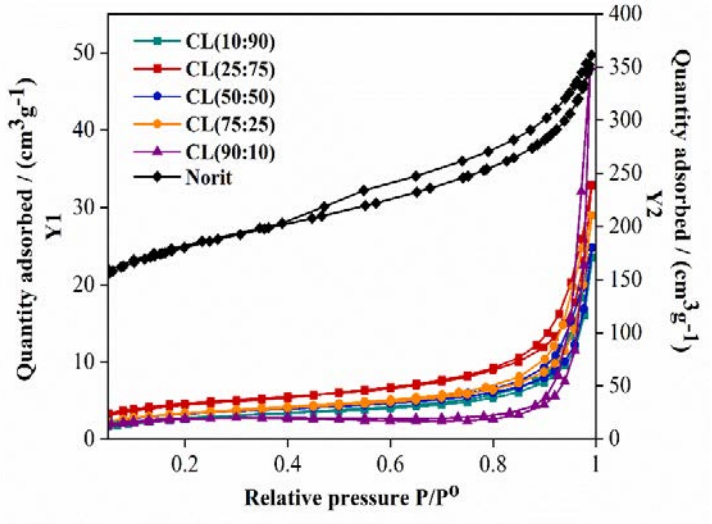

Figure 34. Nitrogen adsorption-desorption isotherms of CL composites and Norit (Quantity adsorbed by CL composites displayed on Y1 axis and quantity adsorbed by Norit displayed on Y2 axis).

To study the thermal degradation of CL composites and individual biopolymers (chitosan and lignin), thermogravimetric analysis (TGA) has been performed under nitrogen atmosphere (Figure 35). Interestingly, the CL composites showed significant changes in the shape of TGA curves compared to chitosan and lignin (Figure 35). The CL composites exhibited improved thermal stability in the range of 100-500 °C compared to lignin and chitosan, which is an indication of the interaction of the composite components. However, Norit is thermally more stable than CL composites, chitosan and lignin (Figure 35).

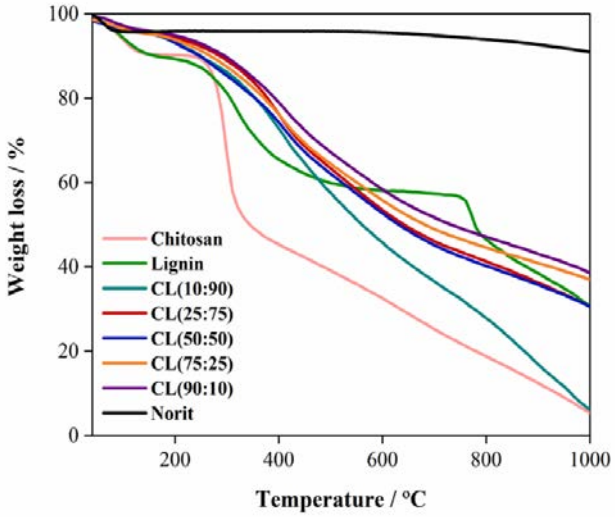

Figure 35. Thermogravimetric analysis (TGA) curves of chitosan, lignin, CL composites and Norit under N_2 atmosphere.

To study the functional groups of CL composites and Norit, FTIR analysis was carried out. No obvious IR bands were observed for Norit except at 2113 cm^{-1}, which refers to the adsorbed carbon monoxide. Though, some distinct features have been observed in the FTIR spectrum of CL composites (Figure 36), which is indicative of chitosan and lignin interaction. The band observed in parent materials for N-H stretching vibrations (3300-3400 cm^{-1}) and O-H stretching vibrations (3200-3550) were disappeared

completely in CL composites, which indicates the probable interaction of chitosan and lignin through hydroxyl group. Moreover, the band observed for C=O stretching vibrations at 1702 cm^{-1} may attribute to the shift in Amide I band present in chitosan (1648 cm^{-1}) or the presence of citric acid in the CL composite. Besides that, the characteristic bands for aromatic ring vibrations (1605, 1506, 1456 cm^{-1}) in lignin remain intact in CL composites. However, the intensity of aforementioned bands reduced with the decrease in lignin proportion in the CL composite. Whereas, the band corresponds to the aryl ether bonds in lignin at 1260 cm^{-1}, disappeared in CL composite, which suggests the cleavage of ether bonds while composite formation. Besides that, the band associated to alkyl substituted ether bonds at 1036 cm^{-1} in lignin has noticeably reduced in intensity with the decrease in the lignin proportion in the CL composite.

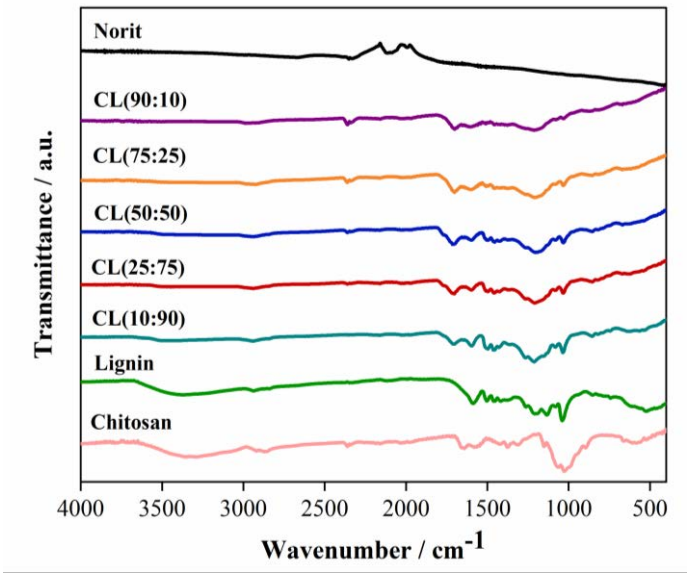

Figure 36. FTIR spectra of chitosan, lignin, Norit and CL composites.

XPS analyses was performed to study the surface functionality and the surface chemical compositions of CL composites and Norit (Figure 37). The deconvolution of C1s spectrum of chitosan, lignin, CL composites and Norit resolved into multiple components that possibly assigned to number of functional groups on the surface.

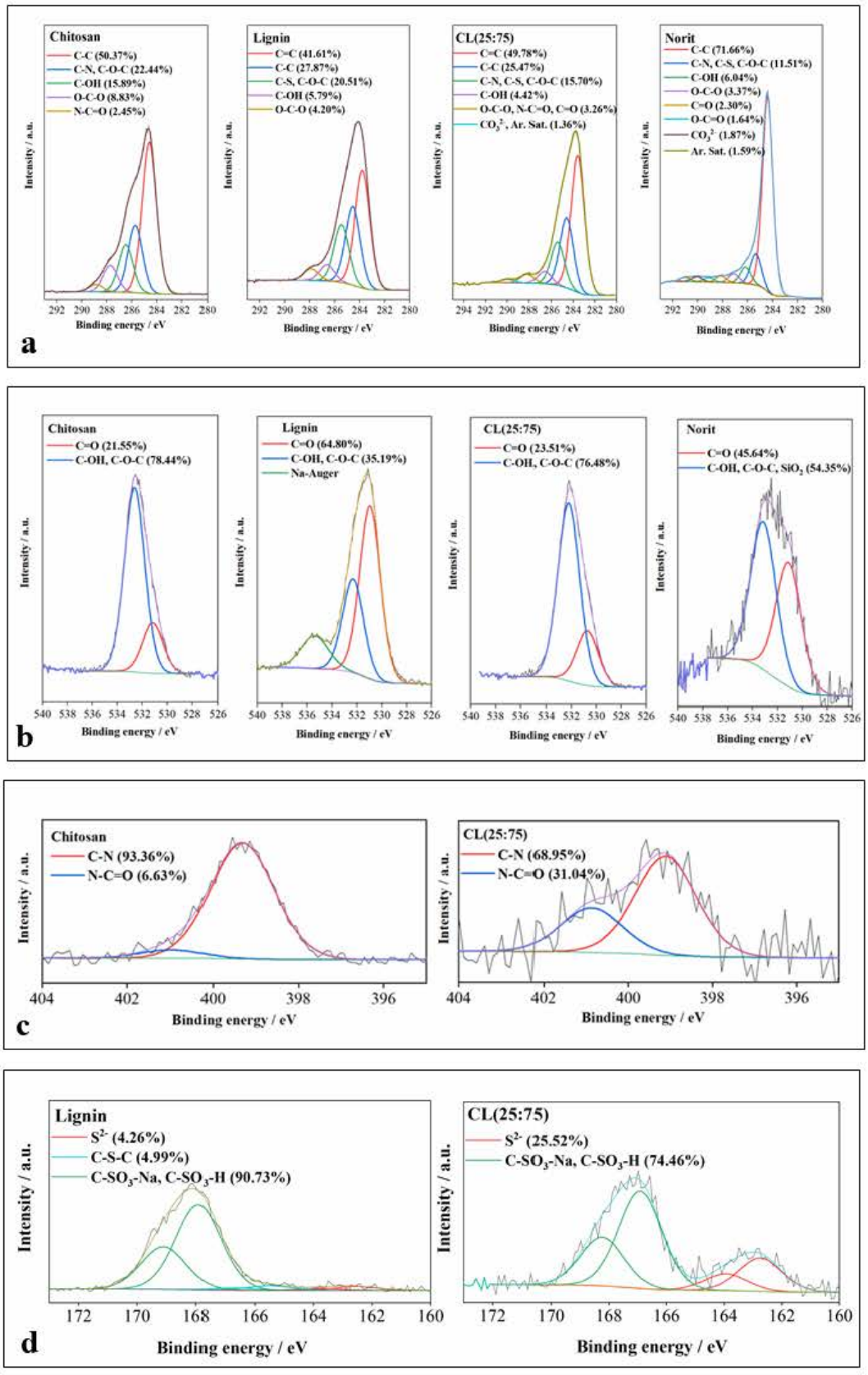

Figure 37. XPS spectra of chitosan, lignin, CL(25:75) and Norit a) C 1s, b) O 1s c) N 1s d) S 2p

Taking CL(25:75) composite as a typical example, the peak observed at 283.5 and 284.6 eV in high-resolution XPS spectrum ascribed to sp^2 carbon (C=C) and sp^3 carbon, respectively (Figure 37a). Whereas, the peak at 285.4 eV corresponds to ether linkages (C-O-C) and carbon bound to nitrogen (C-N) or sulphur (C-S). Besides that, the peak corresponding to alcohol functional group and amide functional group has also observed at 286.6 eV and 288.1 eV, respectively. Moreover, the peak for the carboxylic group (288.5-288.9 eV) have also been observed in the composites, which may arise from the citric acid used in the preparation of composites (Figure 37a). The peak appeared at a higher binding energy (289.9-290.6 eV) was characteristic of aromatic satellites, which may appear due to the presence of lignin (Figure 37a). In the O 1s spectrum of CL(25:75) composite (Figure 37b), the peaks at 530.9 eV and 532.2 eV may correspond to C=O group and C-O group, respectively. Furthermore, the deconvolution of N 1s signal of composite resolved to two peaks (Figure 37c), which is assign to amine (399.1 eV) and amide (400.8 eV) functional groups, due to the presence of chitosan. Whereas, Norit did not show any signal for nitrogen containing surface functional group. Additionally, a few sulphur containing functional moieties were also observed in the composite, which are ascribed to the use of low sulfonate alkali lignin for the synthesis of composite. The peaks (Figure 37d) appeared at 162.7 eV and 163.9 eV corresponds to S $2p_{3/2}$ and S $2p_{1/2}$ of the S^{2-} group, respectively. Whereas, the peaks observed at 166.9 eV and 168.2 eV are related to the alkyl sulfonate group (Figure 37d). However, sulphur containing surface functional moieties were not detected in Norit. The XPS analysis showed the distinct differences in the surface functional moieties of CL composite and Norit, which can play a vital role in determining the characteristic properties of nanocomposite synthesized from titania nanoparticles and CL composites or Norit.

4.2.2 Characterization of titania/chitosan-lignin (T/CL) nanocomposite

The as-synthesized CL composites and Norit (activated carbon) have been used to prepare a series of nanocomposites based on titania nanoparticles. The distinctive properties of the CL-based nanocomposites (75T/CL) have been compared with Norit-based nanocomposite (75T/Norit). X-ray diffraction (XRD) analysis was used to investigate the crystal size and phase composition of pristine titania (SGH-TiO_2), 75T/CL nanocomposites and 75T/Norit nanocomposite. It can be seen in Figure 38, that 75T/CL nanocomposites, 75T/Norit nanocomposite and SGH-TiO_2 showed comparable X-ray diffraction pattern. The XRD reflexes appeared at 25.4 ^{o} (101), 37.9 ^{o} (004), 48.0 ^{o} (200), 54.4 ^{o} (105), 63.2 ^{o} (204), assigned to the anatase phase (JCPDS Card No. 21-1272)[218] of titania (Figure 38). While, the XRD reflex appeared at 30.8 ^{o} (121) refers to the brookite phase (JCPDS no. 29-1360)[219] of titania (Figure 38). Besides that, no remarkable difference was observed with respect to the phase composition and crystal size of SGH-TiO_2, 75T/Norit nanocomposite and 75T/CL nanocomposites. The detailed results for the phase composition and crystal size of the SGH-TiO_2, 75T/Norit nanocomposite and 75T/CL nanocomposites are summarized in Table 6.

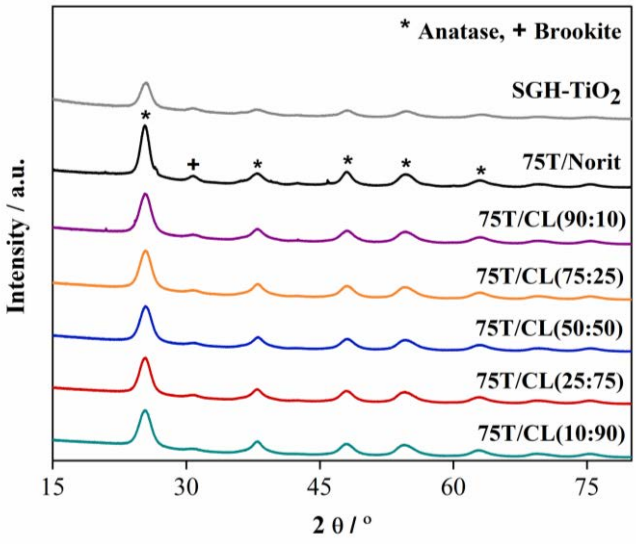

Figure 38. X-ray diffraction (XRD) patterns of 75T/CL nanocomposites, SGH-TiO_2 and 75T/Norit nanocomposite.

In order to study the textural properties (specific surface area and porosity) of as-synthesized nanocomposites, N_2 adsorption-desorption isotherms were measured. As displayed in Figure 39a, that 75T/Norit nanocomposite, 75T/CL nanocomposites and SGH-TiO_2 showed Type IV isotherm and H3 hysteresis, which is indicative of mesoporous materials. Moreover, 75T/CL nanocomposites showed reasonable BET specific surface area in the range of 162-174 m^2g^{-1}, which is also comparable to the specific surface area observed for SGH-TiO_2 (177 m^2g^{-1}). However, the specific surface areas observed for 75T/Norit nanocomposite was slightly higher (269 m^2g^{-1}) than 75T/CL nanocomposites and SGH-TiO_2, which may attribute to the greater specific surface area of Norit (Entry 6, Table 6). Additionally, the pore width distribution analysis (Figure 39b) also suggest that SGH-TiO_2, 75T/CL nanocomposites and 75T/Norit nanocomposite are mesoporous in nature (Entry 7-13, Table 6).

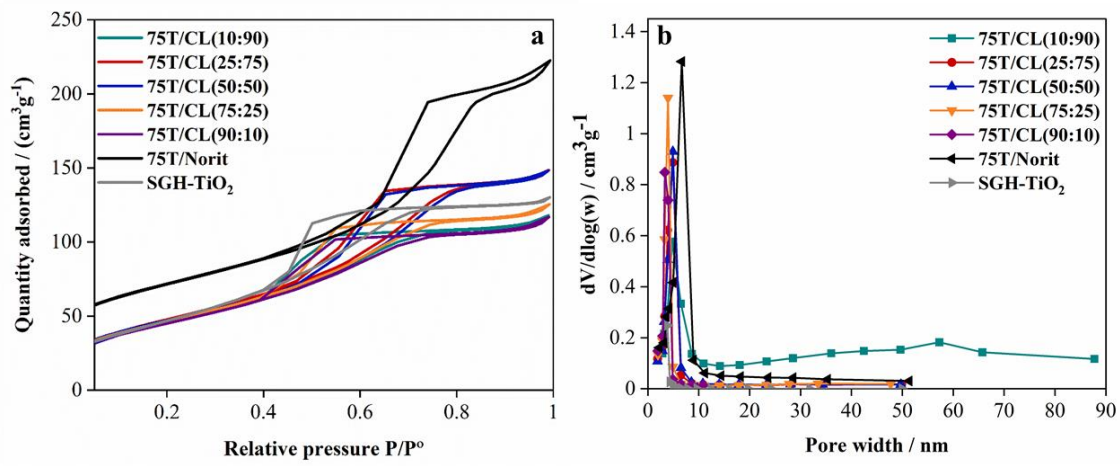

Figure 39. a) Nitrogen adsorption-desorption isotherms of 75T/CL nanocomposites, SGH-TiO_2 and 75T/Norit nanocomposite. b) Pore width distribution in 75T/CL nanocomposites SGH-TiO_2 and 75T/Norit nanocomposite.

TGA measurements (Figure 40) were performed to estimate the actual titania content in the 75T/CL nanocomposites and 75T/Norit nanocomposite. Approximately 26-29% weight loss was observed for nanocomposites after TGA measurements (Figure 40).

The nanocomposites amount remained after TGA measurements (Figure 40) was reasonably comparable to the nominal (75wt%) titania content.

Table 6. Textural (BET-specific surface area (SSA) BJH-pore volume (BJH-Vp) and BJH-pore width (BJH-wp)) and crystallographic features of the samples.

Entries	Samples	SSA/ [m^2g^{-1}]	BJH-Vp/[cm^3/g^{-1}]	BJH-wp/[nm]	Ratio of crystalline phases	Crystal size	
					Anatase:Brookite / %	Anatase / nm	Brookite / nm
1	CL(10:90)	10	NA	NA	NA	NA	NA
2	CL(25:75)	16	NA	NA	NA	NA	NA
3	CL(50:50)	11	NA	NA	NA	NA	NA
4	CL(75:25)	12	NA	NA	NA	NA	NA
5	CL(90:10)	9	NA	NA	NA	NA	NA
6	*Norit	558	0.40	5	NA	NA	NA
7	SGH-TiO_2	177	0.20	3	74:26	5	6
8	75T/CL(10:90)	162	0.32	6	83:17	5	6
9	75T/CL(25:75)	174	0.23	3	79:21	5	6
10	75T/CL(50:50)	170	0.23	4	78:22	5	6
11	75T/CL(75:25)	169	0.19	3	81:19	5	6
12	75T/CL(90:10)	164	0.18	3	74:26	5	5
13	*75T/Norit	239	0.35	5	66:30	6	8

*Sample contain traces of silica

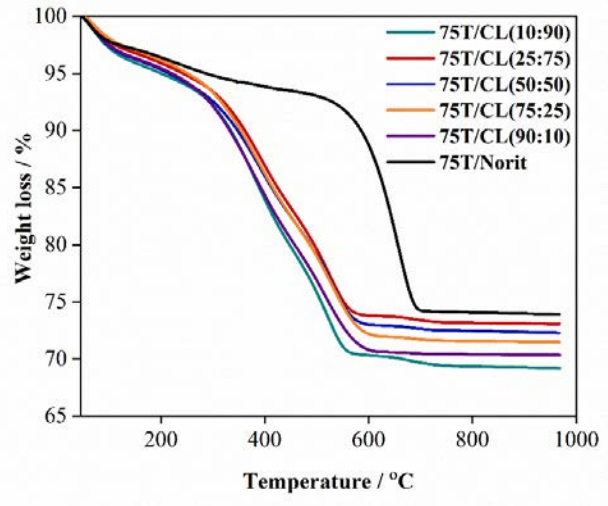

Figure 40. Thermogravimetric analysis (TGA) curves of 75T/CL nanocomposites and 75T/Norit nanocomposite.

To explore the optical properties of the as-synthesized nanocomposites and SGH-TiO_2, DRS-UV-Visible- absorption spectra were measured in the range of 220-800 nm. It can be seen in Figure 41a, that the 75T/Norit nanocomposite and 75T/CL nanocomposites showed absorption in the entire UV-visible region (220-800 nm), which is possibly advantageous for visible light photocatalysis. However, SGH-TiO_2 showed a distinctive absorption edge in the UV region. The optical band gap estimated for SGH-TiO_2 via Kubelka-Munk function was ~3.3 eV (Figure 41b). Whereas, the shape of the DRS-UV-visible absorption spectra of nanocomposite did not allow to calculate the band gap of titania. However, to further examine the CL composite effect on the optical band gap of titania, the nanocomposite was synthesized with the 99:1 ratio of titania nanoparticles and CL composite. However, the optical band gap of titania seems unaffected (Figure 41b), which suggests the surface interaction of CL composite with the titania nanoparticles, and also indicates that the bulk properties of titania remains same.

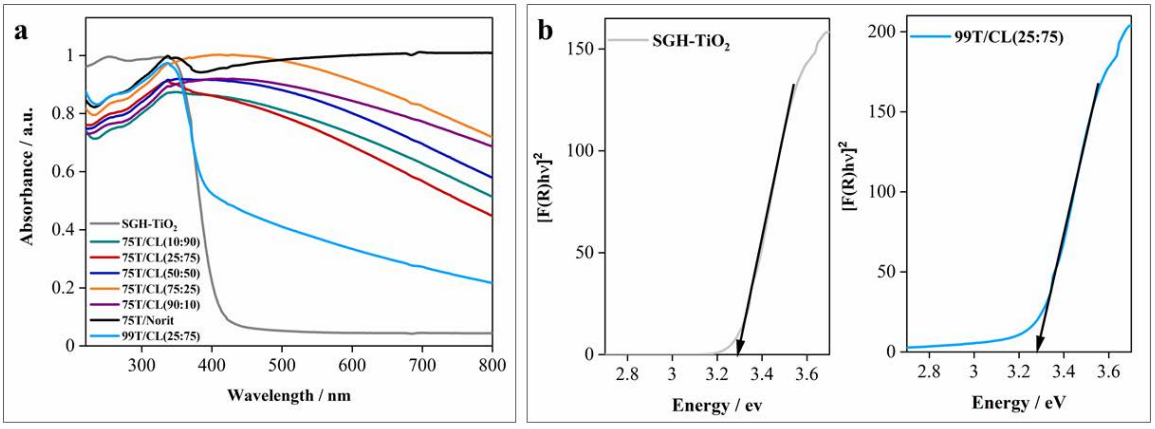

Figure 41 a) UV-Visible-DRS absorption spectra of 75T/CL nanocomposites, SGH-TiO_2 and 75T/Norit nanocomposite b) Optical band gap of SGH-TiO_2 and 99T/CL(25:75).

To study the functional groups of 75T/Norit nanocomposite and 75T/CL nanocomposite, FTIR analysis was carried out (Figure 42). A broad band appeared at 580-800 cm^{-1} in the 75T/CL nanocomposite and 75T/Norit nanocomposite may ascribe to Ti-O-Ti bridge stretching modes. Though, the IR bands related to CL composites have not been observed in 75T/CL nanocomposites possibly due to high (75wt%) titania content in the nanocomposites. Furthermore, the elemental analysis of the 75T/CL nanocomposites was performed to evaluate the elemental composition, and the results are summarized in Table 5 (Entry 9-13).

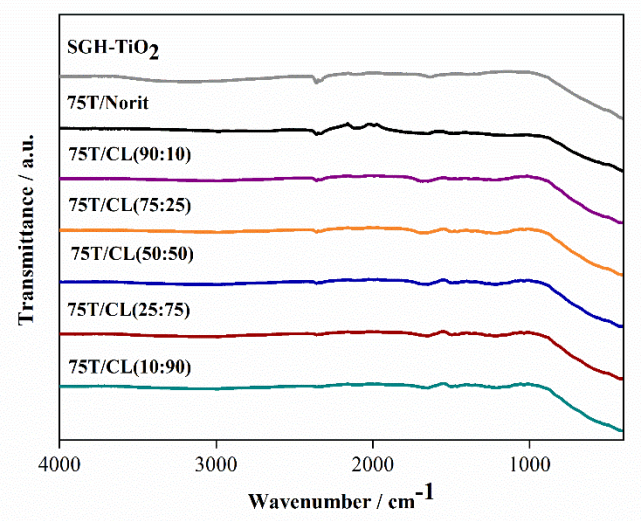

Figure 42. FTIR spectra of 75T/CL nanocomposites, SGH-TiO_2, and 75T/Norit nanocomposite.

X-ray photoelectron spectroscopy (XPS) was used to study the distinct surface functionality of 75T/Norit nanocomposite and 75T/CL nanocomposites (Figure 43). Taking 75T/CL(25:75) as typical example, the Ti 2p signal of 75T/CL(25:75) nanocomposite was deconvoluted into four peaks (Figure 43b), the peaks appeared at 458.6 and 464.3 eV corresponds to Ti^{4+} $2p_{3/2}$ and Ti^{4+} $2p_{1/2}$, respectively. Whereas, the peaks observed at 457.0 and 462.8 eV indexed to Ti^{3+} $2p_{3/2}$ and Ti^{3+} $2p_{1/2}$, respectively. Ti^{3+} is usually defined as a surface defect of titania, which can possibly plays an

imperative role in photocatalysis by inhibiting electron-hole recombination, and improving the visible light activity.[235]

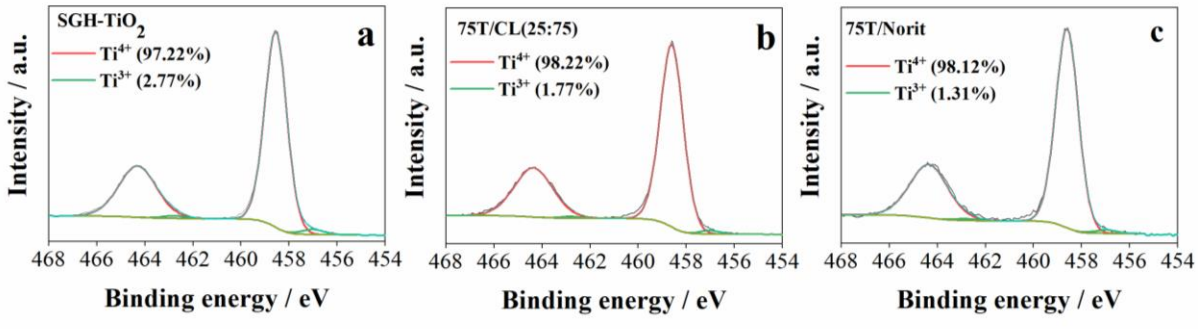

Figure 43. Ti 2p XPS spectra of a) SGH-TiO_2, b) 75T/CL(25:75) and c) 75T/Norit

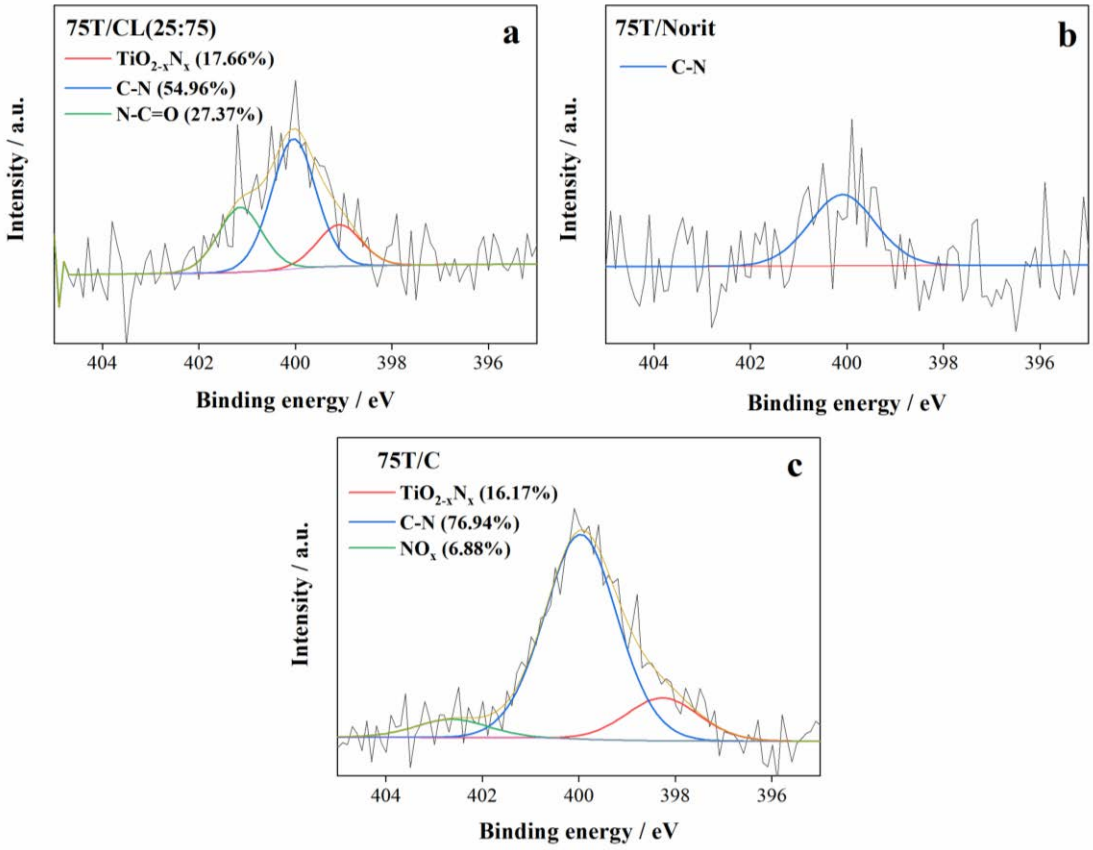

Figure 44. N 1s XPS spectra of a) 75T/CL(25:75) b) 75T/Norit and c) 75T/C

Furthermore, nitrogen-containing functional groups were detected in 75T/CL(25:75) nanocomposite (Figure 44a) and 75T/Norit nanocomposite (Figure 44b). The

deconvolution of N 1s spectrum of 75T/CL(25:75) nanocomposite resolved to three chemical states of nitrogen (Figure 44a). The peaks appeared at 400.0 and 401.1 eV may attribute to C-N and N-C=O functional groups, respectively. While, the peak observed at 399.0 eV is possibly ascribe to the substitution of oxygen with nitrogen in the titania framework, suggesting the formation of N-Ti-O bond.[236, 237] This could be advantageous from the viewpoint of photocatalytic activity of 75T/CL(25:75) nanocomposite under visible light. It is suggested that, substitution of oxygen with nitrogen into titania framework is related to the presence of chitosan. To confirm that hypothesis two new set of nanocomposites has been synthesized by combining titania with chitosan (75T/C) and lignin (75T/L). 75T/L nanocomposite did not show any nitrogen signal. However, 75T/C showed a signal corresponding to N-Ti-O bond at 398.2 eV (Figure 44c), which indicates that nitrogen incorporation in 75T/CL(25:75) nanocomposite is associated with the presence of chitosan. Conversely, no N element signals were detected in SGH-TiO_2. The core level N 1s spectrum of 75T/Norit was deconvoluted into single peak (Figure 44b), observed at 400.1 eV, which refers to C-N functional moiety. The C-N functional moiety may observe in 75T/Norit due to the atmospheric interaction, as N was not found in Norit during elemental and XPS analysis. TEM analysis was carried out to further corroborate the phase composition average particle size and the morphology of the SGH-TiO_2, 75T/CL (25:75) and 75T/Norit (Figure 45a-c). It was found that SGH-TiO_2, 75T/CL (25:75) and 75T/Norit composed of anatase and brookite phase (Figure 45a-c), Additionally, SGH-TiO_2, 75T/CL (25:75) and 75T/Norit showed similar average particle size i.e. 6 nm (Figure 46a-c). Nevertheless, the particle size observed for SGH-TiO_2, 75T/CL (25:75) and 75T/Norit nanocomposite appears quite larger than the mean size (Figure 45a-c), possibly because of agglomeration. However, the results of TEM measurements are comparable with the XRD results.

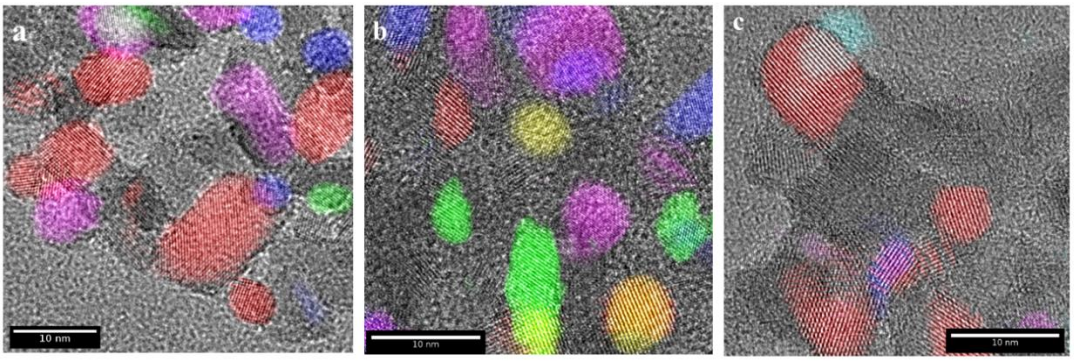

Figure 45. High resolution TEM image of a) SGH-TiO_2 b) 75T/CL(25:75) nanocomposite c) 75T/Norit nanocomposite (The legend showed the crystal planes and lattice spacing (nm)).

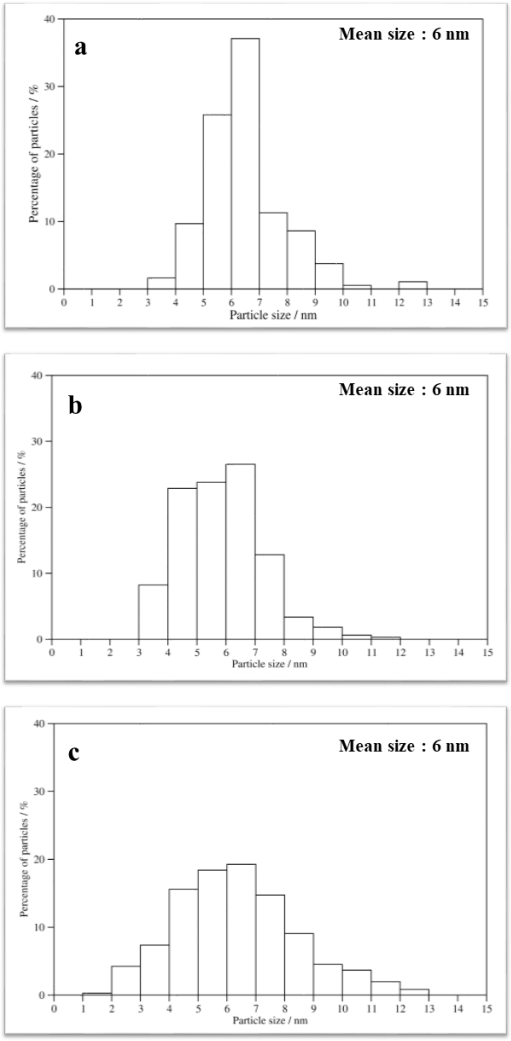

Figure 46. Particle size distribution in a) SGH-TiO_2 b) 75T/CL(25:75) nanocomposite c) 75T/Norit nanocomposite.

Electrochemical impedance spectroscopy (EIS) was applied to elucidate the charge transfer ability of SGH-TiO_2, 75T/CL(25:75) nanocomposite and 75T/Norit nanocomposite, and their Nyquist plots are presented in Figure 47a. Generally, Nyquist plots' arc radius represents the charge transfer resistance between the electrolyte solution and catalysts. As shown in EIS spectrum (Figure 47a), the 75T/CL(25:75) nanocomposite exhibited smaller arc radius than 75T/Norit nanocomposite and SGH-TiO_2. This represents the faster interfacial charge transfer and enhanced charge separation efficiency[194,238] on 75T/CL(25:75), which might be advantageous for photocatalytic point of view. Additionally, the photocurrent response of 75T/CL(25:75) nanocomposite under visible light is relatively higher (Figure 47b) than SGH-TiO_2, which further indicates that the 75T/CL(25:75) has better charge transfer ability under visible light illumination. Conversely, 75T/Norit was not photoactive under the visible light as it has not shown any response when the light was switched on and off (Figure 47b). However, the noise observed in the signal of 75T/Norit (Figure 47b) may refers to the imperfect contact between the electrolyte and electrode surface.

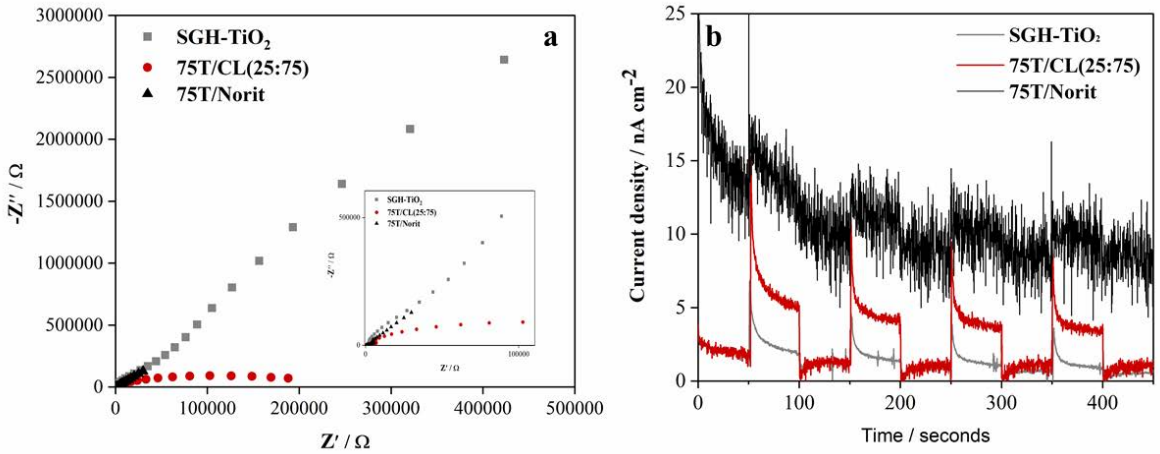

Figure 47. a) EIS Nyquist plots of SGH-TiO_2, 75T/CL(25:75) and 75T/Norit (b) transient photocurrent responses SGH-TiO_2, 75T/CL(25:75) and 75T/Norit.

4.2.3 Photocatalytic activity of the titania/chitosan-lignin (T/CL) nanocomposite for the selective oxidation of benzyl alcohol (BnOH) under UV light

The photocatalytic activity of 75T/CL nanocomposites, SGH-TiO_2, 75T/Norit nanocomposite and physical mixture (75T/CL(25:75)-PM) of SGH-TiO_2 and CL(25:75) was evaluated for the selective oxidation of benzyl alcohol (BnOH) to benzaldehyde (Bnald) under UV light (375 nm) in acetonitrile. 75T/Norit nanocomposite and SGH-TiO_2, both showed high photocatalytic activity under UV light for the oxidation of BnOH, with 82% and 97% BnOH conversion after 4 hours of irradiation, respectively (Figure 48a). However, the series of prepared 75T/CL nanocomposite (75T/CL(10:90), 75T/CL(25:75), 75T/CL(50:50), 75T/CL(75:25) and 75T/CL(90:10)), demonstrated relatively lower photocatalytic activity under UV light, with BnOH conversion in the range of 38-55% after 4 hours of irradiation (Figure 48a). Furthermore, changing the proportion of chitosan and lignin within the 75T/CL nanocomposites did not affect their photocatalytic activity to a larger extent (Entries 2-6, Table 7). Interestingly, the physical mixture (75T/CL(25:75)-PM) showed 46% BnOH conversion (Figure 48a) after 4 hours of irradiation, which was comparable to the BnOH conversion achieved by 75T/CL nanocomposites. The high (97%) BnOH conversion achieved by SGH-TiO_2 might be related to the high oxidizing power of titania under UV light. Besides that, the formation of highly reactive $^{\bullet}OH$ radicals, due to the presence of surface OH groups of titania (Ti-OH) may also enhance the BnOH conversion. To further investigate, whether the comparatively lower activity of 75T/CL nanocomposites is linked with overall lower content of titania (75wt%) or not, an experiment was carried out with higher loading (1.35g/L) of nanocomposite (75T/CL(25:75), which contain the same amount of titania as in 1g/L of SGH-TiO_2. It was found that, with the same amount of titania the BnOH conversion was not increased

substantially (Entry 7, Table 7). This suggests that the overall content of titania may not be decisive for the enhanced photocatalytic activity of SGH-TiO_2. Additionally, 75T/CL nanocomposites formed blackish-brown suspension, which affects the light absorption possibly due to increased shielding effect and opacity which results in their lower photocatalytic activity. Whereas, the enhanced photocatalytic activity of 75T/Norit nanocomposite under UV light in comparison with 75T/CL nanocomposites may ascribe to its relatively higher (239 m^2g^{-1}) specific surface area. However, the crystal size and phase composition of 75T/Norit nanocomposite, SGH-TiO_2, and 75T/CL nanocomposites were comparable (Entries 7-13 Table 6) and possibly not related to their different photocatalytic activity. Interestingly, 75T/CL nanocomposites exhibited high selectivity (>90%) for Bnald under UV light over the course of reaction, in comparison with 75T/Norit nanocomposite and SGH-TiO_2 (Figure 48b).

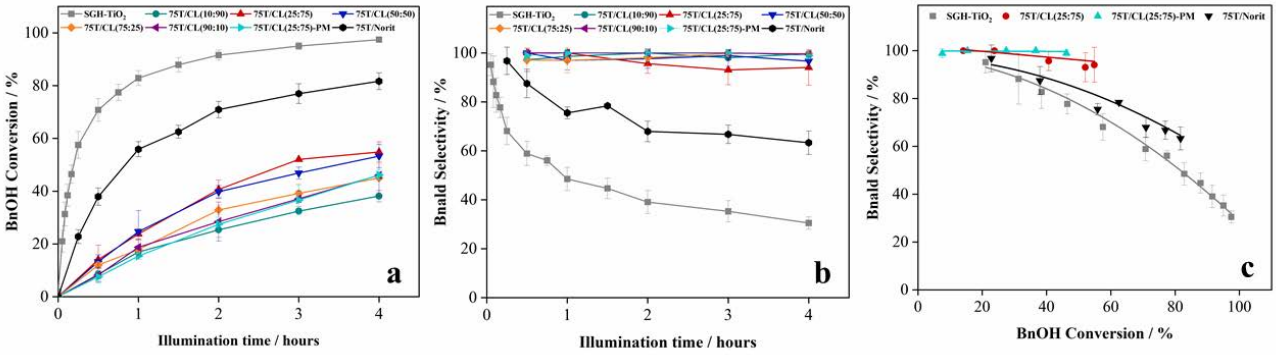

Figure. 48 a) BnOH conversion profile of 75T/CL nanocomposites, SGH-TiO_2 and 75T/Norit nanocomposite as a function of time under UV light (375 nm) b) Bnald selectivity profile of 75T/CL nanocomposites, SGH-TiO_2 and 75T/Norit nanocomposite as a function time under UV light (375 nm) c) BnOH Conversion versus Bnald selectivity plot for 75T/CL(25:75) nanocomposite, SGH-TiO_2 and 75T/Norit nanocomposite under UV light (375 nm).

Table 7. The summary of the photocatalytic oxidation of BnOH over titania and titania/chitosan-lignin (T/CL) nanocomposite.

Entries	photocatalyst	Light	BnOH Conv. / %	Bnald Sel. / %	C Balance / %
1	SGH-TiO_2	UV	[a]58	68	81
2	75T/CL(10:90)	UV	38	100	100
3	75T/CL(25:75)	UV	55	94	97
4	75T/CL(50:50)	UV	53	97	98
5	75T/CL(75:25)	UV	45	100	100
6	75T/CL(90:10)	UV	46	99	<99
7	[b]75T/CL(25:75)	UV	62	92	95
8	75T/Norit	UV	[c]56	76	87
9	Phys. Mix. (TiO_2: CL(25:75))	UV	46	99	<99
10	85T/CL(25:75)	UV	[d]59	79	88
11	95T/CL(25:75)	UV	[e]58	75	86
12	99T/CL(25:75)	UV	[a]47	82	92
13	75T/C	UV	52	100	100
14	75T/L	UV	6	100	100
15	SGH-TiO_2	Visible	0.0	0.0	100
16	75T/CL(10:90)	Visible	12	100	100
17	75T/CL(25:75)	Visible	19	100	100
18	75T/CL(50:50)	Visible	16	100	100
19	75T/CL(75:25)	Visible	14	100	100
20	75T/CL(90:10)	Visible	15	100	100
21	[b]75T/CL(25:75)	Visible	30	99	<99
22	75T/Norit	Visible	0.0	0.0	100
23	Phys. Mix. (TiO_2: CL(25:75))	Visible	0.0	0.0	100
24	85T/CL(25:75)	Visible	17	100	100

25	95T/CL(25:75)	Visible	33	100	100
26	99T/CL(25:75)	Visible	12	100	100
27	75T/C	Visible	14	100	100
28	75T/L	Visible	0.0	0.0	100
29	75T/CL(25:75)	Dark	0.0	0.0	100
30	99T/C	visible	16	94	99
31	99T/C	UV	[f]62	67	78

(**Reaction conditions:** BnOH (0.5mM, 0.01 mmol), photocatalyst (1g/l, 20 mg), reaction time (4 hours), reaction medium (acetonitrile), BnOH solution volume (20 mL) incident light wavelength (UV: 375 nm, Visible: 515 nm), incident light intensity was (6 x ~9 W/m^2), [a]reaction time (15 minutes), [b]catalyst loading (1.35 g/L) [c]reaction time (1 hour) [d]reaction time (2 hours), [e]reaction time (45 minutes) [f]reaction time (30 minutes).

To further confirm that the increased Bnald selectivity is not related to the lower activity, and therefore BnOH conversion vs Bnald selectivity has been plotted (Figure 48c) for 75T/Norit nanocomposite, SGH-TiO_2, 75T/CL(25:75) nanocomposite (a representative catalyst chosen from the 75T/CL nanocomposite series) and physical mixture (75T/CL(25:75)-PM). It is clearly seen (Figure 48c) that, at a lower (~21%) BnOH conversion all the photocatalysts showed high (>90%) Bnald selectivity. Though, at a higher (~50%) BnOH conversion 75T/CL(25:75)-PM and 75T/CL(25:75) nanocomposite demonstrated high (>90%) Bnald selectivity. The lower (68%) Bnald selectivity exhibited by SGH-TiO_2 (Entry 1, Table 7) may attribute to the generation of highly reactive species such as h^+ and $^{\bullet}OH$ by SGH-TiO_2 under UV light irradiation, which may lead to the over-oxidation of BnOH. In addition, the produced Bnald could possibly compete with BnOH for the active sites for further oxidation till mineralization. On the contrary, the high Bnald selectivity demonstrated by

75T/CL(25:75) nanocomposite and 75T/CL(25:75)-PM suggest that, the CL composite present in the reaction medium either as physical mixture or nanocomposite may prevent the mineralization reaction.

Additionally, it is conjectured that CL composite may act as a radical ($O_2^{-\bullet}$, $^{\bullet}OH$) scavenger and thus hinder the undesirable over-oxidation reactions. To substantiate that hypothesis, the SGH-TiO_2 catalyzed BnOH oxidation was performed in the presence of different radical scavengers (Figure 49). When dimethylsulfoxide (DMSO) was added as a $^{\bullet}OH$ radical scavenger (SGH-TiO_2-DMSO), the BnOH conversion was slowed down initially (Figure 49a). However, no considerable changes in the conversion of BnOH (91%) was observed after 4 hours of irradiation. This suggest that $^{\bullet}OH$ may have a minor contribution in the oxidation of BnOH. This is in agreement with the fact which is known from the literature, that only limited number of $^{\bullet}OH$ might be formed from a UV-illuminated water-saturated surface of titania in acetonitrile (as solvent).[239-240]

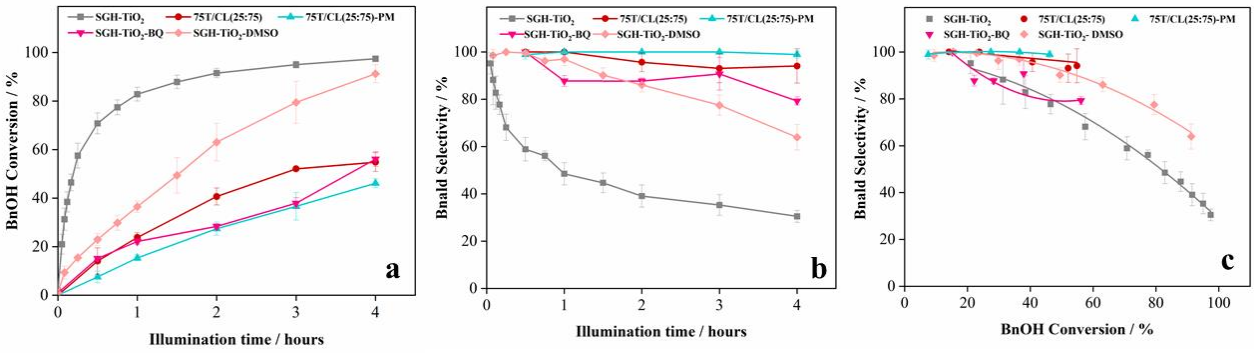

Figure 49 a) Effect of radical scavenger on BnOH conversion profile of SGH-TiO_2, as a function of time under UV light (375 nm) b) Effect of radical scavenger on Bnald selectivity profile of SGH-TiO_2, as a function of time under UV light (375 nm) c) Effect of radical scavenger on BnOH conversion versus Bnald selectivity plot for SGH-TiO_2, under UV light (375 nm).

Though, the enhanced selectivity of Bnald in the presence of DMSO ($^{\bullet}$OH scavenger) suggests the inhibition of undesirable over-oxidation reaction driven by $^{\bullet}$OH. However, the use of benzoquinone (BQ) as superoxide radical anion ($O_2^{-\bullet}$) scavenger (SGH-TiO_2-BQ) reduced the BnOH conversion up to ~50% (Figure 49a), suggesting that $O_2^{-\bullet}$ is one of the dominant species for the oxidation of BnOH. Although, the selectivity of Bnald was not affected (Figure 49b), this suggests that $O_2^{-\bullet}$ scavenger may impede the BnOH oxidation. However, the BnOH oxidation is still accomplished by other radical species. Furthermore, these results also indicate that CL composite could possibly act as radical scavenger and decrease the BnOH oxidation (by scavenging $O_2^{-\bullet}$) and enhance the selectivity of Bnald (by $^{\bullet}$OH scavenging). Additionally, the enhanced selectivity of Bnald (>90%) achieved by 75T/CL(25:75) nanocomposite and 75T/CL(25:75)-PM (Figure 49c), in comparison with 75T/Norit nanocomposite (76%) and SGH-TiO_2 (68%) also proposed that there is possibly an interaction of SGH-TiO_2 and CL(25:75) either as physical mixture or nanocomposite within the suspension (reaction medium), that hinders the mineralization reaction and assist in the partial oxidation of BnOH to Bnald.

Moreover, the impact of titania content in the nanocomposite on the selective oxidation of BnOH under UV light has also been explored. As depicted in Figure 50a, the conversion of BnOH was improved with the increase in titania content in the nanocomposite. Though, the Bnald selectivity (Figure 50b and 50c) has been decreased with higher content (>75wt%) of titania (Entries 10-12, Table 7). To further evaluate the contribution of lignin and chitosan on the activity of 75T/CL nanocomposites, the nanocomposites synthesized by combining titania with chitosan (75T/C) and lignin (75T/L) were also tested for the selective oxidation of BnOH under UV light.

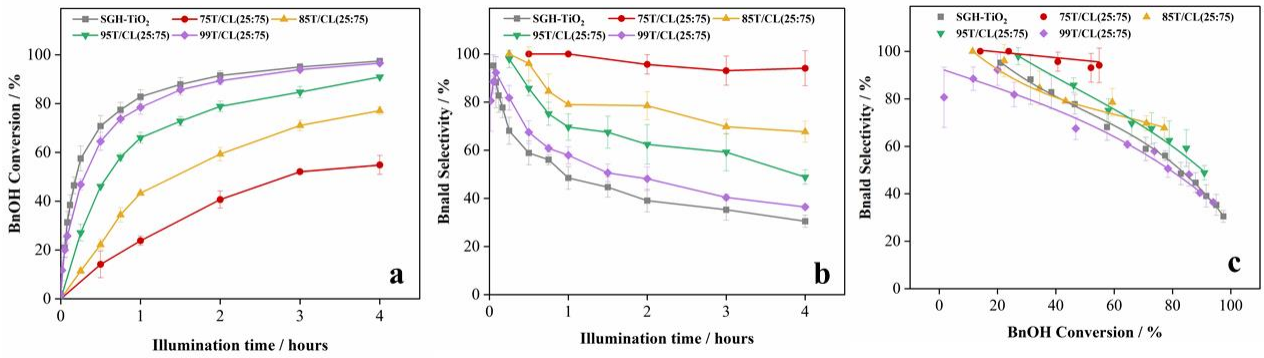

Figure 50 a) Effect of titania content in nanocomposites on the BnOH conversion profile as a function of time under UV light (375 nm) b) Effect of titania content in nanocomposites on the Bnald selectivity profile as a function time under UV light (375 nm) c) Effect of titania content in nanocomposites on BnOH conversion versus Bnald selectivity plot under UV light (375 nm).

Interestingly, 75T/C nanocomposite exhibited (Entry 13, Table 7) comparable photocatalytic activity with respect to conversion of BnOH (52%) and selectivity of Bnald (100%) as 75T/CL nanocomposites (Entries 2-6, Table 7). Whereas, 75T/L nanocomposite exhibited negligible conversion for BnOH (Entry 14, Table 7) under UV light after 4 hours of irradiation. The negligible activity of 75T/L nanocomposite may ascribe to the improved UV shielding capability of lignin in the absence of chitosan. However, this is not a direct evidence, it is proposed that lignin could encapsulate the titania and probably block the UV light in the absence of chitosan and hindered the photocatalytic activity of titania. Recently, there is a growing interest to use lignin in sunscreen to scavenge the photocatalytic activity of titania owing to its UV blocking tendency.[241, 242]

4.2.4 Photocatalytic activity of the titania/chitosan-lignin (T/CL) nanocomposite for the selective oxidation of benzyl alcohol (BnOH) under visible light

The photocatalytic activity of the 75T/CL nanocomposites was also evaluated under visible light (515 nm) for the selective oxidation of BnOH to Bnald. Interestingly, 75T/CL nanocomposites were found to be photocatalytically active under visible light for the selective oxidation of BnOH (Figure 51a). However, compared to UV light the conversion of BnOH attained by 75T/CL nanocomposites after 4 hours of irradiation under visible light was much lower (<20%). Though, all the 75T/CL nanocomposites showed high (100%) selectivity for Bnald after 4 hours of irradiation (Figure 51a). 75T/CL(25:75)-PM, 75T/Norit and SGH-TiO_2, observed to be photocatalytically inactive under visible light for the selective oxidation of BnOH (Figure 51a). It is proposed that the photocatalytic activity of 75T/CL nanocomposites under visible light may attribute to the nitrogen doping of titania by the CL composite. The N 1s core level XPS spectrum of a representative sample i.e. 75T/CL(25:75) nanocomposite indicated that the substitutional N-doping (Figure 44a) of titania may lead to the activity of 75T/CL nanocomposites under visible light. It is in agreement with the fact that, this kind of interaction of nitrogen and titania has not been observed for 75T/Norit nanocomposite and SGH-TiO_2, which did not show any photocatalytic activity under visible light. It is proposed that the nitrogen incorporation into the framework of titania may lead to the creation of a new mid-gap energy level (the N 2p band over the O 2p valence band), which decreases the titania band gap.[243] Although, 75T/CL nanocomposite exhibited absorption (Figure 41a) in the entire UV-Visible spectrum. It is therefore challenging to estimate the change in the absorption of titania to the visible region ascribe to the probable N-doping. However, to elucidate the probable shift in the optical band-gap of titania due to CL composite N-doping, the UV-Visible-DRS

absorption spectrum was measured for nanocomposites containing higher (99wt%) titania content i.e. 99T/CL(25:75). As shown in Figure 41b, no changes in the optical band-gap of SGH-TiO_2, and 99T/CL(25:75) nanocomposite was observed. It is therefore suggested that titania N-doping by CL composites may result in surface modification via bonding of nitrogen,[243] whereas the bulk material is in the intrinsic configuration of pristine titania. In addition, N-doping could potentially reduce the recombination of photogenerated electron-hole pair, which can play an important role in improving the selectivity and photocatalytic activity.[244,89] It is shown by the EIS Nyquist plots (Figure 47a) and transient photocurrent response (Figure 47b) that 75T/CL(25:75) nanocomposite exhibited improved charge transfer in comparison with SGH-TiO_2 and 75T/Norit nanocomposite.

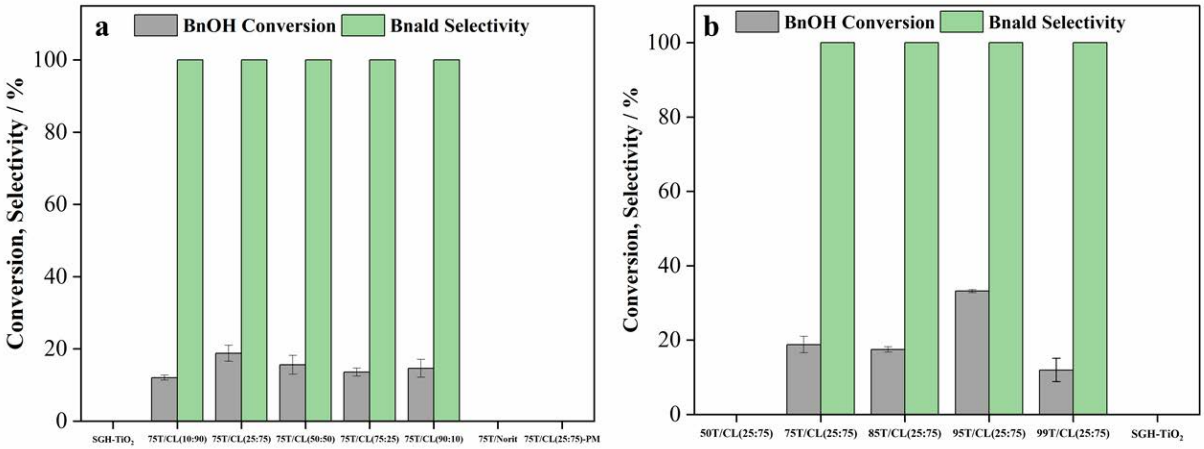

Figure 51. a) Photocatalytic performance of 75T/CL nanocomposites, SGH-TiO_2 and 75T/Norit nanocomposite for the selective oxidation of BnOH under visible light (515 nm) b) Effect of titania content on the photocatalytic performance of nanocomposites for the selective oxidation of BnOH under visible light (515 nm).

Furthermore, it was found that varying the content of titania in the nanocomposite also affect their activity under visible light. Increasing the titania content in the

nanocomposite up to 95wt% (95T/CL(25:75), increases the conversion of BnOH up to 33% after 4 hours of irradiation (Figure 51b). However, increasing the content of titania further up to 99wt% (99T/CL(25:75) reduced the conversion of BnOH (12%), though the selectivity of Bnald was not affected (Entry 26, Table 7). The reduction in the conversion of BnOH with increasing content of titania (99wt%) could be linked to the lower chances of N-doping owing to the lesser CL amount.

4.2.5 Apparent quantum yield (AQY)

The photon flux absorbed under UV and visible light by the photocatalytic system was estimated to be 8.70×10^{-9} and 11.63×10^{-9} E s^{-1}, respectively. Whereas, AQY exhibited by 75T/CL(25:75) nanocomposite, SGH-TiO_2, and 75T/Norit nanocomposite for Bnald formation under UV light after 4 hours of irradiation was estimated to be 4.1%, 2.3%, and 4.1%, respectively. Additionally, the AQY exhibited by 75T/CL(25:75) nanocomposite was 1.1% after 4 hours of irradiation under visible light. The observed AQY are similar to the literature reported efficiency of Au/TiO_2 nanorods (3.4%)[245] and Pd-deposited CdS-TiO_2 composite (1.4%)[246] for the selective oxidation of BnOH at >420 nm and 540 nm, respectively.

4.2.6 Stability and reusability of 75T/CL(25:75) nanocomposite

To assess the stability of 75T/CL(25:75) nanocomposite, titanium leaching of 75T/CL(25:75) nanocomposite was evaluated by XRF analysis of BnOH solution after 4 hours of photocatalytic reaction. As shown in Figure 52, 75T/CL(25:75) nanocomposite did not show any leaching of titanium under UV and visible light. The peaks appeared refers to Rh from Rh lamp, Fe and Cu signals that are finger print of the spectrometer. Furthermore, UV-Visible absorption spectra measured to evaluate the stability of carbon materials in 75T/CL(25:75) nanocomposite in acetonitrile under dark

and light irradiation (UV and visible) showed the leaching (Figure 53) of constituents of 75T/CL(25:75) nanocomposite.

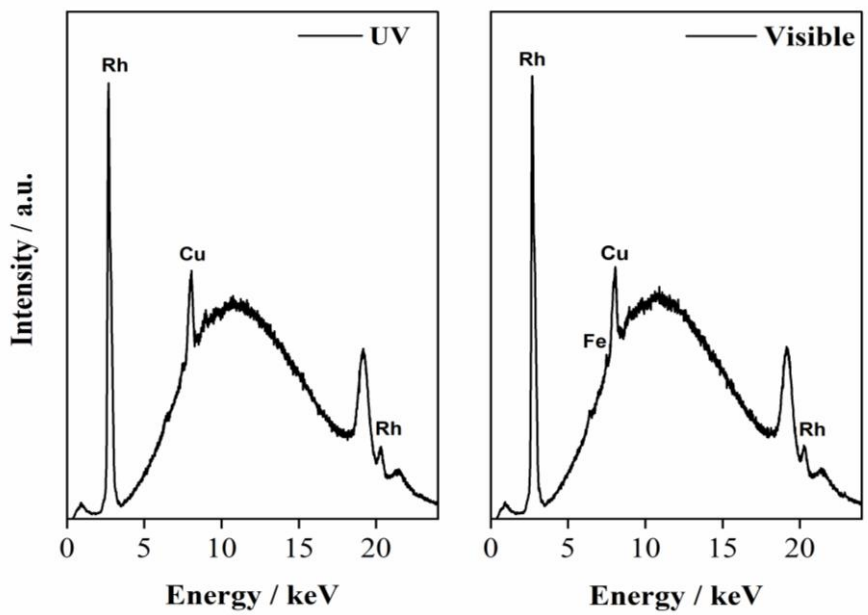

Figure 52. XRF analysis of BnOH solution catalyzed over 75T/CL(25:75) nanocomposite.

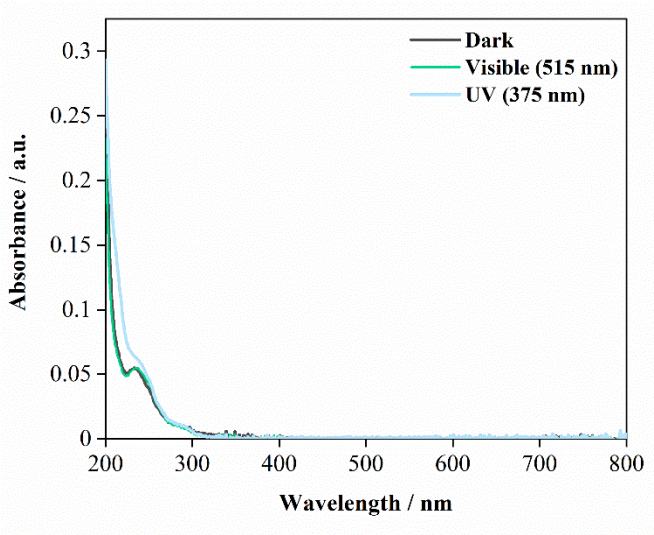

Figure 53. UV-Visible absorption spectra of 75T/CL(25:75) extracts in acetonitrile.

The GC-MS analysis showed the traces of oleanitrile, acetamide, tetradecanamide, hexadecanamide, 9-octadecenamide and 2,4-dimethyl-benzaldehyde in the liquid phase extracts obtained after the stability experiments carried out under dark and light irradiation (UV and visible) for 4 hours. The 2,4-dimethyl-benzaldehyde could be detected due to the lignin fragmentation. However, the other compounds may be observed from the chitosan depolymerization or formerly present as oligomers impurity in the chitosan. To evaluate the recyclability of the 75T/CL(25:75) nanocomposite, reusability experiments were performed for the selective oxidation of BnOH under the UV and visible light. As shown in Figure 54a and 54b, 75T/CL(25:75) nanocomposite maintained its activity after multiple run for the selective oxidation of BnOH to Bnald under the UV and visible light.

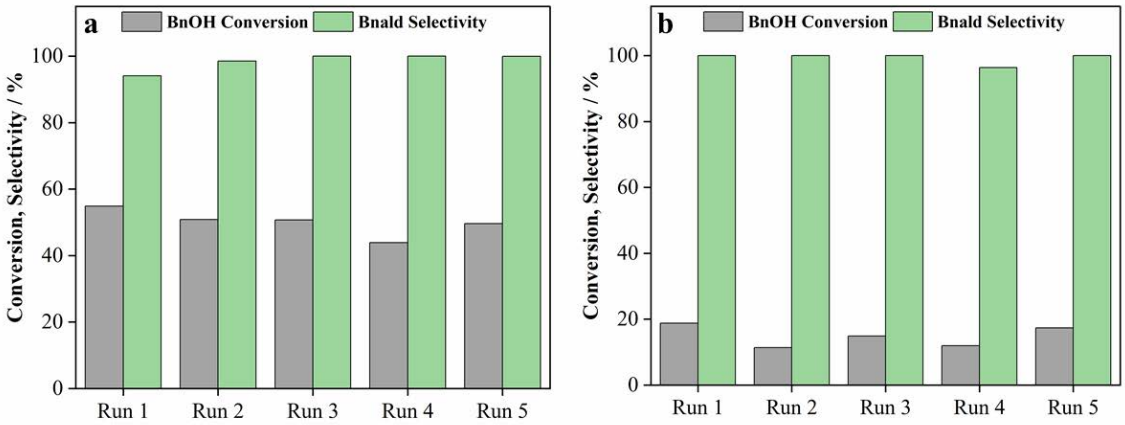

Figure 54. The recycling of 75T/CL(25:75) nanocomposite for the selective oxidation of BnOH under a) UV light (375 nm) irradiation b) visible light (515 nm) irradiation.

4.2.7 Conclusions

In conclusion, blending chitosan with lignin through a hydrothermal method formed a composite with improved physicochemical properties. Moreover, chitosan-lignin (CL)

composites with multiple functional groups potentially interacted with titania and formed a nanocomposite (T/CL). This coupling of CL composite with titania not only improved the selectivity to Bnald in BnOH oxidation reaction under UV light but also stimulates the visible light activity. The interaction of chitosan and titania plays a decisive role in the visible light activity. According to XPS measurements, it is suggested that the T/CL nanocomposites and 75T/C nanocomposites activity under visible light may ascribed to the doping of nitrogen into titania framework from chitosan. However, no direct evidence related to the reduction of band-gap of titania was observed upon amalgamation with CL composite, and visible light activity was ascribed to the nitrogen doping of titania. Besides that, the inactivity of 75T/L under visible light showed that the visible light activity of T/CL nanocomposites may not be attributed to the photosensitizing effect of lignin. Whereas, the improved efficiency of T/CL nanocomposites under UV light probably be associated to the radical scavenging effect of CL composites. It is therefore concluded that nanocomposites prepared from titania and renewable biomass-derived resources improved the photocatalytic performance of titania ascribe to various non-intuitive benefits for instance, an indirect enhancement in light harvesting (through N-doping), and improved selectivity via mediation (scavenging) of unselective reactive radical species.

5. CONCLUSIONS AND FUTURE PERSPECTIVE

Titania-based heterogeneous photocatalysis carried out under mild experimental conditions such as ambient pressure and temperature, utilizing oxygen (dissolved naturally in the reaction medium) as an oxidizing agent, and visible light as an irradiation source is a green and economical approach for the valorization of biomass-based platform chemicals. The results acquired during the course of the Ph.D. investigations implies that ligand-to-metal charge transfer (LMCT)-sensitization, and formation of nanocomposites of titania with chitosan-lignin (CL) can be successfully employed for the visible light activation of titania for the selective oxidation of biomass-derived platform chemicals. The formation of a LMCT-complex between a platform compound, 5-hydroxymethylfurfural (HMF) and titania via hydroxyl functional groups, can be employed as a suitable sensitization approach for harvesting and utilizing visible light. The LMCT-complex formation of HMF on titania extended the visible light absorption of titania up to 650 nm and enables the selective oxidation of HMF to diformylfuran (DFF). The specific surface area and number of OH groups on the titania surface are crucial factors affecting the formation and photoactivity of LMCT-complex. In particular, the visible light activity of LMCT-complex has increased with the specific surface area of the titania and increased number of OH groups on the surface, owing to the increased number of potential adsorptive sites for HMF. Moreover, valorization of biomass via LMCT-sensitization utilizing a substrate (HMF) is found to be a more sustainable and environmentally-benign approach than popular dye-sensitization, which requires dyes that are often unstable under light irradiation and costly. The current study evaluated the visible light activity of LMCT-complex formed between HMF and titania under green light (λ = 515 nm). However, the visible light absorption of LMCT-complex is extended up to the far visible region

(650 nm), which signifies the need for the investigation of LMCT-complex activity under red light. This could also be beneficial for the efficient utilization of solar radiation to advance solar-driven chemical conversion processes. Although, the selectivity of desired products is improved via LMCT-sensitization approach under visible light. However, the general photoactivity of LMCT-complexes in terms of conversion of biomass-derived substrate under visible light has not reached the activity of titania under UV light. Further investigation is required to improve the conversion of substrate without compromising the selectivity of target product. Various approaches could be employed for the process intensification such as using flow photoreactor, testing alternative irradiation sources (solar simulator), using different solvents etc. Besides that, there is a need to evaluate the LMCT-sensitization of other semiconductor nanoparticles. The current study and the majority of studies carried out in the past employ titania due to its abundant availability, nontoxic nature and stability to study the LMCT-sensitization. However, other semiconductors like Nb_2O_5 (upon modification with HMF[194] and amines[247]) and CeO_2 (upon modification with alcohols[248]) also showed the potential for LMCT-sensitization. Compared to titania these semiconductors are not explored to a substantial extent. Thus the results of this thesis open a new avenue for visible-light driven photocatalysis for organic reactions under mild and environmentally-benign conditions.

Furthermore, chitosan and lignin have tremendous potential for the preparation of composites with improved physicochemical properties. Coupling titania with chitosan-lignin (CL) formed a nanocomposite, which improved the visible light (λ = 515 nm) activity of titania for the selective oxidation of benzyl alcohol (BnOH) to benzaldehyde (Bnald). More precisely, 75T/CL(25:75) nanocomposite (a representative nanocomposite) exhibited excellent selectivity for Bnald (100%) at moderate BnOH conversion (19%). Lignin has not exhibited any photosensitizing effect for the visible

light activation of titania. Conversely, chitosan interaction with titania is critical for the visible light activity of titania, possibly by introduction of nitrogen into the titania framework. The present approach of utilizing biomass waste to improve the visible light (515 nm) activity of titania has the potential to significantly contribute to advance photocatalysis for biomass valorization and efficient utilization of solar energy. The current approach of nanocomposite formation utilizing widely available biomass material could be extended to improve the visible light activity of other wide band gap semiconducting materials like ZnO and NiO for their application in selective oxidation. In addition, further investigations are required to improve the conversion of BnOH under visible light and to utilize the far visible light region (red light) for the photocatalytic selective oxidation of BnOH. In this respect, the potential of chitosan and lignin for the preparation of metal free carbonaceous photocatalyst for its application in selective oxidation reactions can be evaluated. This could be a promising approach for biomass-valorization for material synthesis and chemical production.

REFERENCES

1 A. Fujishima and K. Honda, *Nature*, 1972, **238**, 37–38.

2 S. N. Frank and A. J. Bard, *J. Am. Chem. Soc.*, 1977, **99**, 303–304.

3 T. Inoue, A. Fujishima, S. Konishi and K. Honda, *Nature*, 1979, **277**, 637–638.

4 I. Izumi, F.-R. F. Fan and A. J. Bard, *J. Phys. Chem.*, 1981, **85**, 218–223.

5 P. Lisowski, J. C. Colmenares, O. Mašek, W. Lisowski, D. Lisovytskiy, A. Kamińska and D. Łomot, *ACS Sustain. Chem. Eng.*, 2017, **5**, 6274–6287.

6 U. I. Gaya and A. H. Abdullah, *J. Photochem. Photobiol. C Photochem. Rev.*, 2008, **9**, 1–12.

7 A. Naldoni, M. Altomare, G. Zoppellaro, N. Liu, Š. Kment, R. Zbořil and P. Schmuki, *ACS Catal.*, 2019, **9**, 345–364.

8 M. Pagliaro, G. Palmisano, R. Ciriminna and V. Loddo, *Energy Environ. Sci.*, 2009, **2**, 838.

9 L. Liu, H. Zhao, J. M. Andino and Y. Li, *ACS Catal.*, 2012, **2**, 1817–1828.

10 S. P. Pitre, T. P. Yoon and J. C. Scaiano, *Chem. Commun.*, 2017, **53**, 4335–4338.

11 S. Higashimoto, K. Okada, M. Azuma, H. Ohue, T. Terai and Y. Sakata, *RSC Adv.*, 2012, **2**, 669–676.

12 A. Khan, M. Goepel, A. Kubas, D. Łomot, W. Lisowski, D. Lisovytskiy, A. Nowicka, J. C. Colmenares and R. Gläser, *ChemSusChem*, 2021, **14**, 1351–1362.

13 C. B. Almquist and P. Biswas, *Appl. Catal. A Gen.*, 2001, **214**, 259–271.

14 X. Liu, G. Zhu, X. Wang, X. Yuan, T. Lin and F. Huang, *Adv. Energy Mater.*, 2016, **6**, 1600452.

15 X. Pan, M.-Q. Yang, X. Fu, N. Zhang and Y.-J. Xu, *Nanoscale*, 2013, **5**, 3601.

16 M. Zhang, T. Chen and Y. Wang, *RSC Adv.*, 2017, **7**, 52755–52761.

17 J.-G. Li, T. Ishigaki and X. Sun, *J. Phys. Chem. C*, 2007, **111**, 4969–4976.

18 F. Parrino, M. Bellardita, E. I. García-López, G. Marcì, V. Loddo and L. Palmisano, *ACS Catal.*, 2018, **8**, 11191–11225.

19 J. Zhang, P. Zhou, J. Liu and J. Yu, *Phys. Chem. Chem. Phys.*, 2014, **16**, 20382–20386.

20 V. Etacheri, C. Di Valentin, J. Schneider, D. Bahnemann and S. C. Pillai, *J. Photochem. Photobiol. C Photochem. Rev.*, 2015, **25**, 1–29.

21 S. Nishimoto, B. Ohtani, H. Kajiwara and T. Kagiya, *J. Chem. Soc. Faraday Trans. 1 Phys. Chem. Condens. Phases*, 1985, **81**, 61.

22 M. A. Fox and M. T. Dulay, *Chem. Rev.*, 1993, **93**, 341–357.

23 M. H. Samat, A. M. M. Ali, M. F. M. Taib, O. H. Hassan and M. Z. A. Yahya, *Results Phys.*, 2016, **6**, 891–896.

24 Z. Yang, B. Wang, H. Cui, H. An, Y. Pan and J. Zhai, *J. Phys. Chem. C*, 2015, **119**, 16905–16912.

25 S. Yurdakal, G. Palmisano, V. Loddo, V. Augugliaro and L. Palmisano, *J. Am. Chem. Soc.*, 2008, **130**, 1568–1569.

26 W. Zhao, S. Ma, J. Zhou and G. Xiang, *Chem. Commun.*, 2021, **57**, 500–503.

27 H. Lin, L. Li, M. Zhao, X. Huang, X. Chen, G. Li and R. Yu, *J. Am. Chem. Soc.*, 2012, **134**, 8328–8331.

28 B. Sun, G. Zhou, Y. Zhang, R. Liu and T. Li, *Chem. Eng. J.*, 2015, **264**, 125–133.

29 Z. He, Q. Cai, H. Fang, G. Situ, J. Qiu, S. Song and J. Chen, *J. Environ. Sci.*, 2013, **25**, 2460–2468.

30 M. Toyoda, *Appl. Catal. B Environ.*, 2004, **49**, 227–232.

31 Q. Guo, C. Zhou, Z. Ma and X. Yang, *Adv. Mater.*, 2019, **31**, 1901997.

32 X. Chen and S. S. Mao, *Chem. Rev.*, 2007, **107**, 2891–2959.

33 Y. Nosaka and A. Y. Nosaka, *Chem. Rev.*, 2017, **117**, 11302–11336.

34 S.-H. Li, S. Liu, J. C. Colmenares and Y.-J. Xu, *Green Chem.*, 2016, **18**, 594–607.

35 T. Daimon, T. Hirakawa, M. Kitazawa, J. Suetake and Y. Nosaka, *Appl. Catal. A Gen.*, 2008, **340**, 169–175.

36 K. T. Ranjit, I. Willner, S. H. Bossmann and A. M. Braun, *Environ. Sci. Technol.*, 2001, **35**, 1544–1549.

37 D. Friedmann, A. Hakki, H. Kim, W. Choi and D. Bahnemann, *Green Chem.*, 2016, **18**, 5391–5411.

38 M. R. Hoffmann, S. T. Martin, W. Choi and D. W. Bahnemann, *Chem. Rev.*, 1995, **95**, 69–96.

39 S. S. R. Dasary, J. Saloni, A. Fletcher, Y. Anjaneyulu and H. Yu, *Int. J. Environ. Res. Public Health*, 2010, **7**, 3987–4001.

40 A. Gautam, A. Kshirsagar, R. Biswas, S. Banerjee and P. K. Khanna, *RSC Adv.*, 2016, **6**, 2746–2759.

41 S. Belekbir, M. El Azzouzi, A. El Hamidi, L. Rodríguez-Lorenzo, J. A. Santaballa and M. Canle, *Nanomaterials*, 2020, **10**, 996.

42 S. Yurdakal, V. Loddo, V. Augugliaro, H. Berber, G. Palmisano and L. Palmisano, *Catal. Today*, 2007, **129**, 9–15.

43 I. Georgaki, E. Vasilaki and N. Katsarakis, *Am. J. Anal. Chem.*, 2014, **05**, 518–534.

44 S. Sreekantan, C. W. Lai and S. Mohd Zaki, *Int. J. Photoenergy*, 2014, **2014**, 1–7.

45 T. Mishra, J. Hait, N. Aman, R. K. Jana and S. Chakravarty, *J. Colloid Interface Sci.*, 2007, **316**, 80–84.

46 K. M. Joshi and V. S. Shrivastava, *Appl. Nanosci.*, 2011, **1**, 147–155.

47 M. E. Zorn, D. T. Tompkins, W. A. Zeltner and M. A. Anderson, *Environ. Sci. Technol.*, 2000, **34**, 5206–5210.

48 M. R. Nimlos, E. J. Wolfrum, M. L. Brewer, J. A. Fennell and G. Bintner, *Environ. Sci. Technol.*, 1996, **30**, 3102–3110.

49 A. Tawari, W.-D. Einicke and R. Gläser, *Catalysts*, 2016, **6**, 31.

50 S. W. Verbruggen, K. Masschaele, E. Moortgat, T. E. Korany, B. Hauchecorne, J. A. Martens and S. Lenaerts, *Catal. Sci. Technol.*, 2012, **2**, 2311.

51 B. O'Regan and M. Grätzel, *Nature*, 1991, **353**, 737–740.

52 K. Czelej, J. C. Colmenares, K. Jabłczyńska, K. Ćwieka, Ł. Werner and L. Gradoń, *Catal. Today*, , DOI:10.1016/j.cattod.2021.02.004.

53 Y. Bai, I. Mora-Seró, F. De Angelis, J. Bisquert and P. Wang, *Chem. Rev.*, 2014, **114**, 10095–10130.

54 Y. Zhang, Z. Jiang, J. Huang, L. Y. Lim, W. Li, J. Deng, D. Gong, Y. Tang, Y. Lai and Z. Chen, *RSC Adv.*, 2015, **5**, 79479–79510.

55 A. Yella, H.-W. Lee, H. N. Tsao, C. Yi, A. K. Chandiran, M. K. Nazeeruddin, E. W.-G. Diau, C.-Y. Yeh, S. M. Zakeeruddin and M. Gratzel, *Science (80-.).*, 2011, **334**, 629–634.

56 A. A. Melvin, K. Illath, T. Das, T. Raja, S. Bhattacharyya and C. S. Gopinath, *Nanoscale*, 2015, **7**, 13477–13488.

57 T. Liu, W. Chen, T. Huang, G. Duan, X. Yang and X. Liu, *J. Mater. Sci.*, 2016, **51**, 6987–6997.

58 R. Su, R. Tiruvalam, A. J. Logsdail, Q. He, C. A. Downing, M. T. Jensen, N. Dimitratos, L. Kesavan, P. P. Wells, R. Bechstein, H. H. Jensen, S. Wendt, C. R. A. Catlow, C. J. Kiely, G. J. Hutchings and F. Besenbacher, *ACS Nano*, 2014, **8**, 3490–3497.

59 A. S. Hainer, J. S. Hodgins, V. Sandre, M. Vallieres, A. E. Lanterna and J. C. Scaiano, *ACS Energy Lett.*, 2018, **3**, 542–545.

60 W.-T. Chen, A. Chan, Z. H. N. Al-Azri, A. G. Dosado, M. A. Nadeem, D. Sun-Waterhouse, H. Idriss and G. I. N. Waterhouse, *J. Catal.*, 2015, **329**, 499–513.

61 S. O. Flores, O. Rios-Bernij, M. A. Valenzuela, I. Córdova, R. Gómez and R. Gutiérrez, *Top. Catal.*, 2007, **44**, 507–511.

62 S. Kodama and S. Yagi, *J. Phys. Chem.*, 1989, **93**, 4556–4561.

63 B. Hauchecorne, D. Terrens, S. Verbruggen, J. A. Martens, H. Van Langenhove, K. Demeestere and S. Lenaerts, *Appl. Catal. B Environ.*, 2011,

106, 630–638.

64 C. Huang, D. H. Chen and K. Li, *Chem. Eng. Commun.*, 2003, **190**, 373–392.

65 W. Zhang, Z. Yuan, L. Huang, J. Kang, R. Jiang and H. Zhong, *Sci. Rep.*, 2016, **6**, 20981.

66 S. Challagulla, K. Tarafder, R. Ganesan and S. Roy, *Sci. Rep.*, 2017, **7**, 8783.

67 J. L. Ferry and W. H. Glaze, *Langmuir*, 1998, **14**, 3551–3555.

68 K. Imamura, S. Iwasaki, T. Maeda, K. Hashimoto, B. Ohtani and H. Kominami, *Phys. Chem. Chem. Phys.*, 2011, **13**, 5114.

69 C. Joyce-Pruden, J. K. Pross and Y. Li, *J. Org. Chem.*, 1992, **57**, 5087–5091.

70 S. Kohtani, E. Yoshioka, K. Saito, A. Kudo and H. Miyabe, *Catal. Commun.*, 2010, **11**, 1049–1053.

71 H. Hao, L. Zhang, W. Wang and S. Zeng, *Catal. Sci. Technol.*, 2018, **8**, 1229–1250.

72 J. Dai, J. Yang, X. Wang, L. Zhang and Y. Li, *Appl. Surf. Sci.*, 2015, **349**, 343–352.

73 D. Balcells, E. Clot and O. Eisenstein, *Chem. Rev.*, 2010, **110**, 749–823.

74 F.-L. Cao, J.-G. Wang, F.-J. Lv, D.-Q. Zhang, Y.-N. Huo, G.-S. Li, H.-X. Li and J. Zhu, *Catal. Commun.*, 2011, **12**, 946–950.

75 J. Tripathy, K. Lee and P. Schmuki, *Angew. Chemie Int. Ed.*, 2014, n/a-n/a.

76 M. Nishikawa, Y. Mitani and Y. Nosaka, *J. Phys. Chem. C*, 2012, **116**, 14900–14907.

77 S. Yurdakal, V. Augugliaro, J. Sanz, J. Soria, I. Sobrados and M. J. Torralvo, *J. Catal.*, 2014, **309**, 97–104.

78 Q. Wang, M. Zhang, C. Chen, W. Ma and J. Zhao, *Angew. Chemie Int. Ed.*, 2010, **49**, 7976–7979.

79 W. R. Leow, W. K. H. Ng, T. Peng, X. Liu, B. Li, W. Shi, Y. Lum, X. Wang, X. Lang, S. Li, N. Mathews, J. W. Ager, T. C. Sum, H. Hirao and X. Chen, *J. Am. Chem. Soc.*, 2017, **139**, 269–276.

80 J. Wang, P. Rao, W. An, J. Xu and Y. Men, *Appl. Catal. B Environ.*, 2016, **195**, 141–148.

81 A. Di Paola, M. Bellardita, L. Palmisano, Z. Barbieriková and V. Brezová, *J. Photochem. Photobiol. A Chem.*, 2014, **273**, 59–67.

82 S. Yurdakal and V. Augugliaro, *RSC Adv.*, 2012, **2**, 8375.

83 A. Molinari, M. Montoncello, H. Rezala and A. Maldotti, *Photochem. Photobiol. Sci.*, 2009, **8**, 613.

84 M. Zhang, Q. Wang, C. Chen, L. Zang, W. Ma and J. Zhao, *Angew. Chemie Int. Ed.*, 2009, **48**, 6081–6084.

85 G. Zhang, G. Kim and W. Choi, *Energy Environ. Sci.*, 2014, **7**, 954.

86 V. Parvulescu, M. Ciobanu and G. Petcu, in *Handbook of Smart Photocatalytic Materials*, Elsevier, 2020, pp. 103–140.

87 L. G. Devi and R. Kavitha, *Appl. Catal. B Environ.*, 2013, **140**–**141**, 559–587.

88 C. W. H. Dunnill, Z. A. Aiken, J. Pratten, M. Wilson, D. J. Morgan and I. P. Parkin, *J. Photochem. Photobiol. A Chem.*, 2009, **207**, 244–253.

89 R. Asahi, *Science (80-.).*, 2001, **293**, 269–271.

90 H. Irie, Y. Watanabe and K. Hashimoto, *J. Phys. Chem. B*, 2003, **107**, 5483–5486.

91 T. Ihara, *Appl. Catal. B Environ.*, 2003, **42**, 403–409.

92 G. Liu, L. Wang, H. G. Yang, H.-M. Cheng and G. Q. (Max) Lu, *J. Mater. Chem.*, 2010, **20**, 831–843.

93 X. Li, X. Chen, H. Niu, X. Han, T. Zhang, J. Liu, H. Lin and F. Qu, *J. Colloid Interface Sci.*, 2015, **452**, 89–97.

94 H. Kim, J. Kim, W. Kim and W. Choi, *J. Phys. Chem. C*, 2011, **115**, 9797–9805.

95 P. Chowdhury, J. Moreira, H. Gomaa and A. K. Ray, *Ind. Eng. Chem. Res.*, 2012, **51**, 4523–4532.

96 J. Diaz-Angulo, I. Gomez-Bonilla, C. Jimenez-Tohapanta, M. Mueses, M.

Pinzon and F. Machuca-Martinez, *Photochem. Photobiol. Sci.*, 2019, **18**, 897–904.

97 J.-P. Zou, Y. Chen, M. Zhu, D. Wang, X.-B. Luo and S.-L. Luo, in *Nanomaterials for the Removal of Pollutants and Resource Reutilization*, Elsevier, 2019, pp. 25–58.

98 T. Hannappel, B. Burfeindt, W. Storck and F. Willig, *J. Phys. Chem. B*, 1997, **101**, 6799–6802.

99 Y.-P. Yuan, L.-S. Yin, S.-W. Cao, G.-S. Xu, C.-H. Li and C. Xue, *Appl. Catal. B Environ.*, 2015, **168**–**169**, 572–576.

100 R. Abe, K. Sayama and H. Arakawa, *J. Photochem. Photobiol. A Chem.*, 2004, **166**, 115–122.

101 T. Peng and J. Xu, *Optik (Stuttg).*, 2020, **207**, 164407.

102 G. Kim and W. Choi, *Appl. Catal. B Environ.*, 2010, **100**, 77–83.

103 T. Rajh, L. X. Chen, K. Lukas, T. Liu, M. C. Thurnauer and D. M. Tiede, *J. Phys. Chem. B*, 2002, **106**, 10543–10552.

104 Y. Wang, K. Hang, N. A. Anderson and T. Lian, *J. Phys. Chem. B*, 2003, **107**, 9434–9440.

105 L.-M. Liu, S.-C. Li, H. Cheng, U. Diebold and A. Selloni, *J. Am. Chem. Soc.*, 2011, **133**, 7816–7823.

106 J.-L. Shi, H. Hao, X. Li and X. Lang, *Catal. Sci. Technol.*, 2018, **8**, 3910–3917.

107 S. Higashimoto, N. Suetsugu, M. Azuma, H. Ohue and Y. Sakata, *J. Catal.*, 2010, **274**, 76–83.

108 Y. F. Rao and W. Chu, *Environ. Sci. Technol.*, 2009, **43**, 6183–6189.

109 H. Wang, Y. Song, J. Xiong, J. Bi, L. Li, Y. Yu, S. Liang and L. Wu, *Appl. Catal. B Environ.*, 2018, **224**, 394–403.

110 S. Bagheri, N. Muhd Julkapli and S. Bee Abd Hamid, *Int. J. Photoenergy*, 2015, **2015**, 1–30.

111 M. Dahl, Y. Liu and Y. Yin, *Chem. Rev.*, 2014, **114**, 9853–9889.

112 J. Virkutyte, V. Jegatheesan and R. S. Varma, *Bioresour. Technol.*, 2012, **113**, 288–293.

113 W. Ren, Z. Ai, F. Jia, L. Zhang, X. Fan and Z. Zou, *Appl. Catal. B Environ.*, 2007, **69**, 138–144.

114 J. C. Colmenares, R. S. Varma and P. Lisowski, *Green Chem.*, 2016, **18**, 5736–5750.

115 X. Wang, Y. Liu, Z. Hu, Y. Chen, W. Liu and G. Zhao, *J. Hazard. Mater.*, 2009, **169**, 1061–1067.

116 N. M. Mahmoodi, M. Arami and J. Zhang, *J. Alloys Compd.*, 2011, **509**, 4754–4764.

117 H. Slimen, A. Houas and J. P. Nogier, *J. Photochem. Photobiol. A Chem.*, 2011, **221**, 13–21.

118 X. Wang, Z. Hu, Y. Chen, G. Zhao, Y. Liu and Z. Wen, *Appl. Surf. Sci.*, 2009, **255**, 3953–3958.

119 K. E. Tettey, M. Q. Yee and D. Lee, *ACS Appl. Mater. Interfaces*, 2010, **2**, 2646–2652.

120 K. Woan, G. Pyrgiotakis and W. Sigmund, *Adv. Mater.*, 2009, **21**, 2233–2239.

121 W. Wang, P. Serp, P. Kalck and J. L. Faria, *J. Mol. Catal. A Chem.*, 2005, **235**, 194–199.

122 C. Lettmann, K. Hildenbrand, H. Kisch, W. Macyk and W. F. Maier, *Appl. Catal. B Environ.*, 2001, **32**, 215–227.

123 A. Khan, V. Nair, J. C. Colmenares and R. Gläser, *Top. Curr. Chem.*, 2018, **376**, 20.

124 P. Lisowski, J. C. Colmenares, O. Mašek, W. Lisowski, D. Lisovytskiy, A. Kamińska and D. Łomot, *ACS Sustain. Chem. Eng.*, 2019, **7**, 16933–16934.

125 F. D. Bobbink, J. Zhang, Y. Pierson, X. Chen and N. Yan, *Green Chem.*, 2015, **17**, 1024–1031.

126 A. Khan, M. Goepel, J. C. Colmenares and R. Gläser, *ACS Sustain. Chem. Eng.*, 2020, **8**, 4708–4727.

127 M. H. Farzana and S. Meenakshi, *Ind. Eng. Chem. Res.*, 2014, **53**, 55–63.

128 X.-M. Yan, J. Kang, L. Gao, L. Xiong and P. Mei, *Appl. Surf. Sci.*, 2013, **265**, 778–783.

129 G. Chatel, K. De Oliveira Vigier and F. Jérôme, *ChemSusChem*, 2014, **7**, 2774–2787.

130 H. V. Lee, S. B. A. Hamid and S. K. Zain, *Sci. World J.*, 2014, **2014**, 1–20.

131 X. Chen, D.-H. Kuo, D. Lu, Y. Hou and Y.-R. Kuo, *Microporous Mesoporous Mater.*, 2016, **223**, 145–151.

132 Y. Li and N. Hong, *J. Mater. Chem. A*, 2015, **3**, 21537–21544.

133 Y. Wu, J. Wang, X. Qiu, R. Yang, H. Lou, X. Bao and Y. Li, *ACS Appl. Mater. Interfaces*, 2016, **8**, 12377–12383.

134 J. C. Dean, P. Navotnaya, A. P. Parobek, R. M. Clayton and T. S. Zwier, *J. Chem. Phys.*, 2013, **139**, 144313.

135 N. Li, Y. Chen, H. Yu, F. Xiong, W. Yu, M. Bao, Z. Wu, C. Huang, F. Rao, J. Li and Y. Bao, *RSC Adv.*, 2017, **7**, 20760–20765.

136 A. Cogulet, P. Blanchet and V. Landry, *J. Photochem. Photobiol. B Biol.*, 2016, **158**, 184–191.

137 G. Marchand, C. A. Calliste, R. M. Williams, C. McLure, S. Leroy-Lhez and N. Villandier, *ChemistrySelect*, 2018, **3**, 5512–5516.

138 L. Chen, C. Tang, N. Ning, C. Wang, Q. Fu and Q. Zhang, *Chinese J. Polym. Sci.*, 2009, **27**, 739.

139 T. Wang, M. Turhan and S. Gunasekaran, *Polym. Int.*, 2004, **53**, 911–918.

140 H. Orelma, I. Filpponen, L.-S. Johansson, J. Laine and O. J. Rojas, *Biomacromolecules*, 2011, **12**, 4311–4318.

141 M. Schreiber, S. Vivekanandhan, P. Cooke, A. K. Mohanty and M. Misra, *J. Mater. Sci.*, 2014, **49**, 7949–7958.

142 S. Kim, M. M. Fernandes, T. Matamá, A. Loureiro, A. C. Gomes and A. Cavaco-Paulo, *Colloids Surfaces B Biointerfaces*, 2013, **103**, 1–8.

143 K. Crouvisier-Urion, P. R. Bodart, P. Winckler, J. Raya, R. D. Gougeon, P. Cayot, S. Domenek, F. Debeaufort and T. Karbowiak, *ACS Sustain. Chem. Eng.*, 2016, **4**, 6371–6381.

144 E. Rosova, N. Smirnova, E. Dresvyanina, V. Smirnova, E. Vlasova, E. Ivan'kova, M. Sokolova, T. Maslennikova, K. Malafeev, K. Kolbe, M. Kanerva and V. Yudin, *Cosmetics*, 2021, **8**, 24.

145 S. T. Yoganandham, G. Sathyamoorthy and R. R. Renuka, in *Sustainable Seaweed Technologies*, Elsevier, 2020, pp. 191–205.

146 T. M. Masilompane, N. Chaukura, S. B. Mishra and A. K. Mishra, *Int. J. Biol. Macromol.*, 2018, **120**, 1659–1666.

147 C. Han, M.-Q. Yang, B. Weng and Y.-J. Xu, *Phys. Chem. Chem. Phys.*, 2014, **16**, 16891.

148 A. C. Martins, A. L. Cazetta, O. Pezoti, J. R. B. Souza, T. Zhang, E. J. Pilau, T. Asefa and V. C. Almeida, *Ceram. Int.*, 2017, **43**, 4411–4418.

149 W. Wang, P. Serp, P. Kalck and J. L. Faria, *Appl. Catal. B Environ.*, 2005, **56**, 305–312.

150 E. Pabón, J. Retuert, R. Quijada and A. Zarate, *Microporous Mesoporous Mater.*, 2004, **67**, 195–203.

151 T. Tsubota, A. Ono, N. Murakami and T. Ohno, *Appl. Catal. B Environ.*, 2009, **91**, 533–538.

152 Z. Li, B. Hou, Y. Xu, D. Wu, Y. Sun, W. Hu and F. Deng, *J. Solid State Chem.*, 2005, **178**, 1395–1405.

153 K. Mao, X. Wu, X. Min, Z. Huang, Y. Liu and M. Fang, *Sci. Rep.*, 2019, **9**, 16321.

154 C.-C. Tsai and H. Teng, *Chem. Mater.*, 2004, **16**, 4352–4358.

155 J.-N. Nian and H. Teng, *J. Phys. Chem. B*, 2006, **110**, 4193–4198.

156 Q. Xiang, J. Yu and M. Jaroniec, *Nanoscale*, 2011, **3**, 3670.

157 Y. V Kolen'ko, V. D. Maximov, A. V Garshev, P. E. Meskin, N. N. Oleynikov and B. R. Churagulov, *Chem. Phys. Lett.*, 2004, **388**, 411–415.

158 Y. V. Kolen'ko, B. R. Churagulov, M. Kunst, L. Mazerolles and C. Colbeau-Justin, *Appl. Catal. B Environ.*, 2004, **54**, 51–58.

159 A. Corma, S. Iborra and A. Velty, *Chem. Rev.*, 2007, **107**, 2411–2502.

160 S. De, S. Dutta and B. Saha, *Catal. Sci. Technol.*, 2016, **6**, 7364–7385.

161 L. Li, J. S. Rowbotham, H. Christopher Greenwell and P. W. Dyer, in *New and Future Developments in Catalysis*, Elsevier, 2013, pp. 173–208.

162 S. K. Hanson and R. T. Baker, *Acc. Chem. Res.*, 2015, **48**, 2037–2048.

163 J. Zakzeski, P. C. A. Bruijnincx, A. L. Jongerius and B. M. Weckhuysen, *Chem. Rev.*, 2010, **110**, 3552–3599.

164 G. Han, T. Yan, W. Zhang, Y. C. Zhang, D. Y. Lee, Z. Cao and Y. Sun, *ACS Catal.*, 2019, **9**, 11341–11349.

165 P. J. Deuss, K. Barta and J. G. de Vries, *Catal. Sci. Technol.*, 2014, **4**, 1174–1196.

166 M. Kabbour and R. Luque, in *Biomass, Biofuels, Biochemicals*, Elsevier, 2020, pp. 283–297.

167 H. Chang, I. Bajaj, A. H. Motagamwala, A. Somasundaram, G. W. Huber, C. T. Maravelias and J. A. Dumesic, *Green Chem.*, 2021, **23**, 3277–3288.

168 M. J. Climent, A. Corma and S. Iborra, *Green Chem.*, 2011, **13**, 520.

169 V. Choudhary, S. H. Mushrif, C. Ho, A. Anderko, V. Nikolakis, N. S. Marinkovic, A. I. Frenkel, S. I. Sandler and D. G. Vlachos, *J. Am. Chem. Soc.*, 2013, **135**, 3997–4006.

170 F. Salak Asghari and H. Yoshida, *Ind. Eng. Chem. Res.*, 2006, **45**, 2163–2173.

171 H. Xia, S. Xu, H. Hu, J. An and C. Li, *RSC Adv.*, 2018, **8**, 30875–30886.

172 X. Li and Y. Zhang, *Green Chem.*, 2016, **18**, 643–647.

173 J. Lan, J. Lin, Z. Chen and G. Yin, *ACS Catal.*, 2015, **5**, 2035–2041.

174 D. Zhao, D. Rodriguez-Padron, R. Luque and C. Len, *ACS Sustain. Chem. Eng.*, 2020, **8**, 8486–8495.

175 B. Xiao, M. Zheng, X. Li, J. Pang, R. Sun, H. Wang, X. Pang, A. Wang, X.

Wang and T. Zhang, *Green Chem.*, 2016, **18**, 2175–2184.

176 M. Ventura, A. Dibenedetto and M. Aresta, *Inorganica Chim. Acta*, 2018, **470**, 11–21.

177 H. Ait Rass, N. Essayem and M. Besson, *ChemSusChem*, 2015, **8**, 1206–1217.

178 H. G. Cha and K.-S. Choi, *Nat. Chem.*, 2015, **7**, 328–333.

179 P. Pal and S. Saravanamurugan, *ChemSusChem*, 2019, **12**, 145–163.

180 A. Gandini, A. J. D. Silvestre, C. P. Neto, A. F. Sousa and M. Gomes, *J. Polym. Sci. Part A Polym. Chem.*, 2009, **47**, 295–298.

181 E. de Jong, M. A. Dam, L. Sipos and G.-J. M. Gruter, 2012, pp. 1–13.

182 Alex Scott, *C&EN Glob. Enterp.*, 2016, **94**, cen-09412-notw12.

183 D. Zhao, D. Rodriguez-Padron, K. S. Triantafyllidis, Y. Wang, R. Luque and C. Len, *ACS Sustain. Chem. Eng.*, 2020, **8**, 3091–3102.

184 Z. Zhang and K. Deng, *ACS Catal.*, 2015, **5**, 6529–6544.

185 S. Xu, P. Zhou, Z. Zhang, C. Yang, B. Zhang, K. Deng, S. Bottle and H. Zhu, *J. Am. Chem. Soc.*, 2017, **139**, 14775–14782.

186 R. Fang, R. Luque and Y. Li, *Green Chem.*, 2017, **19**, 647–655.

187 D. Baruah, F. L. Hussain, M. Suri, U. P. Saikia, P. Sengupta, D. K. Dutta and D. Konwar, *Catal. Commun.*, 2016, **77**, 9–12.

188 S. Biswas, B. Dutta, A. Mannodi-Kanakkithodi, R. Clarke, W. Song, R. Ramprasad and S. L. Suib, *Chem. Commun.*, 2017, **53**, 11751–11754.

189 D. A. Giannakoudakis, V. Nair, A. Khan, E. A. Deliyanni, J. C. Colmenares and K. S. Triantafyllidis, *Appl. Catal. B Environ.*, 2019, **256**, 117803.

190 H. Zhang, Z. Feng, Y. Zhu, Y. Wu and T. Wu, *J. Photochem. Photobiol. A Chem.*, 2019, **371**, 1–9.

191 L. Chen, W. Yang, Z. Gui, S. Saravanamurugan, A. Riisager, W. Cao and Z. Qi, *Catal. Today*, 2019, **319**, 105–112.

192 I. Krivtsov, E. I. García-López, G. Marcì, L. Palmisano, Z. Amghouz, J. R. García, S. Ordóñez and E. Díaz, *Appl. Catal. B Environ.*, 2017, **204**, 430–439.

193 Q. Wu, Y. He, H. Zhang, Z. Feng, Y. Wu and T. Wu, *Mol. Catal.*, 2017, **436**, 10–18.

194 H. Zhang, Q. Wu, C. Guo, Y. Wu and T. Wu, *ACS Sustain. Chem. Eng.*, 2017, **5**, 3517–3523.

195 C. M. Crombie, R. J. Lewis, R. L. Taylor, D. J. Morgan, T. E. Davies, A. Folli, D. M. Murphy, J. K. Edwards, J. Qi, H. Jiang, C. J. Kiely, X. Liu, M. S. Skjøth-Rasmussen and G. J. Hutchings, *ACS Catal.*, 2021, **11**, 2701–2714.

196 C. Della Pina, E. Falletta and M. Rossi, *J. Catal.*, 2008, **260**, 384–386.

197 J. C. Colmenares, W. Ouyang, M. Ojeda, E. Kuna, O. Chernyayeva, D. Lisovytskiy, S. De, R. Luque and A. M. Balu, *Appl. Catal. B Environ.*, 2016, **183**, 107–112.

198 L. Palmisano, V. Augugliaro, M. Bellardita, A. Di Paola, E. García López, V. Loddo, G. Marcì, G. Palmisano and S. Yurdakal, *ChemSusChem*, 2011, **4**, 1431–1438.

199 A. Magdziarz, J. C. Colmenares, O. Chernyayeva, K. Kurzydłowski and J. Grzonka, *ChemCatChem*, 2016, **8**, 536–539.

200 Z. Zhang, Z. Luo, Z. Yang, S. Zhang, Y. Zhang, Y. Zhou, X. Wang and X. Fu, *RSC Adv.*, 2013, **3**, 7215.

201 Z. Zhang, X. Wang, J. Long, Q. Gu, Z. Ding and X. Fu, *J. Catal.*, 2010, **276**, 201–214.

202 A. Tanaka, K. Hashimoto and H. Kominami, *Chem. Commun.*, 2017, **53**, 4759–4762.

203 S. Yurdakal, B. S. Tek, O. Alagöz, V. Augugliaro, V. Loddo, G. Palmisano and L. Palmisano, *ACS Sustain. Chem. Eng.*, 2013, **1**, 456–461.

204 C. Sievers, Y. Noda, L. Qi, E. M. Albuquerque, R. M. Rioux and S. L. Scott, *ACS Catal.*, 2016, **6**, 8286–8307.

205 S. Higashimoto, N. Kitao, N. Yoshida, T. Sakura, M. Azuma, H. Ohue and Y. Sakata, *J. Catal.*, 2009, **266**, 279–285.

206 V. Augugliaro, T. Caronna, V. Loddo, G. Marcì, G. Palmisano, L. Palmisano

and S. Yurdakal, *Chem. - A Eur. J.*, 2008, **14**, 4640–4646.

207 L. Xiong and J. Tang, *Adv. Energy Mater.*, 2021, **11**, 2003216.

208 J. Yu, G. Dai and B. Cheng, *J. Phys. Chem. C*, 2010, **114**, 19378–19385.

209 J. S. Park and W. Choi, *Langmuir*, 2004, **20**, 11523–11527.

210 A. Spyrogianni, I. K. Herrmann, K. Keevend, S. E. Pratsinis and K. Wegner, *J. Colloid Interface Sci.*, 2017, **507**, 95–106.

211 R. Mueller, H. K. Kammler, K. Wegner and S. E. Pratsinis, *Langmuir*, 2003, **19**, 160–165.

212 A. K. Kharade and S. Chang, *J. Phys. Chem. C*, 2020, **124**, 10981–10992.

213 F. F. Marafatto, M. L. Strader, J. Gonzalez-Holguera, A. Schwartzberg, B. Gilbert and J. Peña, *Proc. Natl. Acad. Sci.*, 2015, **112**, 4600–4605.

214 *Proc. R. Soc. London. Ser. A. Math. Phys. Sci.*, 1956, **235**, 518–536.

215 Q. Yang, S. O. Pehkonen and M. B. Ray, *Ind. Eng. Chem. Res.*, 2005, **44**, 3471–3479.

216 S. P. Pitre, C. D. McTiernan, W. Vine, R. DiPucchio, M. Grenier and J. C. Scaiano, *Sci. Rep.*, 2015, **5**, 16397.

217 M. Wu, Y. Gong, T. Nie, J. Zhang, R. Wang, H. Wang and B. He, *J. Mater. Chem. A*, 2019, **7**, 5324–5332.

218 X. Jiang, M. Manawan, T. Feng, R. Qian, T. Zhao, G. Zhou, F. Kong, Q. Wang, S. Dai and J. H. Pan, *Catal. Today*, 2018, **300**, 12–17.

219 M. Zhao, L. Li, H. Lin, L. Yang and G. Li, *Chem. Commun.*, 2013, **49**, 7046.

220 M. Thommes, *Chemie Ing. Tech.*, 2010, **82**, 1059–1073.

221 T. Huyen, T. Chi, N. Dung, H. Kosslick and N. Liem, *Nanomaterials*, 2018, **8**, 276.

222 C.-Y. Wu, K.-J. Tu, J.-P. Deng, Y.-S. Lo and C.-H. Wu, *Materials (Basel).*, 2017, **10**, 566.

223 J. Guo, X. Cai, Y. Li, R. Zhai, S. Zhou and P. Na, *Chem. Eng. J.*, 2013, **221**, 342–352.

224 D. Zhao, C. Chen, Y. Wang, H. Ji, W. Ma, L. Zang and J. Zhao, *J. Phys. Chem. C*, 2008, **112**, 5993–6001.

225 G. Tsilomelekis, T. R. Josephson, V. Nikolakis and S. Caratzoulas, *ChemSusChem*, 2014, **7**, 117–126.

226 T. Kim, R. S. Assary, L. A. Curtiss, C. L. Marshall and P. C. Stair, *J. Raman Spectrosc.*, 2011, **42**, 2069–2076.

227 T. Kim, R. S. Assary, C. L. Marshall, D. J. Gosztola, L. A. Curtiss and P. C. Stair, *Chem. Phys. Lett.*, 2012, **531**, 210–215.

228 S. Sahoo, A. K. Arora and V. Sridharan, *J. Phys. Chem. C*, 2009, **113**, 16927–16933.

229 G. A. Tompsett, G. A. Bowmaker, R. P. Cooney, J. B. Metson, K. A. Rodgers and J. M. Seakins, *J. Raman Spectrosc.*, 1995, **26**, 57–62.

230 B. Bharti, S. Kumar, H.-N. Lee and R. Kumar, *Sci. Rep.*, 2016, **6**, 32355.

231 B. Ohtani, *Chem. Lett.*, 2008, **37**, 216–229.

232 B. Ohtani, *Front. Chem.*, 2017, **5,** 1-3.

233 M. Melchionna and P. Fornasiero, *ACS Catal.*, 2020, **10**, 5493–5501.

234 S. E. Braslavsky, A. M. Braun, A. E. Cassano, A. V. Emeline, M. I. Litter, L. Palmisano, V. N. Parmon and N. Serpone, *Pure Appl. Chem.*, 2011, **83**, 931–1014.

235 Y. Xu, S. Wu, P. Wan, J. Sun and Z. D. Hood, *RSC Adv.*, 2017, **7**, 32461–32467.

236 M. Pisarek, M. Krawczyk, M. Hołdyński and W. Lisowski, *ACS Omega*, 2020, **5**, 8647–8658.

237 J. B. Yoo, H. J. Yoo, H. J. Jung, H. S. Kim, S. Bang, J. Choi, H. Suh, J.-H. Lee, J.-G. Kim and N. H. Hur, *J. Mater. Chem. A*, 2016, **4**, 869–876.

238 Y. Chen, W. Li, J. Wang, Q. Yang, Q. Hou and M. Ju, *RSC Adv.*, 2016, **6**, 70352–70363.

239 Y. Murakami, K. Endo, I. Ohta, A. Y. Nosaka and Y. Nosaka, *J. Phys. Chem.*

C, 2007, **111**, 11339–11346.

240 J. C. Colmenares and R. Luque, *Chem. Soc. Rev.*, 2014, **43**, 765–778.

241 Y. Li, D. Yang, S. Lu, X. Qiu, Y. Qian and P. Li, *ACS Sustain. Chem. Eng.*, 2019, **7**, 6234–6242.

242 J. Yu, L. Li, Y. Qian, H. Lou, D. Yang and X. Qiu, *Ind. Eng. Chem. Res.*, 2018, **57**, 15740–15748.

243 S. A. Ansari, M. M. Khan, M. O. Ansari and M. H. Cho, *New J. Chem.*, 2016, **40**, 3000–3009.

244 C. W. Dunnill and I. P. Parkin, *Dalt. Trans.*, 2011, **40**, 1635–1640.

245 P. Verma, K. Mori, Y. Kuwahara, S. J. Cho and H. Yamashita, *Catal. Today*, 2020, **352**, 255–261.

246 S. Higashimoto, Y. Tanaka, R. Ishikawa, S. Hasegawa, M. Azuma, H. Ohue and Y. Sakata, *Catal. Sci. Technol.*, 2013, **3**, 400–403.

247 S. Furukawa, Y. Ohno, T. Shishido, K. Teramura and T. Tanaka, *J. Phys. Chem. C*, 2013, **117**, 442–450.

248 R. Zhao and L. Shi, *Org. Chem. Front.*, 2018, **5**, 3018–3021.

APPENDIX

A1. Optimization of hydrothermal treatment temperature and duration for the synthesis of SGH-TiO_2

The X-ray diffraction pattern of titania synthesized through sol-gel technique and hydrothermal method at different temperature (125 ºC, 150 ºC and 175 ºC) and time duration (4 hours, 8 hours and 16 hours) has been recorded (Figure A1). All the titania samples exhibited almost identical XRD patterns differing only in terms of the intensity of the XRD reflections. The reflexes observed in X-ray diffraction pattern of titania samples at 25.4º, 37.9 º, 48.1 º, 54.6º, 63.0 º showed the presence of anatase. In addition to anatase, reflex for brookite was found at 30.6 º. The XRD pattern of 50TCL(25:75) nanocomposite showed only reflexes from anatase phase and these are comparatively broader and less intense than the reflexes observed in pristine titania samples.

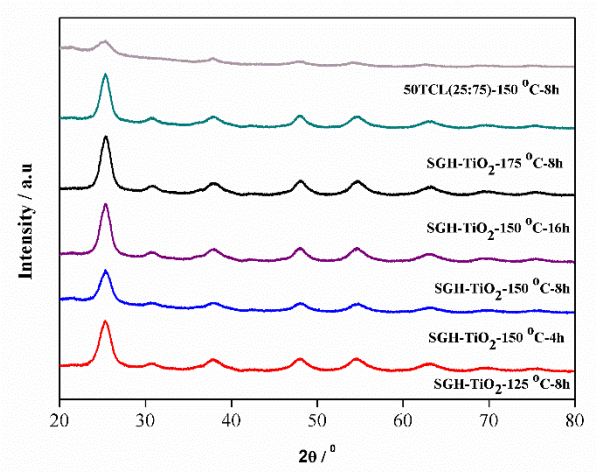

Figure A1. XRD patterns of SGH-TiO_2 and 50T/CL(25:75) nanocomposite prepared through sol-gel and hydrothermal method.

Interestingly, the intensity of the reflexes has not affected with varying the temperature (125 ºC, 150 ºC and 175 ºC). However, the intensity of the reflexes slightly increased with increasing duration of hydrothermal treatment from 4 hours to 8 hours. Whereas,

further increase in duration of hydrothermal treatment from 8 hours to 16 hours would not affect the intensity of reflexes. The average crystallite size (Table A1) of pristine titania samples and 50T/CL(25:75) nanocomposite was quite similar, in the range of 5-7 nm. The 8 hours of hydrothermal treatment at 150 ^{O}C showed crystalline phases of titania in 50T/CL(25:75) therefore, 8 hours of hydrothermal treatment at 150 ^{O}C was selected for the preparation of other nanocomposites.

Table A1. Crystallite sizes of SGH-TiO_2 and 50T/CL(25:75) nanocomposite.

Entries	Sample	Crystallite size (nm)
1	SGH-TiO_2-125 ^{O}C-8-h	5
2	SGH-TiO_2-150^{O}C-4-h	6
3	SGH-TiO_2-150^{O}C-8-h	6
4	SGH-TiO_2-150^{O}C-16-h	6
5	SGH-TiO_2-175^{O}C-8-h	7
6	50T/CL(25:75)-150^{O}C-8-h	6

A2. Optimization of HMF initial concentration for the photocatalytic selective oxidation over SGH-TiO_2 under visible light

In order to optimize the initial concentration of HMF, the photocatalytic selective oxidation experiments were carried out using different initial concentration (0.5mM, 1mM and 2 mM) of HMF (Figure A2). At lower (0.5mM) initial concentration of HMF, high HMF conversion (82%) was achieved with high DFF selectivity (76%) after 4 hours of illumination. Whereas, at higher initial HMF concentration (2mM) very low HMF conversion (16%) was achieved with excellent DFF selectivity (100%) after 4 hours of illumination. While, at 1mM initial HMF concentration moderate HMF conversion (59%) was achieved with reasonably high DFF selectivity (87%) after 4

hours of illumination. Therefore, 1mM initial HMF concentration was selected for the detailed photocatalytic selective oxidation study.

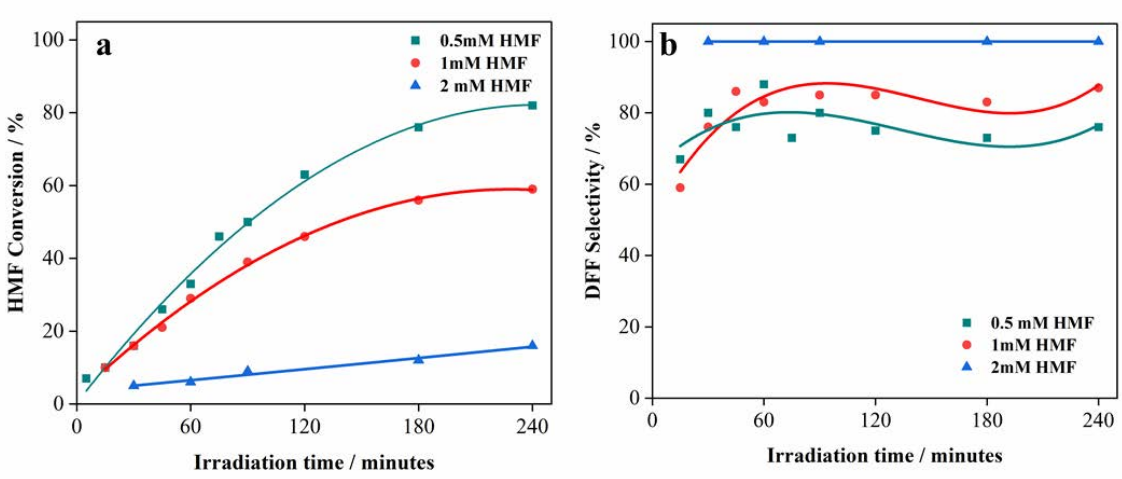

Figure A2 a) HMF conversion and b) DFF selectivity profile in the photocatalytic selective oxidation of HMF under visible light (λ = 515 nm), using different initial HMF concentrations.

A3. Chemical stability/solubility of chitosan, lignin and chitosan-lignin (CL) composites

The chemical stability/solubility of chitosan, lignin and chitosan-lignin (CL) composites was evaluated by preparing a suspension of composites in different solvents (3mg/3ml). The suspensions were stirred for 15 minutes at 400 rpm. Afterwards the suspensions were filtered (0.20 µm, 25mm, nylon filters) and then filtrate was analyzed using Thermoscientific Evolution 220-UV-VIS spectrophotometer.

Chitosan showed partial solubility in all the tested solvents (Figure A3). Whereas, lignin was completely soluble in water and 0.1 M NaOH and partially soluble in acetonitrile (ACN), methanol (MeOH) and 0.1 M H_2SO_4 (Figure A4). CL composites also showed partial solubility in ACN and water (Figure A5). Though, the solubility of CL composite in ACN and water is not desirable from the photocatalytic application

point of view. However, the CL composite were further coupled with titania which possibly improve the chemical stability of CL composites. The results of the chemical stability/solubility of chitosan, lignin and chitosan-lignin (CL) composites are summarized in Table A2

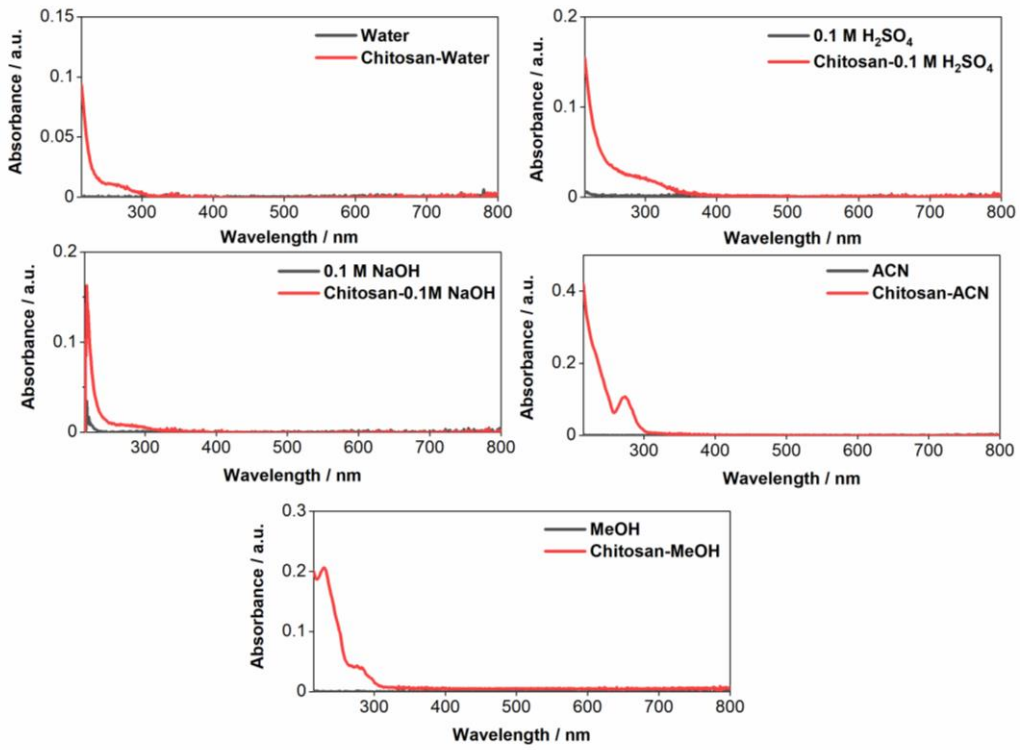

Figure A3. The chemical stability/solubility of chitosan in different solvents.

Table A2: Solubility of chitosan, lignin and chitosan-lignin (CL) composites in different solvents.

Entries	Solvents	0.1 M NaOH	0.01M H_2SO_4	Water	Methanol	Acetonitrile
1	**Lignin**	Soluble	Partially soluble	Soluble	Partially soluble	Partially soluble
2	**Chitosan**	Partially soluble	Partially soluble	Partially soluble	Partially soluble	Partially soluble
3	**CL composites**	Partially soluble	Partially soluble	Partially soluble	Partially soluble	Partially soluble

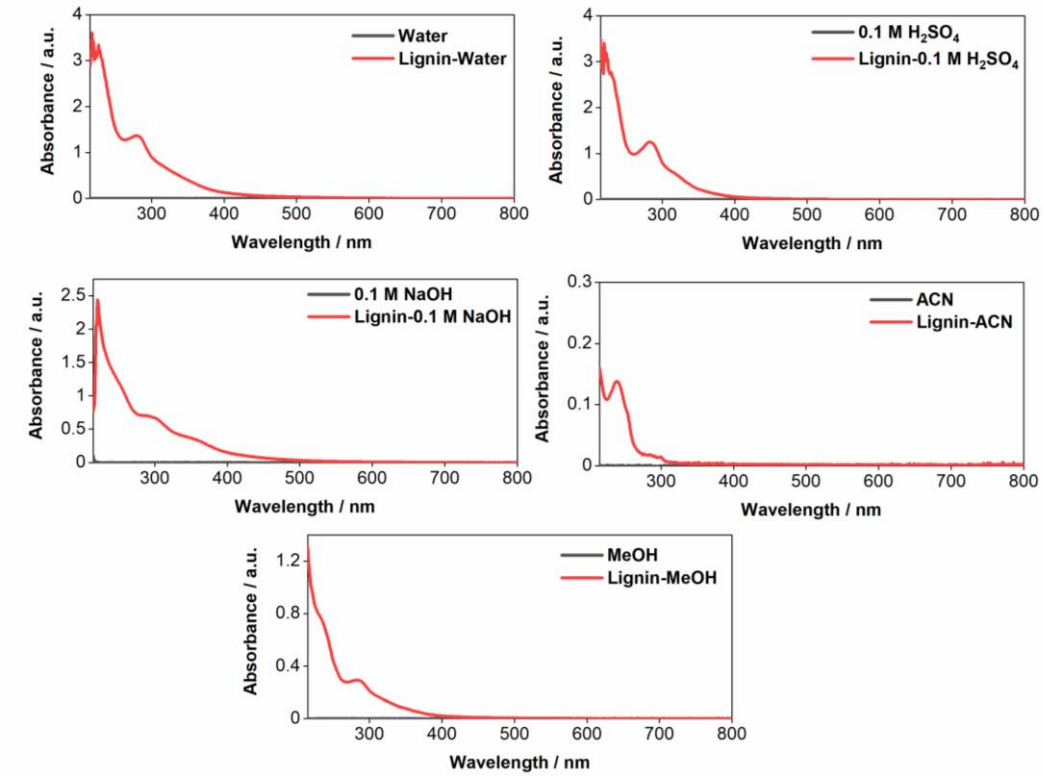

Figure A4. The chemical stability/solubility of lignin in different solvents.

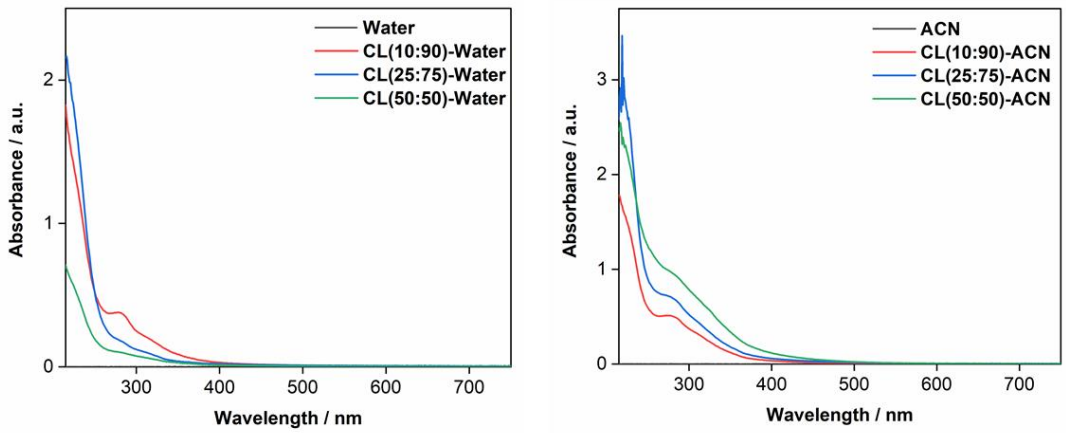

Figure A5. The chemical stability/solubility of CL composites in water and acetonitrile (ACN).

A4. Optimization of titania content in titania/chitosan-lignin (T/CL) nanocomposites

In order to optimize the titania content, T/CL nanocomposites were prepared with the weight fraction of 25/75 (25wt%titania/75wt%CLcomposite, 25T/CL) and 50/50 (50wt% titania/50wt%CLcomposite, 50T/CL) and (75wt%titania/25wt%CLcomposite, 75T/CL) following the sol-gel and hydrothermal route. To prepare a titania sol, a specified volume of titanium(IV) isopropoxide (TTIP), equivalent to the definite wt% of titania (25wt%, 50wt% and 75wt%) was dissolved in 25 cm^3 of 2-propanol and stirred for 2 hours at room temperature. Afterwards, 1 cm^3 of 1M HNO_3 was added to the solution stirred (400 rpm) for 5 minutes until gelation begins. Subsequently, 25 cm^3 of water was added to the gel formed and further stirred for 3 hours. To prepare the T/CL nanocomposites with different weight fraction of (25wt%, 50wt% and 75wt%) the corresponding titania sol was separately introduced into a suspension of CL composite (0.8 g) in 160 mL of water, while stirring (600 rpm) at room temperature. The resulting suspension was stirred for 5 hours, then filtered, washed with water and dried in oven (80 ^{O}C) for 12 hours. Afterwards, the obtained solid sample was ground to powder and then shifted to Teflon lined autoclave filled (~80%) with water for hydrothermal treatment (150 °C) for 8 hours. Finally, the nanocomposite obtained were dried in hot air oven (110 ^{O}C) for 12 hours. Following the same procedure, a series of nanocomposites were prepared using CL composites synthesized in various weight ratios (10:90, 25:75, 50:50, 75:25 and 90:10).

A5. XRD analysis of T/CL nanocomposites

The reflexes observed in X-ray diffraction pattern of 25T/CL(50:50), 50T/CL(50:50) and 75T/CL(50:50) at 25.4^{o}, 37.9 ^{o}, 48.1 ^{o}, 54.6^{o}, 63.0 ^{o} showed the presence of anatase

(Figure A6). In addition to anatase, reflex for brookite was also found at 30.6 º in 75T/CL(50:50).

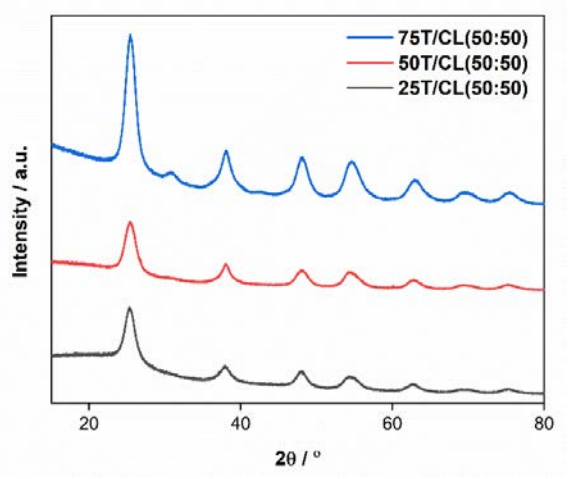

Figure A6. XRD patterns of 25T/CL(50:50), 50TCL(50:50) and 75T/CL(50:50) nanocomposites

A6. N_2 sorption isotherm analysis of T/CL nanocomposites

N_2 sorption isotherm (Figure A7) of 25T/CL(50:50) and 50T/CL(50:50) categorized into Type IV isotherm which is an indication of mesoporous materials. The BET specific surface area of 25T/CL(50:50) and 50T/CL(50:50) was 81 m^2g^{-1} and 123 m^2g^{-1}, respectively.

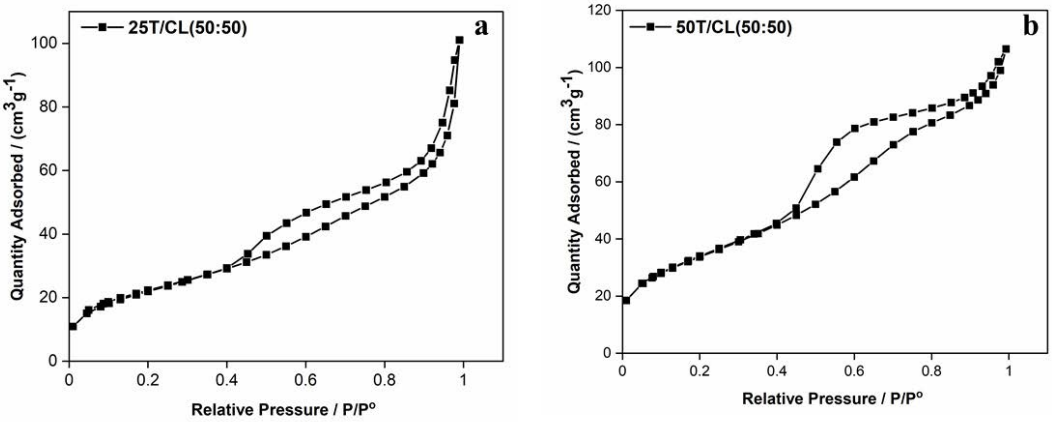

Figure A7. N_2 sorption isotherm of 25T/CL(50:50) and 50T/CL(50:50) nanocomposite.

A7. Optimization of BnOH initial concentration for the photocatalytic selective oxidation over T/CL nanocomposite

Based on the optimization of initial concentration of HMF for the photocatalytic selective oxidation, the preliminary experiments for photocatalytic selective oxidation of BnOH over 75T/CL nanocomposites were carried out using 1mM initial concentration of BnOH. As shown in Figure A8, 75T/CL nanocomposites showed 33-48% BnOH conversion and high Bnald selectivity (>85%) after 4 hours of illumination under UV light. However, under visible light (515 nm) 75T/CL nanocomposites showed low BnOH conversion 3-17% with excellent Bnald selectivity (100%) after 4 hours of illumination (Figure A9). To test the effect of initial BnOH concentration on the BnOH conversion, the photocatalytic selective oxidation of BnOH over 75T/CL nanocomposite was carried out using 0.5 mM initial BnOH concentration. The BnOH conversion and Bnald selectivity was slightly improved (Entries 1-6, Table A3) under UV light.

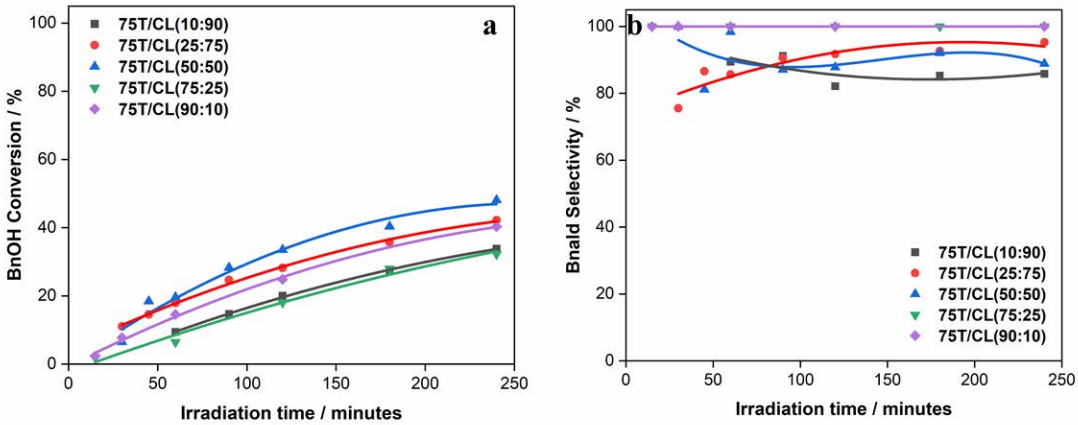

Figure A8. a) BnOH conversion profile of 75T/CL nanocomposites using 1mM initial BnOH concentration, as a function of time under UV light (375 nm) b) Bnald selectivity profile of 75T/CL nanocomposites.

Table A3. The summary of the photocatalytic oxidation of BnOH over titania and titania/chitosan-lignin (T/CL) nanocomposite.

Entries	photocatalyst	Light	BnOH Conv. / %	Bnald Sel. / %	C Balance / %
1	75T/CL(10:90)	UV	38	100	100
2	75T/CL(25:75)	UV	55	94	97
3	75T/CL(50:50)	UV	53	97	98
4	75T/CL(75:25)	UV	45	100	100
5	75T/CL(90:10)	UV	46	99	<99
6	75T/CL(10:90)	Visible	12	100	100
7	75T/CL(25:75)	Visible	19	100	100
8	75T/CL(50:50)	Visible	16	100	100
9	75T/CL(75:25)	Visible	14	100	100
10	75T/CL(90:10)	Visible	15	100	100
11	25T/CL(10:90)	UV	0.0	0.0	100
12	25T/CL(25:75)	UV	0.0	0.0	100
13	25T/CL(50:50)	UV	0.0	0.0	100
14	25T/CL(75:25)	UV	0.0	0.0	100
15	25T/CL(90:10)	UV	0.0	0.0	100
16	25T/CL(10:90)	Visible	0.0	0.0	100
17	25T/CL(25:75)	Visible	0.0	0.0	100
18	25T/CL(50:50)	Visible	0.0	0.0	100
19	25T/CL(75:25)	Visible	0.0	0.0	100
20	25T/CL(90:10)	Visible	0.0	0.0	100
21	50T/CL(10:90)	UV	0.0	0.0	100
22	50T/CL(25:75)	UV	0.0	0.0	100
23	50T/CL(50:50)	UV	4	94	>99
24	50T/CL(75:25)	UV	0.0	0.0	100
25	50T/CL(90:10)	UV	5	80	99
26	50T/CL(10:90)	Visible	0.0	0.0	100
27	50T/CL(25:75)	Visible	0.0	0.0	100

28	50T/CL(50:50)	Visible	0.0	0.0	100
29	50T/CL(75:25)	Visible	0.0	0.0	100
30	50T/CL(90:10)	Visible	0.0	0.0	100

(**Reaction conditions:** BnOH (0.5mM, 0.01 mmol), photocatalyst (1g/l, 20 mg), reaction time (4 hours), reaction medium (acetonitrile), BnOH solution volume (20 mL) incident light wavelength (UV: 375 nm, Visible: 515 nm), incident light intensity was (6 x ~9 W/m^2)

Similarly, under visible light the BnOH conversion was slightly improved (12-19%) using 0.5 mM initial BnOH concentration with similar Bnald selectivity (100%). On the other hand, 25T/CL and 50T/CL nanocomposites were found to be photocatalytically inactive for the selective oxidation of BnOH under UV and visible light (Table A3).

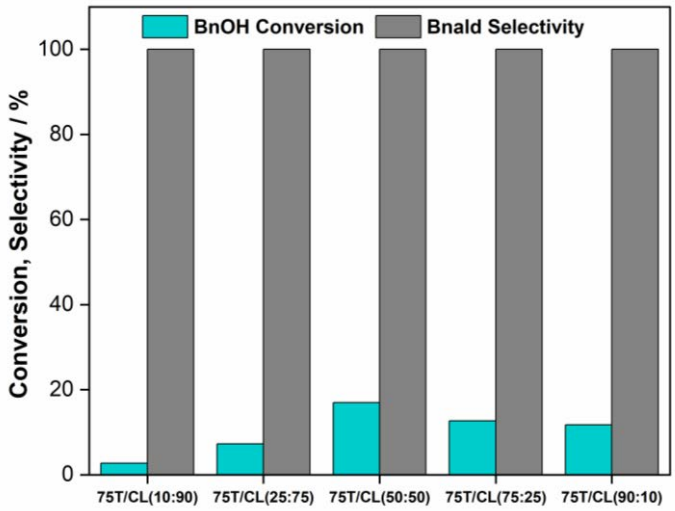

Figure A9. Photocatalytic selective oxidation of BnOH (using 1 mM initial concentration) over 75T/CL nanocomposites under visible light (515 nm).

A8. Photocatalytic activity of 75T/CL nanocomposites for the selective oxidation of HMF

The photocatalytic activity of 75T/CL nanocomposites was evaluated for the selective oxidation of HMF to DFF under visible light (515 nm) in acetonitrile using the same condition and parameters used for SGH-TiO_2. As shown in Figure A10, 75T/CL nanocomposite exhibited much lower activity (15-30% HMF conversion) after 4 hours of illumination. However, 75T/CL nanocomposites showed comparatively improved DFF selectivity (>90%) than SGH-TiO_2 at lower HMF conversion (5-15%). Whereas, at higher HMF conversion (>20%) 75TCL nanocomposites and SGH-TiO_2 showed comparable DFF selectivity.

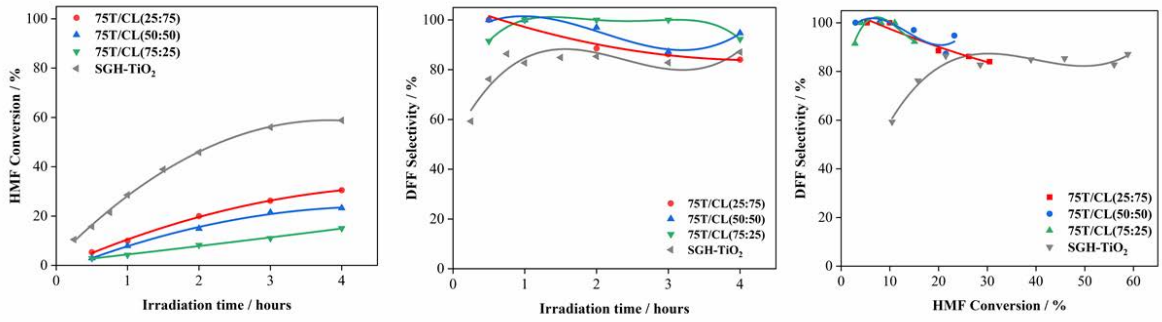

Figure A10. a) HMF conversion profile of 75T/CL nanocomposites and SGH-TiO_2 as a function of time under visible light (515 nm) b) DFF selectivity profile of 75T/CL nanocomposites and SGH-TiO_2 as a function time under visible light (515 nm) c) HMF conversion versus DFF selectivity plot for 75T/CL nanocomposite and SGH-TiO_2 under visible light (515 nm).

A9. Thermogravimetric analysis (TGA) of SGH-TiO_2 and P25

Thermogravimetric analysis (TGA) of SGH-TiO_2 and P25 (Figure A11) was carried out to determine the hydroxyl (OH) group density of titania samples. The weight loss

occurred between 120 ^{O}C - 750 ^{O}C was used to estimate the hydroxyl (OH) group density.

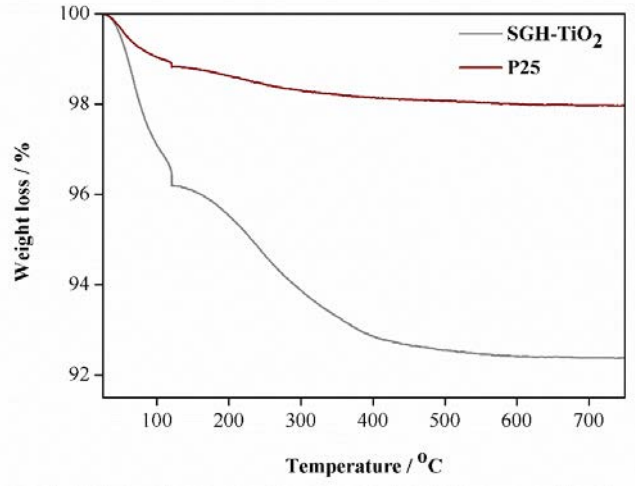

Figure A11. Weight loss during TGA of SGH-TiO$_2$ and P25. (Reprinted an open-access article content[12])

A10. UV-Visible-DRS absorption analysis of 99T/C nanocomposite

99T/C nanocomposite showed absorption (Figure A12) in the entire UV-visible region (220-800 nm). However, the optical band gap estimated for 99T/C via Kubelka-Munk function was ~3.2 eV.

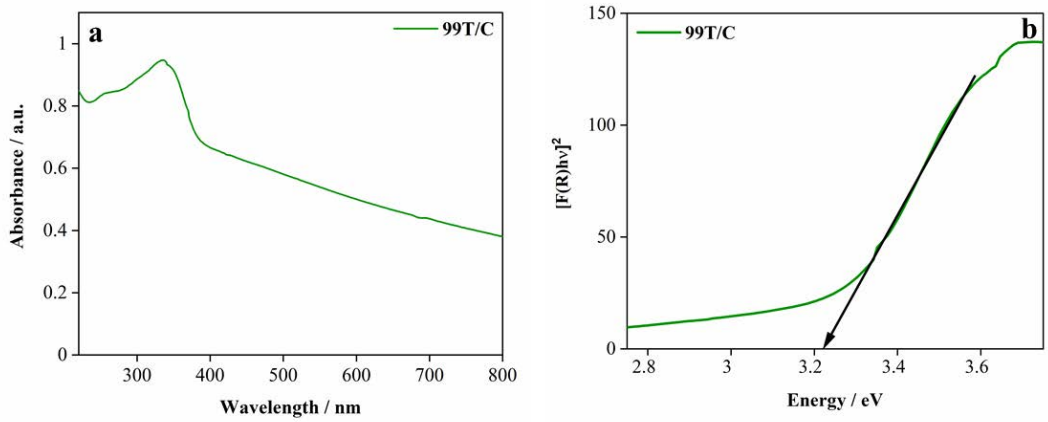

Figure A12. UV-Visible-DRS absorption spectra of 99T/C nanocomposite, b) Optical band gap of 99T/C nanocomposite.

A11. DRS-UV-visible absorption analysis of SGH-TiO_2 and benzyl alcohol adsorbed SGH-TiO_2 (BnOH-Ads-SGH-TiO_2)

To evaluate the effect of adsorption of BnOH on the optical absorption behavior of SGH-TiO_2, DRS-UV-Visible absorption spectra (Figure A13) was recorded for SGH-TiO_2 and benzyl alcohol adsorbed SGH-TiO_2 (BnOH-Ads-SGH-TiO_2). As shown in Figure A13, optical absorption behavior of SGH-TiO_2 is not affected after the adsorption of BnOH, which indicates that the BnOH-Ads-SGH-TiO_2 might not be photocatalytically active under visible light (515 nm).

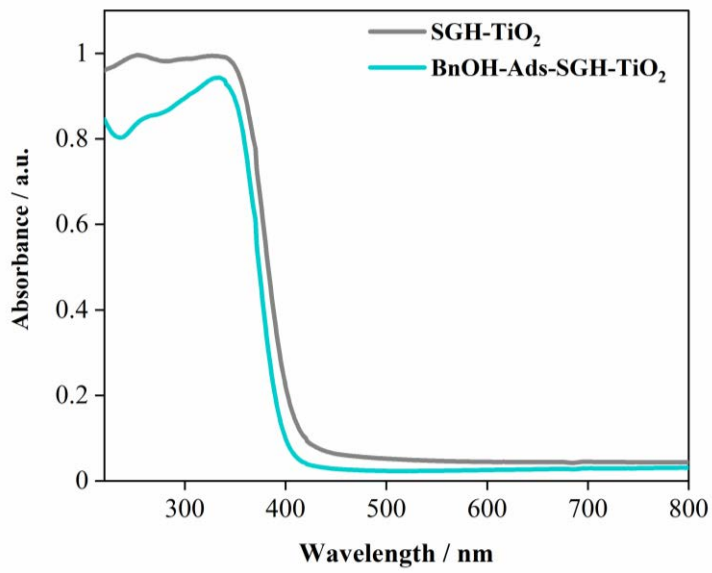

Figure A13. DRS-UV-visible absorption spectra of SGH-TiO_2 and benzyl alcohol adsorbed SGH-TiO_2 (BnOH-Ads-SGH-TiO_2).

A12. Temperature programmed oxidation (TPO) of SGH-TiO_2 and P25

The temperature programmed oxidation (TPO) experiments were carried out to determine carbon content in titania samples. The carbon content was estimated from the CO_2 signals of the QMS (Figure A14), calibrated using CO_2 (with the pulse of 1.01 × 10^{-5} mol).

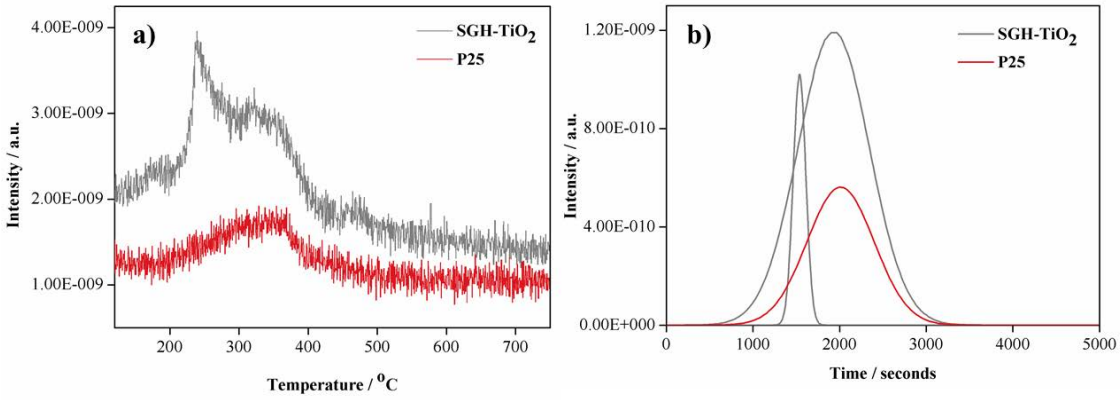

Figure A14 a) CO_2 signal as a function of temperature. b) CO_2 signals as a function of time. (Reprinted an open-access article content[12])

A13. UV-Visible absorption analysis of potassium–ferrioxalate phenanthroline complex (PFPC)

To determine the amount of Fe^{2+} produced during actinometry experiment after the illumination, the absorption of illuminated and control sample (prepared in dark) was recorded (Figure A15) on Thermoscientific Evolution 220 UV Vis Spectrophotometer.

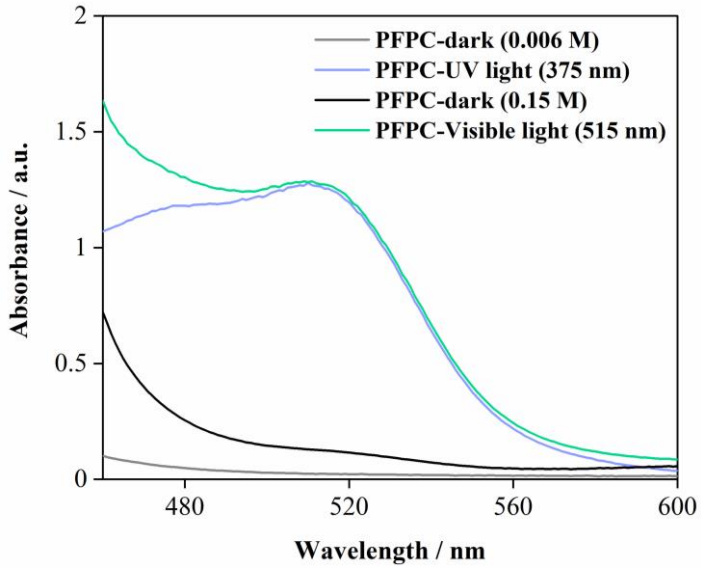

Figure A15. UV-Visible absorption spectrum of potassium–ferrioxalate phenanthroline complex (PFPC).

A14. Calibration of 5-hydroxymethylfurfural (HMF), 2,5- diformylfuran (DFF), benzyl alcohol BnOH and benzaldehyde (Bnald).

The calibration of 5-hydroxymethylfurfural (HMF), 2,5- diformylfuran (DFF), benzyl alcohol BnOH and benzaldehyde (Bnald) in acetonitrile is shown in Figure A16 and A17.

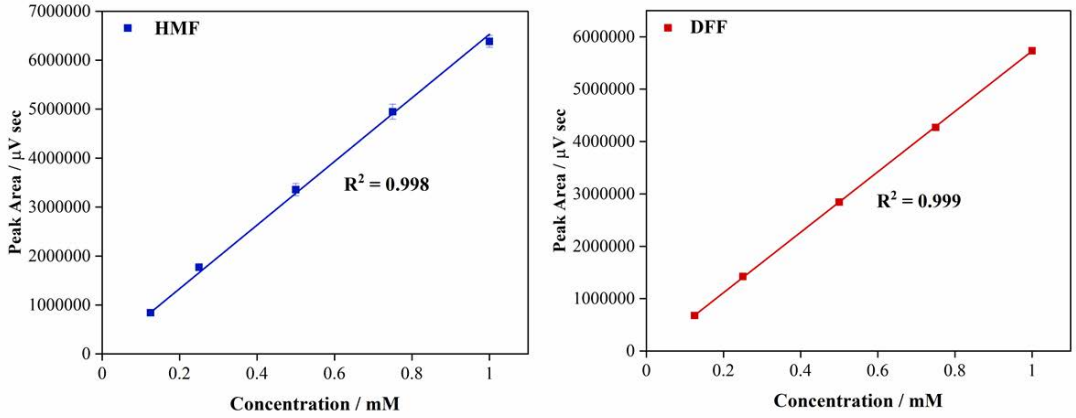

Figure A16. Calibration curve for 5-hydroxymethylfurfural (HMF) and 2,5-diformylfuran (DFF) in acetonitrile.

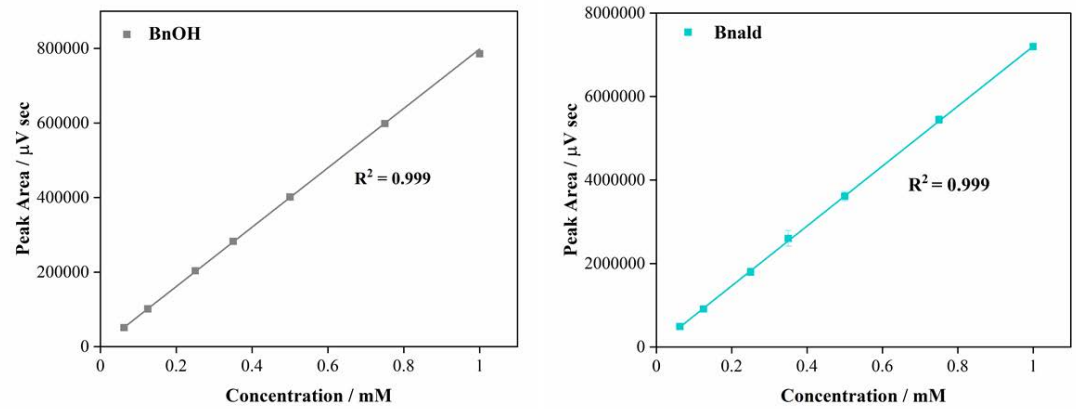

Figure A17. Calibration curve for benzyl alcohol (BnOH) and benzaldehyde (Bnald) in acetonitrile.

A15. Emission spectra of the light sources

The emission spectrum of the light sources used in the photocatalytic selective oxidation experiments for HMF and BnOH are shown in Figure A18.

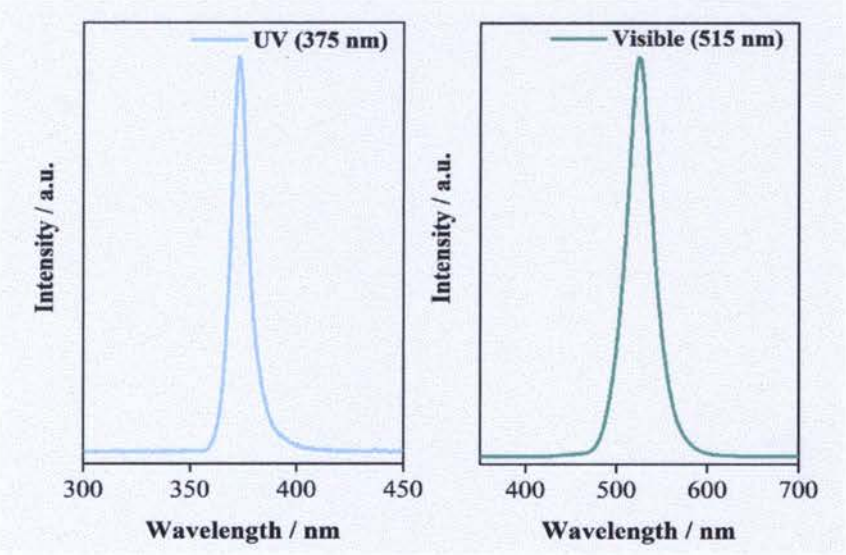

Figure A18. Emission spectrum for UV (375 nm) and visible (515 nm) LED light source.

A16. UV-Visible absorption analysis of HMF

The UV visible absorption spectrum (Figure A19) of HMF in acetonitrile showed that HMF showed absorption maximum at 280 nm.

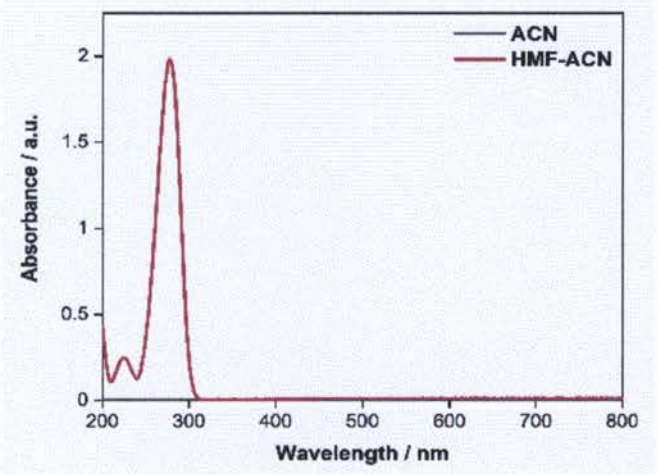

Figure A19. UV-Visible absorption spectrum of HMF in acetonitrile.